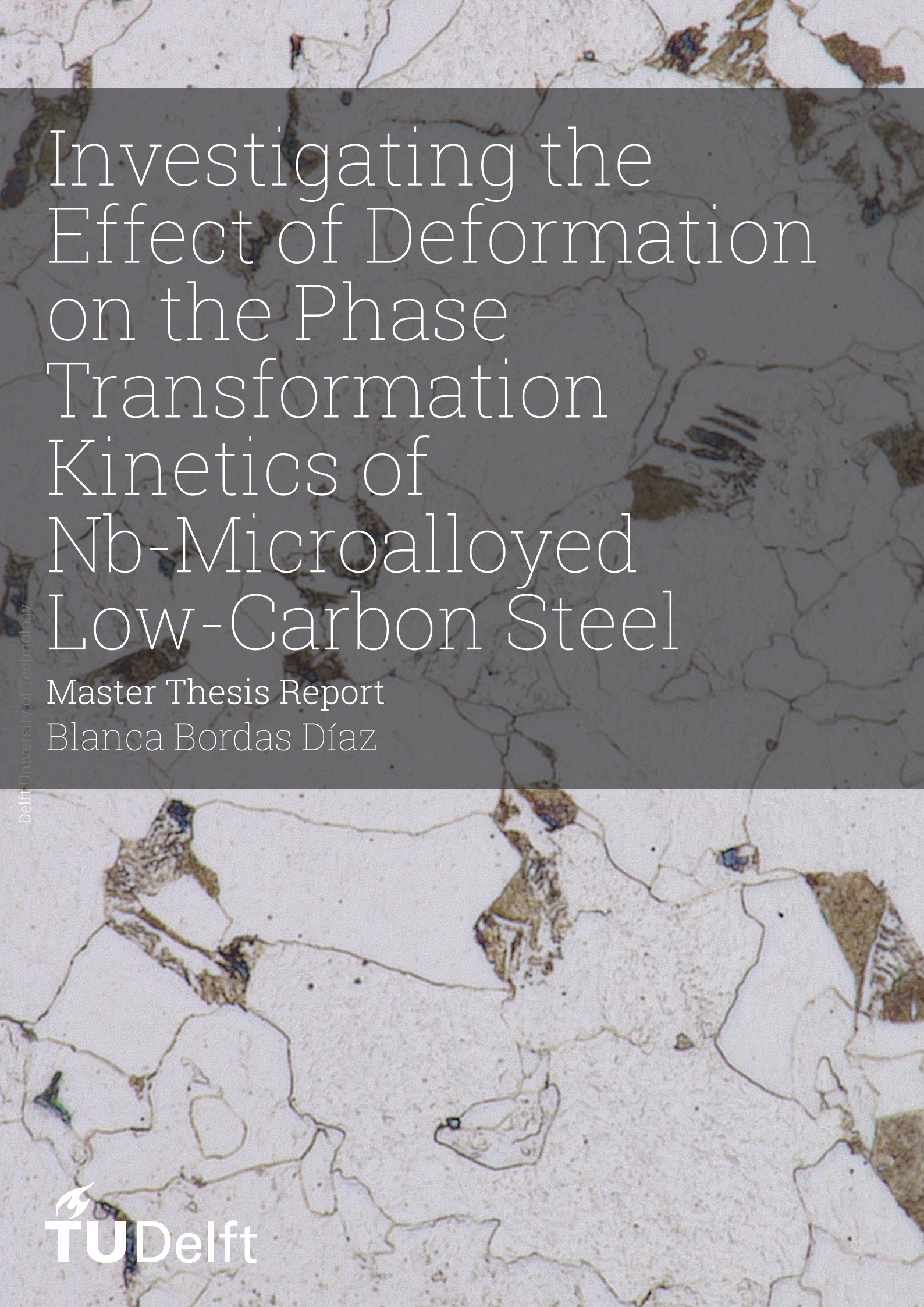

Investigating the Effect of Deformation on the Phase Transformation Kinetics of Nb-Microalloyed Low-Carbon Steel

Master Thesis Report

Blanca Bordas Díaz

Delft University of Technology

TU Delft

Investigating the Effect of Deformation on the Phase Transformation Kinetics of Nb-Microalloyed Low-Carbon Steel

by

Blanca Bordas Díaz

to obtain the degree of Master of Science
at the Delft University of Technology,
to be defended publicly on Thursday 26th of February, 2026 at 11:00.

Student Number:	6067077
Responsible Professor:	S. E. Offerman, Dr. Ir.
Daily Supervisor:	T. Brederode, Ir.
Faculty:	Materials Science & Engineering (MSE), TU Delft

Cover: Optical microscopy image of the material under investigation cooled down at 1 K/s, showing ferrite (light grains) and pearlite (dark grains).

An electronic version of this thesis is available at `http://repository.tudelft.nl/`.

TU Delft

Acknowledgments

First of all, I would like to thank my daily supervisors, Erik Offerman and Timo Brederode, for their weekly guidance and support throughout the duration of this thesis. Their help made this process more enriching and encouraged me to become more passionate about the topic. I would also like to express my gratitude to Kees Bos and Theo Kop from TATA Steel for providing the samples used in this work, as well as insightful information about the material and the topic. Hossein Beladi was also of great help with his knowledgeable insights and recommendations throughout the project.

I would also like to give a special mention to all the technicians who helped me solve the problems I encountered in the laboratory: Nico Geerlofs and Raymond Dekker with the dilatometer, Durga Mainali with sample preparation and optical microscopy, and Kees Kwakernaak for the EBSD measurements.

After six and a half years of studying abroad, I have been incredibly fortunate to have my family's support every day. For this, I want to thank my dad and mum for the opportunity they have given me; without them, this would not have been possible. I would also like to thank my sisters, whom I was lucky enough to have just a one-hour NS trip away for most of my studies. I have missed them especially during these past two years.

My friends have also been an invaluable part of this journey. My master friends have been really special, whose closeness showed me how people from many different cultures can truly connect. They have given me many nights filled with laughter and enjoyable study sessions. To my friends from Eindhoven who walked with me on this journey, our time together was deeply meaningful. We grew up together, lived through the most intense years of our lives, and created memories that I will cherish forever.

Blanca Bordas Díaz
Delft, February 2026

Abstract

Deformation is a key element in most thermomechanical processing routes for steel; therefore, understanding how deformation affects phase transformation kinetics is essential for effective microstructure control and for tailoring mechanical properties. In this study, different levels of compressive strain (ε_2 = 0.0, 0.3 and 0.5), followed by continuous cooling at different rates (1, 10, 50 and >100 K/s), were applied to a Nb-microalloyed low-carbon steel (0.05C-1.3Mn-0.042Nb-0.2Si-0.010Ti-0.03Al-0.0040N-Bal. Fe, wt.%). To quantify the influence of deformation in the austenite on the transformed product, the resulting microstructure, grain size, grain boundary character, and hardness were analyzed and the combined results were used to construct a continuous cooling transformation (CCT) diagram.

Results show that with increasing deformation, the pearlite fraction of the slow-cooled samples decreases. Samples with higher cooling rates and increasing deformation exhibit increased variability in the resulting microstructures, due to shifts in the CCT curves. The results show that increasing deformation in the austenite generally leads to grain refinement in the transformed phases for all cooling rates. However, despite the reduction in grain size with increasing deformation, the hardness decreases with increasing deformation for all cooling conditions. For the slow-cooled samples, it is associated with a decrease in the pearlite fraction. However, for the samples processed at high cooling rates, this behavior is explained by the nature of the microstructural constituents present in the samples, which, they evolve from martensite to bainite and eventually to ferrite with increasing deformation. Grain boundary analysis reveals that the effect of deformation on total grain boundary length strongly depends on the cooling rate. At low cooling rates, deformation promotes the formation of low-angle grain boundaries (LAGBs), and at high cooling rates, the grain boundary length decreases with increasing deformation, attributed to changes in the resulting microstructures.

In the CCT diagram, deformation shifts the ferrite transformation curves to shorter times and locally to higher temperatures, while the bainite curves are also shifted to shorter times, but locally to lower temperatures. The martensitic transformation is suppressed to a lower temperature with increasing deformation. Overall, the results demonstrate that prior deformation has a pronounced effect on the microstructural evolution and phase transformation kinetics of a Nb-microalloyed low-carbon steel.

Contents

Nomenclature

Abbreviations

Abbreviation	Definition
BCC	Body-Centered Cubic
BCT	Body-Centered Tetragonal
CCT	Continuous Cooling Transformation
CR	Cooling rate
CI	Confidence Interval
DRX	Dynamic Recrystallization
EBSD	Electron Back-Scatter Diffraction
FCC	Face-Centered Cubic
GB	Grain Boundary
HAGB	High-Angle Grain Boundary
HF	High-frequency
HSLA	High-Strength Low-Alloy
IQ	Image Quality
IPF	Inverse Pole Figures
LAGB	Low-Angle Grain Boundary
ND	Normal Direction
OIM	Orientation Imaging Mapping
OM	Optical Microscopy
PAG	Parent Austenite Grain
RD	Rolling Direction
SEM	Scanning Electron Microscopy
SFE	Stacking Fault Energy
TD	Transverse Direction
TMP	Thermo-Mechanical Processing
TTT	Time-Temperature-Transformation

Symbols

Symbol	Definition	Unit
α	Ferrite	[-]
α'	Martensite	[-]
A_{e1}	Austenite start temperature (equilibrium)	[°C]
A_{e3}	Austenite finish temperature (equilibrium)	[°C]
A_{c1}	Austenite start temperature (heating)	[°C]
A_{c3}	Austenite finish temperature (heating)	[°C]
A_{r1}	Austenite start temperature (cooling)	[°C]
A_{r3}	Austenite finish temperature (cooling)	[°C]
B_s	Bainite start temperature	[°C]
B_f	Bainite finish temperature	[°C]
$\mathrm{CR}_{\mathrm{max}}$	Maximum cooling rate	[K/s]
ε_1	1st deformation step	[%]
ε_2	2nd deformation step	[%]
γ	Austenite	[-]
M_s	Martensite start temperature	[°C]
M_f	Martensite finish temperature	[°C]
T_s	Transformation start temperature	[°C]
T_f	Transformation finish temperature	[°C]

1

Introduction

As the global demand for materials continues to increase, the traditional linear approach of extracting raw materials, processing them, and discarding products at the end of their service life is no longer sustainable. To address this challenge, circular economy strategies have become increasingly important. Besides reduced CO_2 emissions, these strategies promote innovation, improved efficiency, durable products and conservation of raw materials [1]. In the metals industry, steel plays a central role in this transition. The versatility of steel, arising from its wide range of compositions, processing routes, and product forms, enables its application across numerous industries and significantly enhances its contribution to a circular economy [2]. Responsible and efficient use of steel therefore relies not only on recycling but also on optimizing processing routes to achieve the desired combination of mechanical properties and performance with minimal material and energy input.

Deformation is an inherent part of most industrial steel processing routes, such as rolling and forging. Consequently, understanding the influence of deformation on the phase transformation kinetics of steel is essential for effective microstructure control and tailoring mechanical properties. The compressive simulation of steel using thermo-mechanical testing equipment, such as a dilatometer operated in deformation mode, provides a controlled approach for studying the influence of deformation on phase transformation kinetics. Such simulations are particularly relevant for primary steel processing operations, including hot rolling, forging, sheet metal forming, and extrusion, where deformation and thermal histories strongly affect microstructural evolution.

This study aims to clarify how deformation in the austenite affects the ferrite, pearlite, bainite and martensite transformation behavior in a Nb-microalloyed low-carbon steel under continuous cooling conditions, providing guidance for optimizing thermomechanical processing to produce high-strength structural steels for building applications [3]. First, the microstructure will be characterized using the dilatometer data, optical microscopy (OM) and hardness will be measured. The results will be combined and plotted in a Continuous Cooling Transformation (CCT) Diagram. These experimental results are supported by Thermo-Calc predictions and comparisons with relevant literature. To further understand the influence of deformation, the grain size and grain boundary length will also be measured. The findings will provide insight that is directly applicable to industrial thermomechanical processing routes and contributing to more efficient and sustainable steel production.

The report has been structured as follows: Chapter 2 presents the background information on the topic of deformation and phase transformation kinetics. Chapter 3 details the research methodology employed in this study, including sample preparation and dilatometry, OM, Vickers hardness, EBSD and grain size analysis. Chapter 4 presents and discusses the results obtained from these techniques. Chapter 5 summarizes the main findings in a conclusion, followed by future recommendations in Chapter 6.

2

Background Information

This section provides an overview of how the chemical composition of a material and deformation can influence the microstructure and mechanical properties of steel. As well as their effect on the kinetics and thermodynamics of phase transformations. Together, these topics establish the necessary background for understanding the principles underpinning this thesis before delving into the methodology.

2.1. Fundamentals of Steel Microstructure

Steel is primarily composed of iron (Fe) and carbon (C), with the addition of alloying elements. Depending on the thermal and processing conditions used, steel can exhibit both equilibrium and non-equilibrium microstructural constituents. The former are ferrite, austenite, and cementite, with pearlite representing an equilibrium microstructure composed of ferrite and cementite. The latter are bainite and martensite which form under fast cooling conditions. The formation of these microstructural constituents plays a critical role in determining the final mechanical properties of steel, which are also influenced by carbon and other alloying elements.

2.1.1. Effect of Carbon Content

Carbon strongly governs phase stability, transformation behavior, and mechanical properties of steels. It is known to influence the fraction, morphology, and hardness of the resulting microstructural constituents [4]. Carbon is the primary strengthening element, with its concentration ranging from approximately 0.02 to 2 wt.% [5]. Low-carbon steels (less than approximately 0.3 wt.% C) exhibit excellent ductility and weldability, and are widely used in structural and automotive applications. Carbon atoms occupy interstitial sites within the iron crystal lattice, which hinders dislocation motion. Therefore, increasing carbon content generally enhances tensile strength and hardness while reducing ductility and weldability [5]. The principal microstructural constituents commonly observed in carbon steels are briefly described below, with their typical formation ranges schematically illustrated in Figure 2.1.

Austenite is the high-temperature phase of steel, with a face-centered cubic (FCC) structure [6]. Ferrite, with a body-centered cubic (BCC) crystal structure, consists of nearly pure iron with a very low carbon solubility at room temperature (typically below 0.005 wt.%). This phase commonly exhibits an equiaxed, polygonal morphology and it is recognized as a relatively soft and highly ductile phase that develops under slow cooling conditions [6]. An example is shown in Figure 2.2(a) and (b). Micrographs 2.2(c)-(e) correspond to acicular ferrite which consists of irregular ferrite grains.

As the carbon content increases, excess carbon combines with iron to form cementite (Fe_3C), a hard and brittle iron carbide phase. This phase forms when the carbon content exceeds the solubility limit in ferrite [6]. During slow cooling, ferrite and cementite arrange into a lamellar microstructure known as pearlite, which provides an intermediate combination of strength and ductility and is frequently observed in low- and medium-carbon steels [6].

Bainite is another transformation product consisting of ferrite and cementite, but different than pearlite.

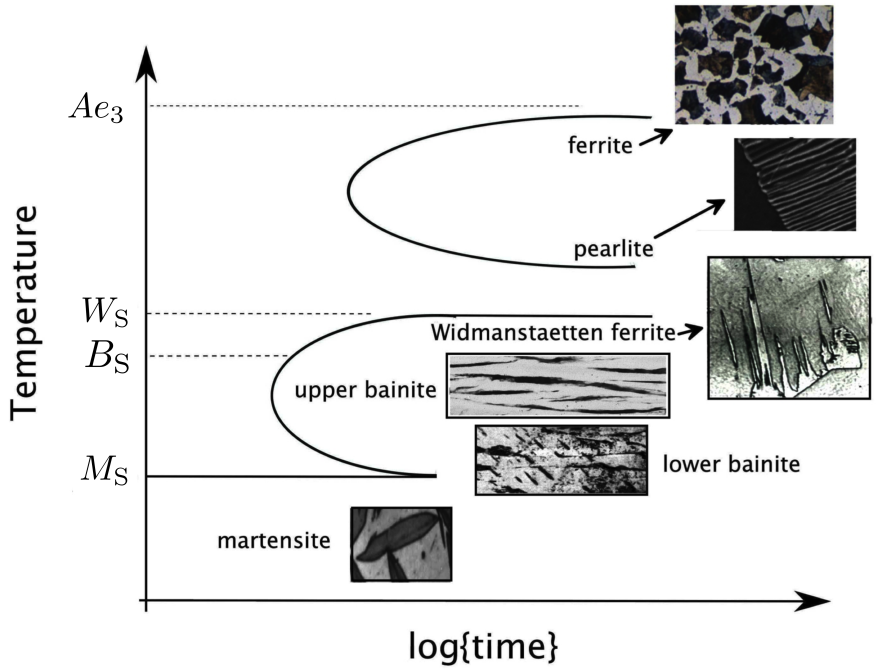

Figure 2.1: Schematic time-temperature-transformation (TTT) diagram illustrating the formation of ferrite, pearlite, bainite (upper and lower), Widmanstätten ferrite, and martensite as a function of temperature and time. The characteristic transformation temperatures (A_{c3}, W_s, B_s, and M_s) are indicated, together with representative microstructural morphologies. *Unpublished image by H.K.D.H. Bhadeshia, used with permission.*

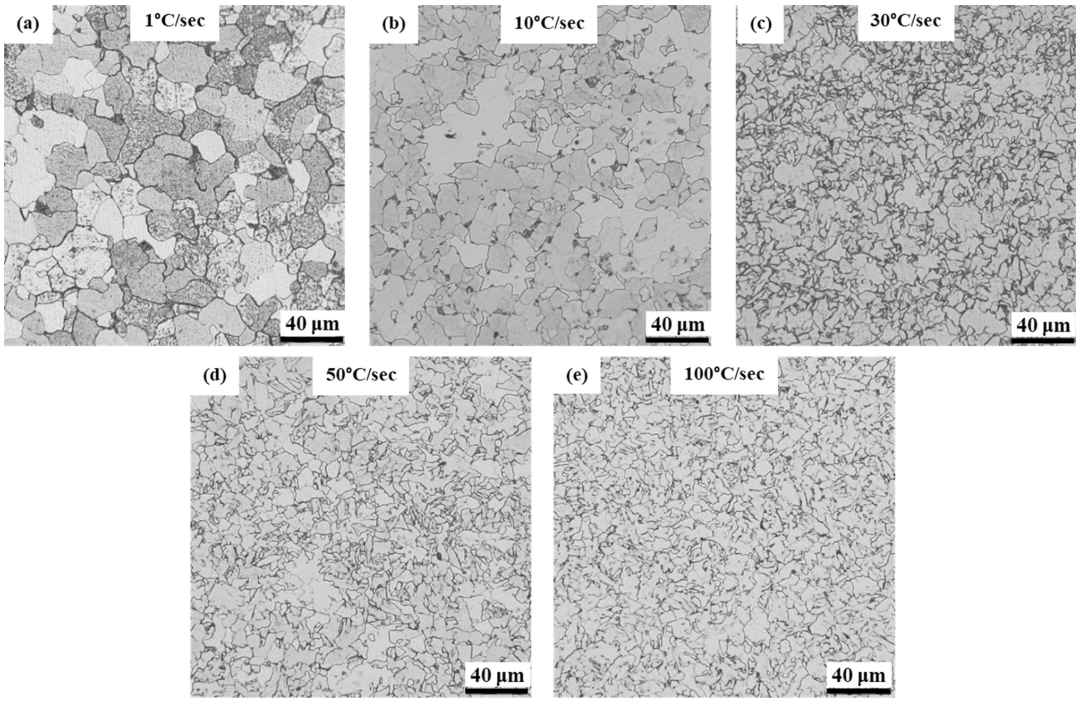

Figure 2.2: Micrographs of a low carbon HSLA steel material, microalloyed with Nb and Ti subjected to a cooling rate of (a) 1 °C/s, (b) 10 °C/s, (c) 30 °C/s, (d) 50 °C/s, and (e) 100 °C/s [7]. *Used with permission of the copyright holder.*

It forms at intermediate temperatures and is commonly classified as upper or lower bainite, depending on the transformation temperature. Upper bainite consists of ferrite laths with carbides located at lath boundaries, whereas in lower bainite the carbides are also distributed within the ferrite laths [6]. Another possible microstructural constituent in low-carbon steels is granular bainite, also termed quasi-polygonal

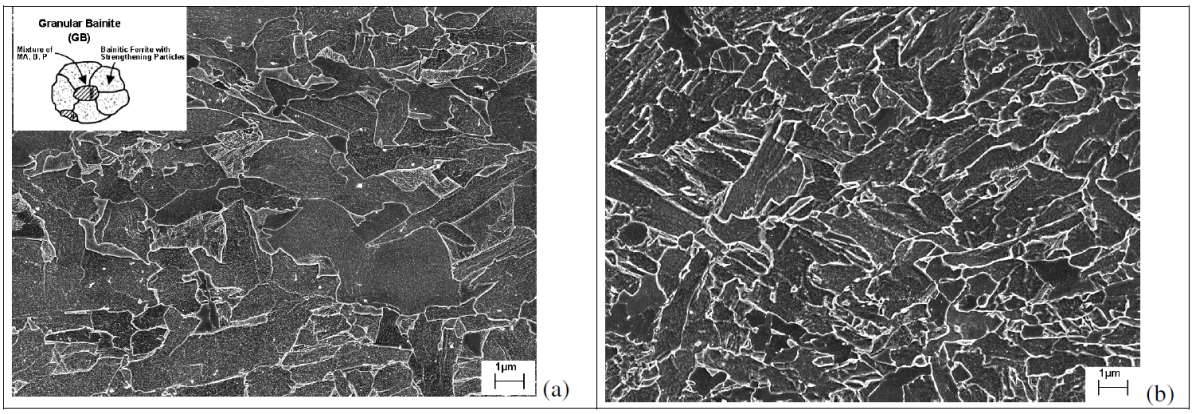

Figure 2.3: Scanning Electron Microscopy (SEM) images of granular bainite with (a) 0.06 wt.%C and (b) 0.045 wt.%C [8].

ferrite (Figure 2.3). It consists of irregular ferrite grains, not a well-defined lath morphology and with second phases distributed between grains, which could be pearlite or cementite [8].

Further increasing the carbon content and for faster cooling rates, the strength of steel increases primarily due to the formation of harder transformation products, particularly martensite [4]. Martensite is a non-equilibrium phase characterized by a high hardness and strength, but very brittle. At sufficiently high cooling rates, carbon becomes trapped within the iron lattice, adopting a distorted body-centered tetragonal (BCT) crystal structure [9].

2.1.2. Effect of Alloying Elements

In addition to carbon, alloying elements play a decisive role in controlling phase stability, phase transformation kinetics and microstructural evolution in carbon steels. Their influence is particularly significant in low-carbon steels, where optimized strength-ductility-toughness combinations are achieved primarily through microstructural control rather than increased carbon content.

Substitutional alloying elements such as manganese (Mn) and silicon (Si) affect transformation behavior primarily by modifying austenite stability and diffusion kinetics. Mn delays diffusional transformations and Si suppresses cementite formation, influencing the morphology of ferrite and bainite [10]. Alloying elements added in small concentrations are called micro-alloying elements. Micro-alloying additions of niobium (Nb) and titanium (Ti) strongly influence the austenite grain growth, recrystallization behavior, and phase transformation kinetics. These elements form fine carbide and nitride precipitates that restrict austenite grain coarsening through grain-boundary pinning and solute drag effects, enhancing the materials' strength and toughness [11, 12]. This suppresses or delays the formation of polygonal ferrite and pearlite and promotes the formation of acicular ferrite or bainitic microstructures under appropriate cooling conditions [11]. Mn has been shown to delay the precipitation of Nb- and Ti-containing phases and to increase the solubility of niobium carbides in austenite by reducing niobium diffusivity, thereby extending the effectiveness of solute Nb during thermomechanical processing [11].

In the case of martensitic transformation, alloying elements dissolved in austenite generally reduce the martensite start temperature (M_s) by increasing austenite stability, strengthening of the austenitic matrix and increasing the resistance to martensite-austenite interface motion [13], with the exception of aluminum and cobalt [14]. Aluminum and nitrogen also play important supporting roles by acting as deoxidizing elements and forming fine AlN and TiN precipitates, which influence grain growth control and precipitation behavior during processing [14].

The influence of alloying and micro-alloying elements on thermomechanical factors and transformation phases are summarized schematically in Figure 2.4. This diagram is a Continuous Cooling Transformation (CCT) plot illustrating how variations in composition shift transformation kinetics and start temperatures during continuous cooling [14].

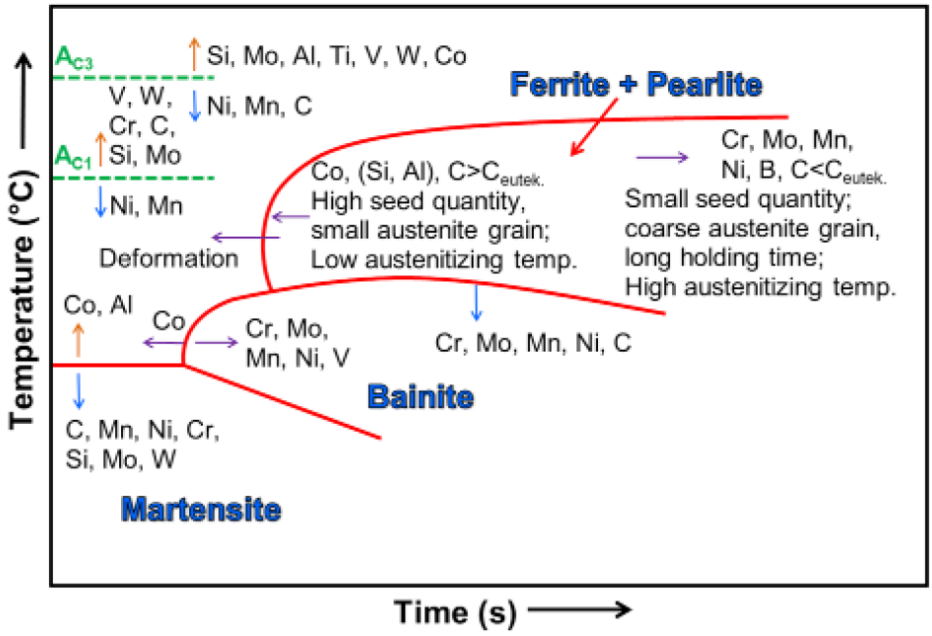

Figure 2.4: Schematic representation of the influence of alloying elements and microstructural state on phase transformation kinetics [14]. The author defines "seeds" as pre-existing sites where a new phase can nucleate.

2.1.3. Phase Transformation Mechanisms

After explaining the microstructural constituents and the effects of material composition, the transformation mechanisms will be discussed. As Hutchinson et al. [15] explains, when a phase transformation takes place, there is nucleation and growth of the grains. Nucleation involves the formation of stable nuclei of a new phase at energetically favorable sites such as grain boundaries, defects, or inclusions. Growth then proceeds by interface migration as atoms diffuse or rearrange, allowing the new phase or grains to expand until impingement or equilibrium is reached. There are two types of growth mechanisms that can take place, diffusional and displacive (diffusionless) growth.

Displacive transformations, as is the case for martensite, occur by coordinated, diffusionless atomic movements that preserve an atomic correspondence between the parent and product lattices, leading to a characteristic macroscopic shape change in the form of an invariant-plane strain with a significant shear component and associated elastic strain energy; as a result, the product typically forms thin plates [16]. In contrast, diffusional transformations, as is the case for ferrite, require reconstructive diffusion involving extensive atomic mixing both normal and parallel to the interface, so no atomic correspondence exists between parent and product lattices; the transformation proceeds by lattice reconstruction without a shear-dominated shape change, resulting in negligible elastic strain energy and more equiaxed morphologies [16]. An illustration exemplifying the resulting atomic correspondence occurring for ferrite (during slow cooling) and martensite (during quenching) can be found in Figure 2.5.

2.1.4. Thermodynamics and Kinetics of Phase Transformations

Understanding the role of the factors influencing phase transformation kinetics and thermodynamics, provides a qualitative basis for assessing phase transformation behavior [17]. In this section, the thermodynamics and kinetics of the transformation of austenite to ferrite, and to martensite are explained.

The transformation from austenite (γ) to ferrite (α) is diffusion-controlled and requires the redistribution of carbon between the parent and product phases. The thermodynamic driving force for the $\gamma \rightarrow \alpha$ transformation is provided by the chemical free energy difference between the two phases, which increases with decreasing temperature [18]. In general terms, the thermodynamic driving force for the transformation can be expressed as the difference in Gibbs free energy (ΔG_v) between austenite matrix and the ferrite nucleus [19],

$$\Delta G_{\mathrm{v}} = G^{\alpha} - G^{\gamma}, \tag{2.1}$$

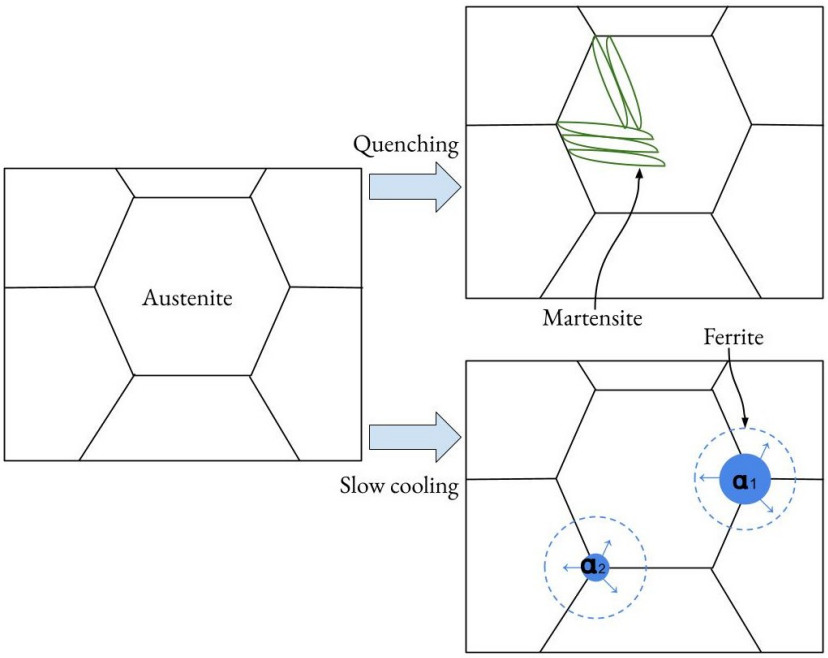

Figure 2.5: Diagram showing the difference in growth mechanisms when slow cooling and quenching from the austenite phase.

the transformation becomes favorable when $\Delta G_v < 0$.

The kinetics of the ferrite transformation, in addition to the thermodynamic driving force, are governed by carbon diffusion and the nucleation and growth of ferrite grains. Following nucleation, ferrite grows by a diffusion-controlled process that can be described by the classical Zener model, which predicts parabolic growth of an isolated ferrite grain when carbon diffusion in austenite is rate-limiting [19, 20]. Because the solubility of carbon in ferrite is much lower than in austenite, carbon is rejected at the moving α/γ interface and must diffuse into the surrounding austenite, thereby controlling the growth rate of ferrite grains. In the early stages of transformation, when interactions between neighboring diffusion fields are negligible, the ferrite grain radius increases with the square root of time, consistent with diffusion-controlled growth kinetics [19]. Alloying elements influence this process by modifying carbon diffusion and the relative thermodynamic stability of ferrite and austenite, thereby affecting both the driving force for transformation and the resulting growth rates [21].

As Jain et al. [17] describes, for the transformation of austenite to martensite, although the chemical free energy of martensite (α') becomes lower than that of austenite (γ) below the temperature T_0, the austenite to martensite transformation does not necessarily occur spontaneously at all temperatures below T_0. T_0 is the temperature at which the Gibbs free energy of martensite is equal to the Gibbs free energy of austenite. Since for this transformation to take place, an interface has to be created and the elastic strain energy arising from the displacive lattice distortion has to be accommodated [17]. Therefore, martensite nucleation becomes possible only when the available driving force exceeds a critical value. At temperature T, the transformation criteria may be expressed as:

$$\Delta G^{\gamma\to\alpha'}_{\text{chemical}} + \Delta G^{\gamma\to\alpha'}_{\sigma} \geq \Delta G^{\gamma\to\alpha'}_{\text{critical}}, \tag{2.2}$$

where $\Delta G^{\gamma\to\alpha'}_{\text{chemical}}(T)$ is the chemical free energy change for the transformation of austenite to martensite, $\Delta G^{\gamma\to\alpha'}_{\sigma}(T)$ is the additional contribution from an applied stress (or deformation), and $\Delta G^{\gamma\to\alpha'}_{\text{critical}}$ represents the minimum driving force required to overcome the interfacial and elastic strain-energy terms. The latter is reached at the martensite start temperature M_s, which corresponds to the point at which the chemical driving force becomes sufficient for nucleation under the given conditions.

2.2. Fundamentals of Deformation in Thermomechanical Processing

Thermomechanical processing (TMP) combines controlled deformation and thermal treatment to tailor the microstructure and mechanical properties of steels. Deformation applied in the austenitic region prior to phase transformation plays a crucial role in accelerating transformation kinetics, refining grain size, and modifying phase selection. These effects, described below, arise from changes in austenite grain morphology, increased dislocation density and stored energy.

Plastic deformation introduces a high density of dislocations, which act as barriers to further dislocation motion and contribute to strengthening of the material through grain refinement. These deformation-induced defects act as short-circuit diffusion paths for substitutional alloying elements such as manganese, which can segregate at phase boundaries and impede interface migration during long holding times [22]. Consequently, tuning the density and distribution of these defects provides an effective means of controlling ferrite nucleation, growth, and final grain size [22]. Additionally, decreasing grain size increases the yield strength and hardness of the material due to the increased grain boundary area, which impedes dislocation glide [23]. This is understood by the Hall-Petch relation, written as follows:

$$\sigma_{0.2} = \sigma_0 + \frac{k}{\sqrt{d}}, \tag{2.3}$$

where $\sigma_{0.2}$ is the conditional yield strength, σ_0 and k are experimental constants, and d is the grain size [24]. As a result, deformation-induced grain refinement is an effective strategy for enhancing mechanical properties in low-carbon steels.

Deformation further influences transformation kinetics by modifying the total driving force for phase transformation to consist of both chemical Gibbs free energy and stored deformation energy [22]. Increased dislocation density enhances stored energy and significantly increases the availability of nucleation sites, particularly at grain boundaries. At low strain levels, ferrite nucleation predominantly occurs at grain boundaries, whereas higher strain levels promote intragranular nucleation associated with austenite grain subdivision and high-angle boundary formation [22]. Moreover, deformation has also shown to the shift ferrite and pearlite transformation curves to shorter times on continuous cooling transformation (CCT) diagrams, reflecting accelerated transformation kinetics. This occurs because a finer austenite grain structure increases the total grain boundary area, providing more nucleation sites [14]. The effect of deformation on bainite transformation is more complex, since bainite involves both displacive and diffusional mechanisms, whose relative contributions are still debated. The influence of deformation on the martensitic transformation is often characterized by a slight suppression due to dislocations hindering interface motion [14]. In some cases, however, accumulated lattice defects can promote martensite nucleation, leading to transformation at higher temperatures than in undeformed austenite [14].

At elevated temperatures, deformation can also trigger dynamic recrystallization (DRX), a process in which new strain-free grains form during deformation through the consumption of dislocations driven by stored energy [25]. DRX leads to grain refinement and microstructural homogenization, improving both strength and toughness [25, 26]. Grain refinement through deformation and recrystallization is widely recognized as an effective method for achieving high strength in metallic materials [22].

Overall, deformation during TMP alters stored energy, nucleation site density, diffusion pathways, and grain morphology. These effects collectively control phase transformation behavior, microstructural refinement, and mechanical properties, making deformation a critical parameter in the design of TMP routes for low-carbon and micro-alloyed steels.

2.3. Continuous Cooling Transformation (CCT) Diagrams

Continuous Cooling Transformation (CCT) diagrams describe the evolution of microstructure as a function of temperature and cooling rate under continuous cooling conditions. They are influenced by the chemical composition, prior austenite grain size, deformation amount, and cooling path to predict the onset and completion of phase transformations. They are constructed by determining transformation

start and finish temperatures over a range of cooling rates, commonly using dilatometry, microstructural analysis, or thermal analysis techniques. Unlike Time-Temperature-Transformation (TTT) diagrams, CCT diagrams are particularly relevant to guide industrial thermomechanical processing routes to obtain the desired microstructures, where cooling occurs continuously rather than isothermally.

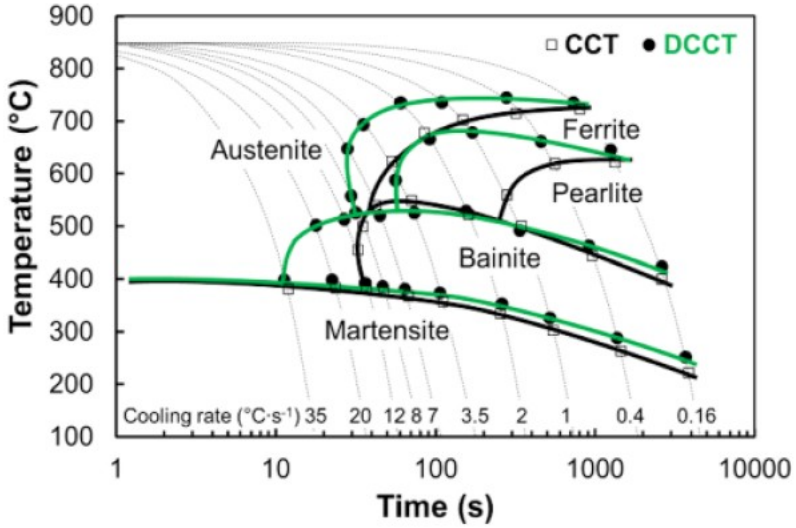

Figure 2.6: Example from literature combining the results of a CCT and DCCT diagram of a 20MnCrS5 steel [14].

Furthermore, the use of CCT diagrams and deformation-CCT (DCCT) diagrams enable assessment of the effect of deformation on phase transformation kinetics. Kawulok et al. [14], observed that deformation applied to a 20MnCrS5 steel accelerated diffusion-controlled transformations, particularly ferrite and pearlite phase transformations, which appeared in the DCCT diagram shifted to shorter times, compared to the (undeformed) CCT diagram (Figure 2.6). A significant acceleration of the bainite transformation was also evident. This behavior was attributed to enhanced nucleation in deformed austenite, where bainite nuclei were preferentially formed within deformation bands [14]. In contrast, the martensitic transformation showed no pronounced sensitivity to prior deformation.

Important uncertainties remain regarding the mechanisms governing bainitic transformation, particularly under the influence of prior deformation. Bainite is widely regarded as a transformation product involving both displacive and diffusional components; however, the relative contribution of these mechanisms is still debated. Experimental observations reported in the literature show inconsistent effects of deformation on bainite transformation kinetics, where in some cases prior deformation leads to a noticeable shift of the bainite region in CCT diagrams, while in others little or no shift is observed [14]. These discrepancies highlight an incomplete understanding of the fundamental transformation mechanisms controlling bainite formation.

To address this gap, the present work experimentally examines the influence of prior deformation on phase transformation kinetics in a low-carbon Nb-microalloyed steel with a defined composition. Dilatometry, microstructural characterization, CCT diagram analysis, hardness measurements, and grain size evaluation are used to understand this effect, with comparisons to literature findings and Thermo-Calc calculations. This approach provides further insight into deformation-affected transformation mechanisms and contributes to a more comprehensive understanding of phase transformation kinetics in thermo-mechanically processed steels.

3

Methodology

3.1. Sample Preparation

The material under investigation was provided by TATA Steel and is a high-strength low-alloy (HSLA) steel type. The composition can be found in Table 3.1. The samples used in this investigation originate from the same metal plate and are cylindrical specimens with dimensions of approximately 10 mm in height and 5 mm in diameter (Figure 3.1).

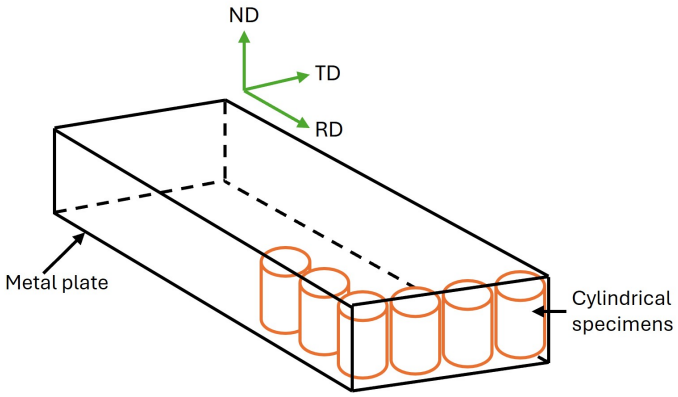

Figure 3.1: Diagram showing the sample orientation of the as-received metal plate with the cylindrical specimens. ND is the normal direction, TD is the transverse direction and RD is the rolling direction.

Table 3.1: Chemical composition (in wt%) of the investigated steel sample.

C	Mn	Nb	Si	Ti	Al	N	Fe
0.05	1.3	0.042	0.2	0.01	0.03	0.004	Bal.

The chemical composition strategy was designed with the objective of maximizing the strength and toughness of the sample with the addition of niobium and low concentration of carbon. Nb promotes grain refinement, which leads to increased strength and toughness [27]. Additionally, the strength is improved by keeping the carbon content low [27], as well as giving the material a low hardenability, which is the maximum depth to which steel can be effectively hardened through quenching [28].

The following sections describe the steps carried out throughout the investigation in detail. In summary, the approach involves the thermal and mechanical treatment of the steel samples using a dilatometer in deformation mode, followed by a microstructural and hardness analysis to determine the phases present in the samples. Based on these findings, a CCT diagram was constructed. To further quantify the effect of deformation on the material, the grain sizes and grain boundary lengths were measured.

3.2. Thermo-Calc

In order to design the thermo-mechanical process, an initial estimate of the phases transformed when different cooling rates are applied is required, as well as their transformation temperatures. This was completed using the software Thermo-Calc 2025b [29], where the CCT diagram (Figure 3.2), TTT diagram (Figure 3.4) and phase equilibrium diagram (Figure 3.5) were predicted.

When the complete material composition, as described in Table 3.1, was specified the software computed an incomplete CCT diagram, with irregular transformation curves. To solve this, a simplified composition of the material was used. The resulting CCT diagram can be seen in Figure 3.2. This is a helpful tool to estimate appropriate cooling rates for desired microstructures. For example, Figure 3.2 shows that at cooling rates exceeding 170 K/s, only martensite is expected to form. However, the difference between forming a ferrite-bainite microstructure or martensite occurs over a very narrow range of cooling rates.

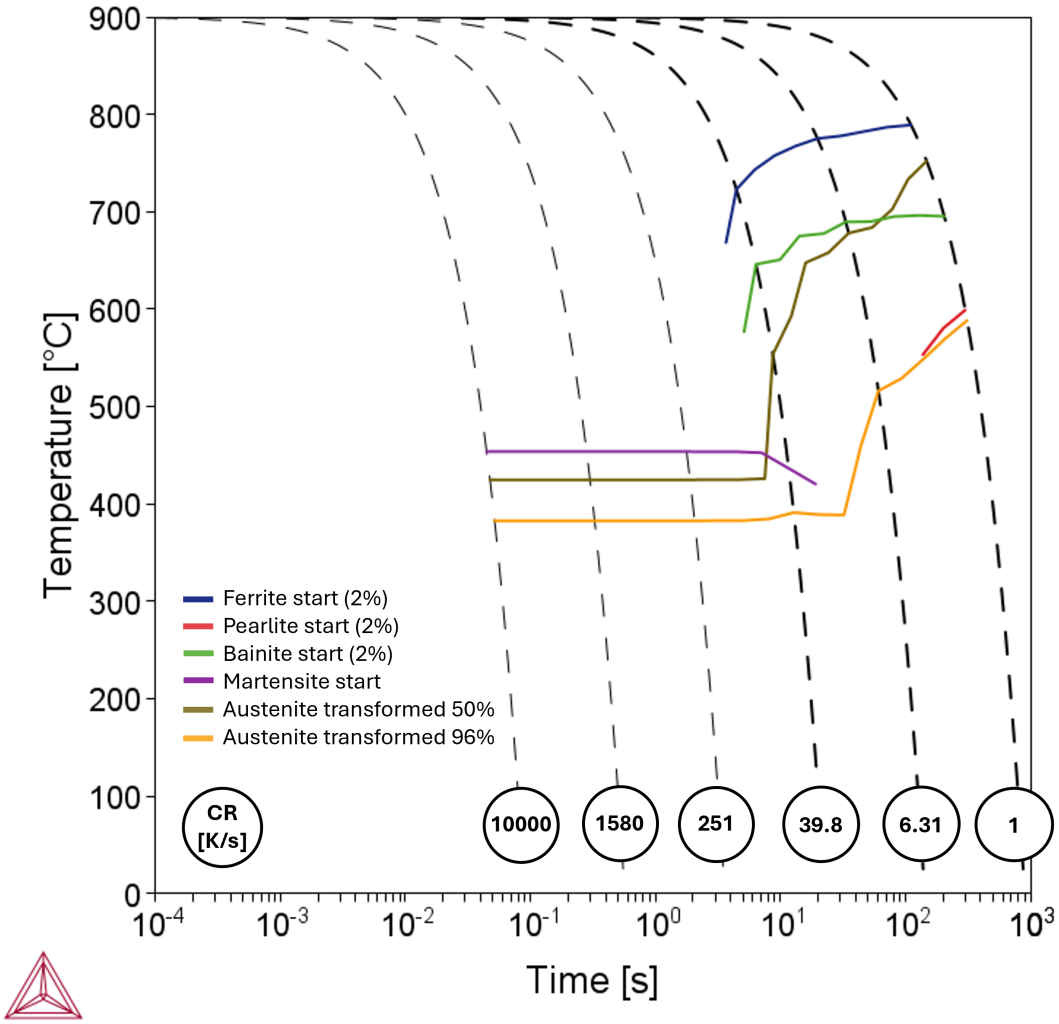

Figure 3.2: CCT diagram for a simplified composition (0.05C-1.3Mn-0.2Si-Bal.Fe in wt%) showing the start temperatures for pearlite, bainite and martensite, as well as the 50% and 98% austenite transformation curves. The dashed lines represent different cooling rates, from fastest to slowest (left to right). No. of steps used was 15 and austenite grain size: 100 μm.

Unfortunately, the effect of deformation cannot be simulated using Thermo-Calc. However, since it is known that applying deformation in the austenite region causes grain refinement [30], to partially simulate this effect, a CCT diagram with a reduced austenite grain size was generated. In this case, an austenite grain size of 20 μm was assumed (refer to Figure 3.3), again using the simplified composition.

Comparing Figure 3.3 with Figure 3.2, it can be observed that the martensite start (M_s) temperature line decreases slightly for a smaller austenite grain size. This can be explained with dislocation networks

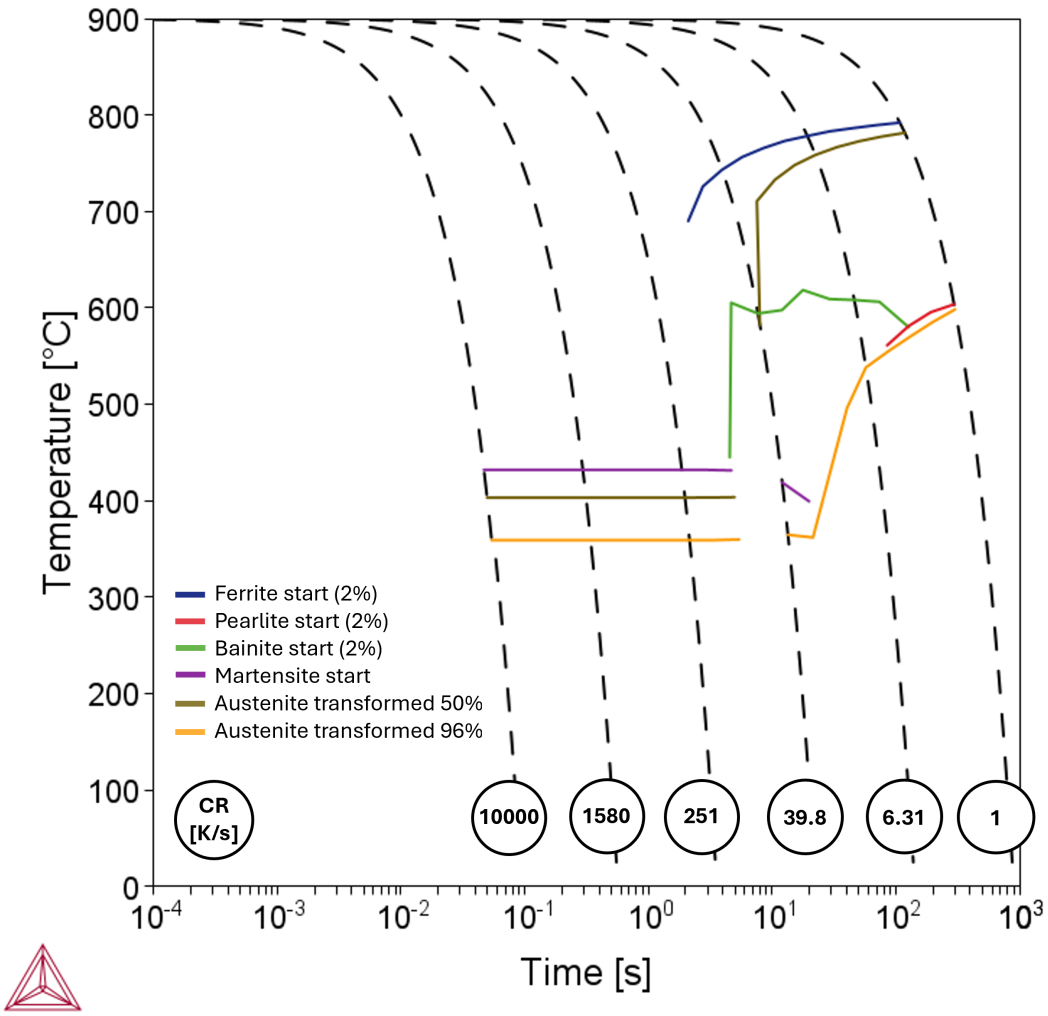

Figure 3.3: CCT diagram simulating the resulting phase transformations after deforming (compressing) the austenite grains. With a simplified composition (0.05C-1.3Mn-0.2Si-Bal.Fe in wt%). No. of steps used was 15 and austenite grain size: 20 μm.

hindering interface motion, hence suppressing the martensite formation [14]. There is also a slight shift in the ferrite, bainite and pearlite curve to shorter times.

The TTT diagram (Figure 3.4) shows how the microstructure of the material changes over time at isothermally. It is interesting to observe how the bainite curve (green curve) behaves in the plot. It can be seen that bainite appears only after two seconds if held at those temperatures. This suggests that even a rate of 250 K/s would not be enough to obtain a fully martensitic microstructure.

3.2.1. Martensite Start Temperature

The M_s temperature is the temperature at which martensite starts forming. Similarly, the martensite finish (M_f) temperature is the temperature at which the martensite is fully transformed. Using the CCT curve from Figure 3.2, a value of 453.6 °C is estimated for the M_s temperature, and 382.4 °C for the M_f temperature. To enable comparison, M_s temperatures were also calculated using empirical equations reported in literature. The results have been summarized in Table 3.2.

Based on the M_s values calculated empirically, an average M_s temperature of 491.0 °C was found. This is 37.4 °C higher than the value estimated by Thermo-Calc. This difference is meaningful but not unexpected. The discrepancy can be attributed to the influence of alloying elements on the M_s temperature, which may increase or decrease depending on composition. Since not all predictive equations account for the same alloying elements, the observed differences are therefore understandable. For instance, Nb, Cu, Cr, Mo, Ni, C and N decrease the M_s temperature, and Al, Ti, V and Co increase the

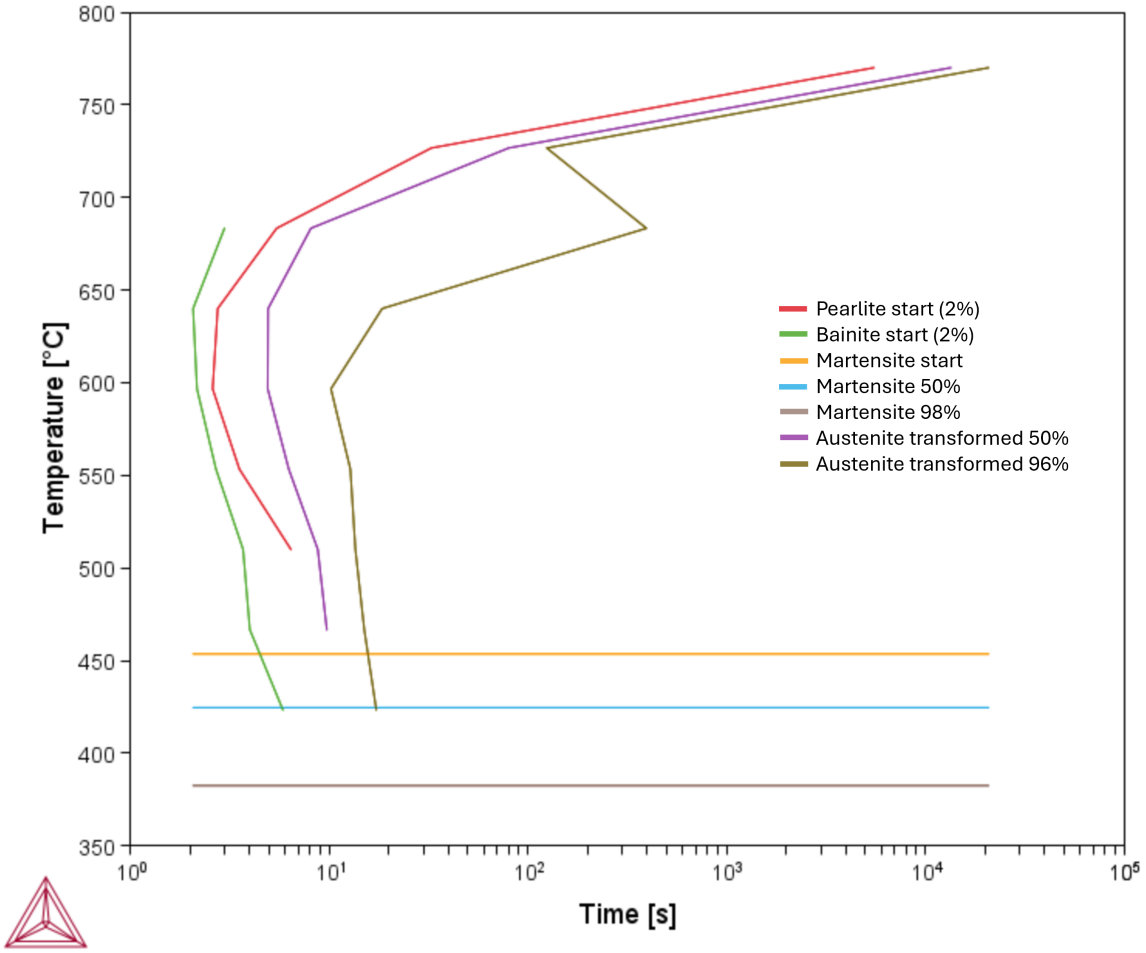

Figure 3.4: TTT diagram of the sample under investigation calculated with Thermo-Calc.

Table 3.2: Comparison of M_s temperature predictions. The equations used can be found in Appendix A.2.

M_s **Temperature Calculation**	M_s **Temperature [°C]**
Thermo-Calc	453.6
van Bohemen [31]	494.0
Kung & Rayment (mod. St&H) [32]	492.9
Steven & Haynes [33]	494.4
Ishida [34]	497.1
Andrews [35]	476.8

M_s temperature [32]. Another reason is that empirical equations typically do not account for variations in the prior austenite grain size, which can also significantly influence the M_s temperature.

3.2.2. Bainite Start Temperature

To calculate the bainite start (B_s) temperature, the TTT diagram (Figure 3.4) was used, as well as empirical equations from van Bohemen [36] and Steven & Haynes [33], which were also derived from TTT results. The results can be found in Table 3.3. Note that the equation from van Bohemen [36] was validated for samples with a carbon content of 0.10-1.9 wt.%, however, the sample under investigation contains 0.05 wt.% C, hence, this calculation is an extrapolation. The ~ 20°C difference between Thermo-Calc and the empirical B_s calculations can be attributed to experimental and methodological differences between all three methods.

Table 3.3: Comparison of B_s temperature predictions. The equations used can be found in Appendix A.3.

B_s **Temperature Calculation**	B_s **Temperature [°C]**
Thermo-Calc (TTT)	683.3
van Bohemen [31]	705
Steven & Haynes [33]	703.8

3.2.3. Austenite Temperatures

Upon heating, A_{c1} is the temperature at which the austenite grains start to form, and A_{c3} where the grains are fully austenitic. Using the equations proposed by Trzaska [37] (Appendix A.4), the calculated austenite transformation temperatures were A_{c1} = 724.95°C and A_{c3} = 874.75°C. The used equations are applicable for a range of mass concentrations of elements, based on 500 steel compositions tested [37]. The only difference is that the minimum carbon content for which this equation is applicable is 0.06wt% C, and the sample under investigation has 0.05wt% C.

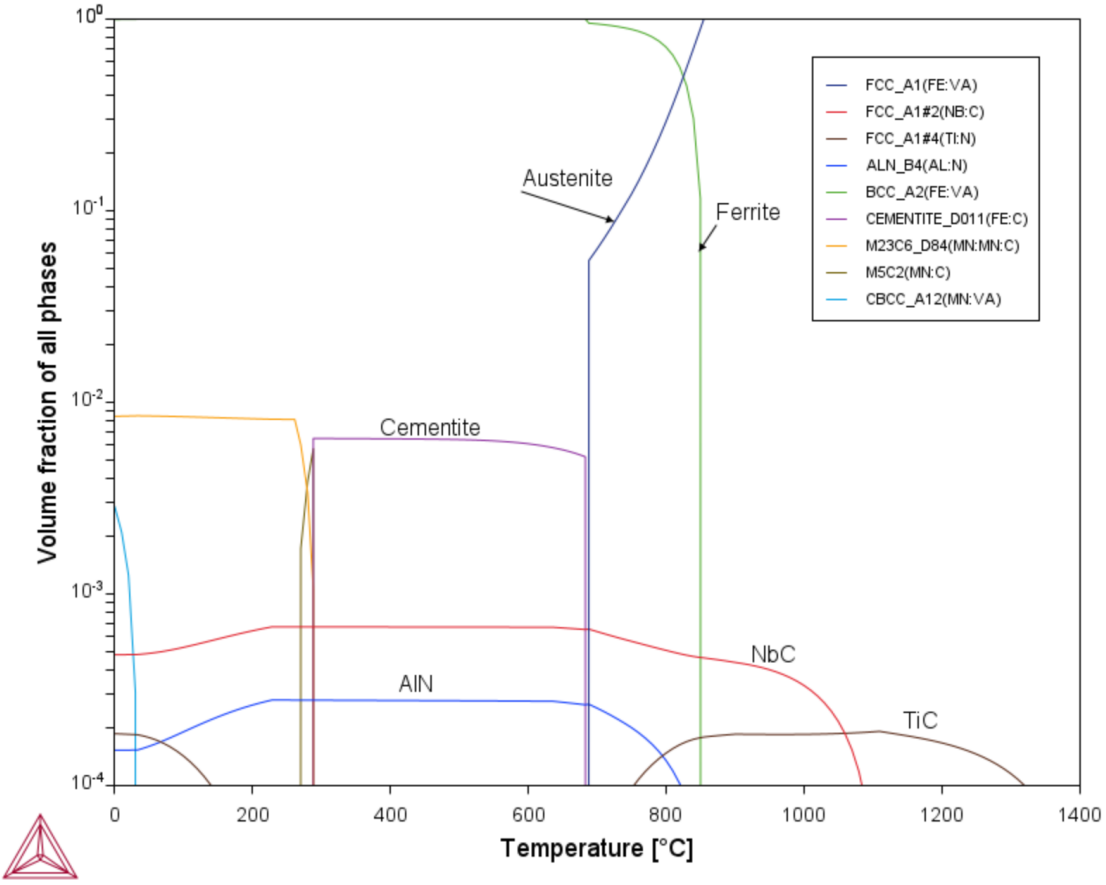

Figure 3.5: Calculated equilibrium phase fractions as a function of temperature for the sample under investigation. The diagram shows the stability ranges of key phases across the temperature range from 0 to 1400 °C.

The equilibrium phase fractions as a function of temperature for the material were plotted using Thermo-Calc, as can be seen in Figure 3.5. From the diagram, the equilibrium transformation temperatures were found to be A_{e1} = 688 °C and A_{e3} = 853 °C. These temperatures correspond to equilibrium conditions; therefore, the subscript e is used by convention.

No empirical equations were identified in literature for calculating the austenite transformation temperatures during cooling (A_{r1} and A_{r3}). Since, these temperatures are commonly determined

experimentally using differential thermal analysis (DTA). In a study by Bharadwaj et al. [7], the transformation behavior of a Nb,Ti-microalloyed low-carbon HSLA steel during continuous cooling was investigated, and the austenite transformation temperatures were identified. Although the exact chemical composition of this material is not specified, it is comparable to the material used in the present study due to the microalloying elements present and the low carbon content. In their work, the material was heated to 1100 °C, held for 3 minutes at this temperature, and subsequently cooled at different rates. For a cooling rate of 1 K/s, transformation temperatures of A_{r3} = 856 °C and A_{r1} = 762 °C were reported.

3.3. Dilatometry

The dilatometer DIL805 was used to heat treat and compress the samples. For every sample, the initial length and diameter were measured prior to testing and implemented as input parameters in the program. To avoid shifts in temperature readings, the same thermocouple was used for all tests. Before every test, the hydraulic was shifted to a position of 24.6 mm and the vacuum was started. The atmosphere was vacuum He and only when the system measured a pressure of 2.6e-4 mbar, the experiment was started. The treatment done on the samples can be visualized in Figure 3.6. The first compressive deformation (ε_1) applied was 0.3 for all samples. However, the second compressive deformation (ε_2), was variable with values of 0, 0.3, and 0.5. Both deformation steps had a strain rate of 5 s^{-1} for all the samples. For the final cooling step, four cooling rates were used: 1, 10, 50 and 150 K/s. A summary of the samples tested can be found in Table 3.4. Due to the limited availability of samples, the samples cooled down at 10 K/s were only deformed at 0.0 and 0.3.

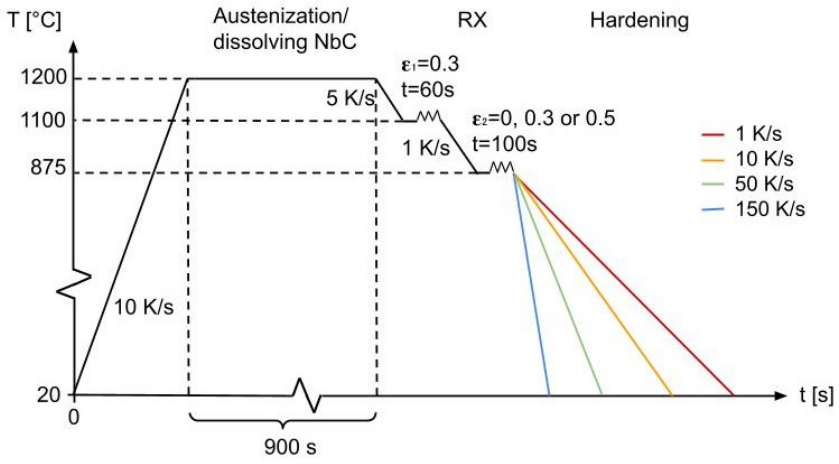

Figure 3.6: Temperature-time profile of the dilatometry deformation experiment showing heating, austenization, recrystallization (RX), deformation, and subsequent hardening under different cooling rates.

Table 3.4: Summary of the samples tested with the dilatometer.

Cooling rate [K/s]	**Second deformation step** (ε_2)
1	0.0, 0.3, 0.5
10	0.0, 0.3
50	0.0, 0.3, 0.5
150*	0.0, 0.3, 0.5

Now the steps chosen for the temperature-time profile (Figure 3.6) will be explained. Heating the sample up to 1200 °C and holding was done to dissolve the NbC precipitates. As was seen in Figure 3.5 (red curve), NbC dissolve above approximately 1100 °C. Therefore a temperature of 1200 °C for a holding time of 900 seconds should be sufficient for a full dissolution. NbC was an issue that, if not dissolved, would cause pinning and inhibit complete recrystallization of the austenite grains. Due to the long isothermal holding, the austenite grains would be very large in size, and the microstructure

analysis would lead to poor statistical representativeness [38]. Therefore, a first deformation step (ε_1) was introduced to refine the austenite grain size. After slow-cooling the sample to 875 °C, the sample is held at this temperature for a 100 seconds to homogenize the temperature gradient throughout the sample. The choice of a variable second deformation step (ε_2) was made to investigate the influence of deformation on the phase transformation kinetics and grain size. Similar to industrial processes, hot rolling is always conducted above the austenitic region, hence the choice of deforming in those temperatures [7]. Lastly, the different cooling paths were selected to produce distinct transformation products.

An issue was encountered with the samples with a cooling rate of 150 K/s (*), where the dilatometer did not manage to reach that rate. This is due to differences in temperature between the component and the quenching medium as the temperature goes down. During cooling, heat stored in the furnace and quartz push-rods flows back into the specimen, severely limiting the cooling rate [39]. The effective cooling rates were recorded and a distinct change in slope was observed, with a very steep initial gradient from 875 to 500 °C corresponding to a rapid cooling rate (faster than 130 K/s), followed by a more gradual slope from 500 °C to room temperature (slower than 80 K/s). A summary of the actual cooling rates measured for these samples can be found in Table 3.5. For clarity, and unless otherwise stated, samples processed under this condition are referred to as the high cooling rate (CR_{max}) condition.

Table 3.5: Table summarizing the effective cooling rates measured by the thermocouples for the samples with a nominal cooling rate of 150 K/s.

ε_2	Cooling rate (800→500 °C) [K/s]	Cooling rate (500→100 °C) [K/s]	Average cooling rate [K/s]
0	292	79	99
0.3	197	64	95
0.5	137	54	77

To plot the results, the dilatometer graphs were generated using Python. The code used is based on code originally developed by Vannam Nguyen (Copyright 2023, Module 3 - Thermal Analysis, used with permission of the author). The code was modified and extended to enable separate visualization of heating and cooling curves, and to include first-derivative calculations as well as the transformation curves. The plots will be shown in the Results Section.

3.3.1. Determination of Phase Fractions

To determine the phase fractions present of those samples with two phases, the dilatometer data was used. The fractions during cooling were calculated using a derivative-based approach using Python, rather than the classical geometric lever rule. From the transformation curves, the inflection points detected were identified as the transformation start temperature of the second phase. This was calculated as the value were the second derivative of the transformation curve was zero. Then the transformed phase fraction at this temperature was obtained directly from the transformation curve by interpolation. This corresponded to the phase fraction of the phase that formed first (f_A) and the phase fraction of the section phase (f_B) was calculated using $f_B = 1 - f_A$.

3.4. Optical Microscopy

To analyze the microstructure after the TMP, the compressed cylindrical samples were cut along their longitudinal axis using the cutter Struers Accutom 100, producing two semi-cylindrical halves (Figure 3.7). The blade used was 50A15, operated at 0.1 mm/s and 300 rpm, over a cutting distance of 11 mm. Only one half was further prepared by sanding, polishing, and etching. Sanding, with Struers LaboPol-21, was performed sequentially with grits P320, P800, P1200, and P2000 under a constant water flow, for approximately 3 minutes per sanding paper. The sample was then cleaned in the ultrasonic bath, Branson 5510, for 5 minutes in an isopropanol solution. Polishing was carried out with a Struers LaboPol-5 at a rotational speed of 250 rpm using 3 μm and 1 μm polishing papers, using the corresponding polishing liquids for each step. This part was completed with a second ultrasonic cleaning for 5 minutes. Finally, the sample was chemically etched by covering its surface with 2% Nital for approximately 10 seconds, then rinsed with distilled water first and then isopropanol, and hair-dried.

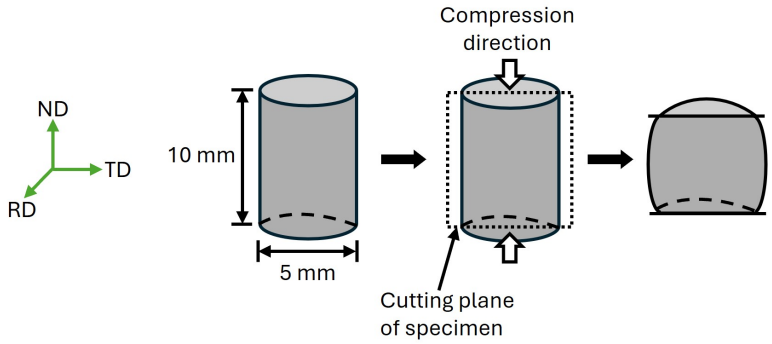

Figure 3.7: Illustration showing the sample orientation, cutting plane of the specimen, compression direction and the resulting compressed specimen. The ND-TD plane is in the plane of the paper (used for analysis), and RD is in the direction out of the plane.

This complete process made the samples picture-ready for the optical microscope (OM). The microscope used was a VHX Digital Microscope from Keyence. For all samples three pictures were taken, with a x200, x700 and x1000 magnification. The lighting selected for the images was the full coaxial and the pictures were always taken of the center of the sample, for consistency.

3.5. Vickers Hardness

To help understand the effect of grain size on the mechanical properties of the material, as well as aiding in the characterization of the phases present in each sample, combined with OM and the measured dilation signals, the hardness was measured with Vickers Hardness. This is a mechanical test that determines the material's resistance to permanent deformation, by applying a load and measuring the surface area of the diamond pyramid indent [40, 41].

First, the samples were embedded together per cooling rate, using the embedding machine Struers CitoPress-5. The samples had to be sanded and polished again up to 3 μm, following the same procedure as explained in Section 3.4. The HV10 hardness testing method, with a selected applied load of 10 kgf, was chosen. This was decided as a suitable load given the morphology and dimensions of the sample. To ensure reproducibility, five evenly distributed indentations were made across the surface of each sample. The hardness value was calculated automatically by the testing machine according to the following equation:

$$HV = \frac{2Fsin\frac{136^\circ}{2}}{d^2} \approx 1.854\frac{F}{d^2}, \tag{3.1}$$

where F is the load in kgf and d is the mean of the two diagonals of the diamond pyramid (d_1 and d_2) measured in μm.

3.6. Mean Linear Intercept Method

To further quantify the effect of prior deformation on the microstructure of the samples, the average grain size was measured using the OM images as well as the IPF maps (explained in Section 3.7). For the OM images, the mean linear intercept (M.L.I.) method was used. This method is part of the ASTM E112 standard [42], a well-known tool for measuring grain sizes in materials. The M.L.I. method consists on measuring the number of intersecting grains along a horizontal line drawn across the OM image [42]. The average grain size is taken from the results of five parallel lines, which were equally distanced across the image. For statistics and visualization, the images used were those with the 50 μm scale bar. This method was conducted using the software Fiji, which is a scientific image analysis tool from ImageJ [43].

The first step is the image calibration; the scale bar has to be measured, and then the magnification (M) can be calculated (see equation below). In this case, Fiji has a "setting scale" function which allowed the calibration to be done automatically, based on the measured scale bar and the specification of the length of the scale bar, obtaining the unit of pixels/μm.

$$M = \frac{\text{Measured length of scale bar } [\mu m]}{\text{Actual length of scale bar } [\mu m]} \tag{3.2}$$

The second step is to calculate the grain size, in μm, by using the length of a horizontal line (across the image) and the number of grains intersected. These two steps were repeated five times per image and then the average grain size ($\bar{G}$) of each sample was calculated using:

$$\bar{G} = \frac{\mathrm{L}\,[\mu m]}{\sum \mathrm{N}}, \tag{3.3}$$

where L is the length of a parallel line (after calibration) and N is the number of grains intersected. However, $N = 1$ if the line crosses grains, but $N = 0.5$ if the line is tangential to a grain or at a triple point, and if the lines starts or finishes at a grain.

3.7. EBSD

Electron Back-Scatter Diffraction (EBSD) is a widely used technique for characterizing microstructures of the transformation products by analyzing the crystallographic orientations [44]. For the sample preparation, the samples were polished again with an additional OPS polishing step. This extra polishing step was done manually during 15 minutes per sample, finishing with an ultrasonic bath for 5 minutes. After these steps, the samples were ready to be tested using a JSM-IT800 Scanning Electron Microscope (SEM) from JEOL. The samples were analyzed using the 12.5 mm specimen holder, at an accelerating voltage of 15kV. The samples were estimated to have a tilt angle of 70° from the horizontal. The working distance was 16.0 mm in the Z direction. The scanned area was the ND-TD plane and the selected areas chosen were always in the center of the sample to ensure consistency. EBSD orientation mapping scans were performed at two different magnifications, x3000 and x500, with a step size of 0.1 μm and 0.2 μm, respectively. All images were visualized in the AZtec software (Oxford Instruments). The data was represented in inverse pole figure (IPF) maps, obtained along the X, Y, and Z directions, with the same color coding applied to all IPF maps, shown in Figure 3.8. IPF maps are used to represent the crystal orientation relative to a specific sample direction, either the rolling direction (RD), transverse direction (TD), normal direction (ND) [45].

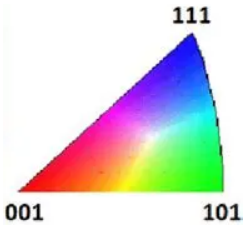

Figure 3.8: Color legend for IPF maps, indicating the crystal directions aligned with the sample directions.

3.8. EDAX OIM Analysis

To analyze the results obtained from EBSD, the EDAX OIM Analysis 8 software was used [46]. The EBSD data files were converted from .ctf file format to .ang using a Python script [47]. Note that the grains in the software are defined as the collection of pixels within a certain orientation range, known as the grain tolerance angle [48]. All the samples were first cleaned-up using the function "Cleanup dataset" (explained below), later the Image Quality (IQ), IPF and Grain images were generated and finally the grain size distributions were plotted (see Section 3.8.2).

Two clean-up step were done per sample, one clean-up type being grain dilation. For this type, the specifications were a grain tolerance of 5°, minimum grain size of 5 pixels, restrict cleanup to points with confidence intervals (CIs) less than 0.2, iterations: stop after 25% changed. The second clean-up type was neighbor orientation correlation (NOC) which is based on colors. The specifications were a grain tolerance angle of 5°, restrict clean-up to points with CIs less than 0.2, maximum clean-up level

of 5 pixels. These clean-up steps were selected because they produced the best visual results while ensuring that the microstructure was not removed. However, usually the clean-up step cleaned 0.1% or less of the pixels in the images. These parameters are of key importance for the analysis, and have a great influence on the grain size results, therefore, careful attention should be payed to them [48].

3.8.1. Grain Boundaries

To determine the grain boundary lengths, the properties of the IPF image were adjusted by adding rotation angle specifications; from 2 to 15° for the low-angle grain boundaries (LAGBs) and from 15 to 62.8° for the high-angle grain boundaries (HAGBs). This regenerated the IPF image with the grain boundaries (GBs). The software calculated the GB fraction of HAGBs versus LAGBs and the GB length of HAGBs and LAGBs separately, as well as the total GB length.

The GB fraction is useful to understand what type of GBs each sample has, and which type dominates in a sample. The GB length quantifies how many boundaries exist in a sample. It can also suggest grain refinement or sub-grain formation. The images with the largest magnification (with a 10 or 15 μm scale bar) was used for the GB analysis for all the samples for consistency. This was decided as this magnification used a smaller step size which would detect the sub-grain structure and details better.

The GB length data was normalized per unit area of each image. This is essentially the length density ($\mu m/\mu m^2$). To normalize the data, first the analyzed area (A) had to be calculated. For this, the EBSD files (in .ctf format) were revisited to find the step size (s) and the number of pixels in the x- (N_x) and y- (N_y) direction for each sample. Then the analyzed area could be calculated using:

$$A = (N_x \cdot s)(N_y \cdot s) = N_x \cdot N_y \cdot s^2 \tag{3.4}$$

The samples with CR = 1 K/s and CR_{max} had a step size of 0.1 μm, and 514 and 385 pixels for N_x and N_y, respectively. Whereas, samples with CR = 10 and 50 K/s, the step size used was 0.05 μm, and 428 (N_x) and 321 (N_y) pixels. Leading to unit areas of 0.495 and 1.37 mm^2, respectively.

Using this, the normalized GB length can be calculated:

$$L_A^i = \frac{L^i}{A}, \tag{3.5}$$

where i is the type of boundary, either total, HAGB or LAGB, and the subscript A is the analyzed area.

3.8.2. Grain Size Distribution

Besides the M.L.I. method for grain size calculation, the grain size distribution of the sample was computed using the EDAX OIM Analysis software, which computes the grain size diameter (in μm) against the number fraction. Two grain size distribution plots were generated, one for grains in the range of 0 to the maximum μm grain size of each sample, and another plot with the constraint that the minimum grain size was 1 μm. This allows to eliminate the grains which are identified by the software within a boundary or mis-indexed pixels, and measures the larger grains. The data from the plots are also presented in a table and summary statistics of the average grain size. These statistics are separated into two grain size methods: the number and the area method [48]. On one hand, the number method first averages the grain areas by dividing the total area of the image by the number of grains, and then converts this average area into a diameter [48]. On the other hand, the area method accounts for the fact that larger grains occupy more area. Grains with larger areas contribute more to the calculation, so a weighted average area is determined [48]. This weighted average area is then used to calculate the average grain diameter. The grain size distribution was computed for all samples, for both the images with x500 and x3000 magnification.

4

Results & Discussion

4.1. Characterization of Initial Microstructure

The untreated sample, as-received from TATA Steel, was analyzed using OM to understand how the starting microstructure of the material under investigation looks like. This sample will be referred to as the *original* sample.

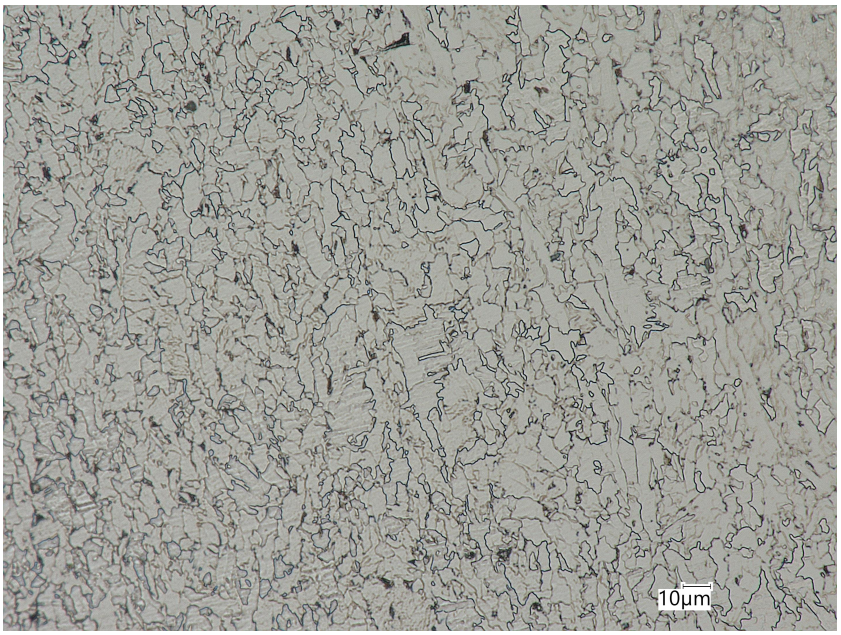

Figure 4.1: OM image of the original sample.

The exact TMP process taken to obtain this material is unknown due to confidentiality reasons. However, it is known that the original sample was cooled to an appropriate temperature to obtain a mixture of polygonal and granular bainitic ferrite. As it can be seen from Figure 4.1, the microstructure of the investigated steel appears as a very irregular microstructure which consists predominantly of ferrite with a low fraction of a second phase, likely cementite.

The OM image of the original sample looks very similar to a sample corresponding to granular bainite, as shown by Zajac et al. [8] (Figure 2.3). The material in the study [8] had a similar carbon content as the sample under investigation (only 0.005 wt.% less of carbon). This microstructure also consists of irregular ferrite, the absence of a well-defined lath morphology and with second phases distributed between grains, which could be pearlite or cementite [8].

4.2. Dilatometry

The dilatometer plots illustrate the transformation curve (in %) against temperature (T) on cooling for all the samples tested. The temperature axis is plotted from low to high values, therefore, the transformation curve progresses from 100% to 0% during cooling. For the complete plots showing the change in length (ΔL) and the first derivative of the ΔL-T curve (dL/dT), refer to Appendix B.1.

From these dilatometer plots, the transformation start (T_s) and finish (T_f) temperatures for every sample, as well as the transformation range (ΔT_{transf}) and the duration of the transformation (t_{transf}) are summarized in Table 4.1. The results are analyzed below. It is important to note that these values correspond to the overall transformation for each sample and have not been separated into individual phase transformations in cases where more than one phase forms.

CR [K/s]	ε_2	T_s [°C]	T_f [°C]	ΔT_{transf} [°C]	t_{transf} [s]
1	0.0	790	625	175	175
	0.3	800	685	115	115
	0.5	805	715	85	85
10	0.0	680	575	105	10.5
	0.3	790	605	185	18.5
50	0.0	625	420	205	4.1
	0.3	630	520	110	2.2
	0.5	665	600	65	1.3
CR_{max}	0.0	530	385	145	1.5
	0.3	530	370	160	1.7
	0.5	575	420	155	2.0

Table 4.1: Transformation start temperature (T_s), finish temperature (T_f), transformation range (ΔT_{transf}), and transformation time (t_{transf}) as a function of cooling rate (CR) and prior deformation ε_2.

For the samples with CR = 1 K/s, the T_s is similar to the value found in the simplified CCT diagram for ferrite (Figure 3.2), near 800 °C. Due to the slow cooling rate and the identified transformation temperatures, this microstructure corresponds to ferrite. It is also observed that as deformation increases, t_{transf} decreases. Increased dislocation density enhances stored energy and significantly increases the availability of nucleation sites, particularly at grain boundaries and within subdivided grains [22]. This accelerates diffusional transformations of austenite to ferrite and pearlite [14].

The samples with CR = 10 K/s show a decrease in the T_s and T_f compared to the samples with CR = 1 K/s. A faster cooling rate shifts the phase transformation to lower temperatures by reducing the time available for diffusion-controlled processes. For the sample with ε_2 = 0.3, the slight increase in the t_{transf} and T_s temperature, compared to the sample with ε_2 = 0.0, is associated with the change in the morphology of the ferrite grains. This will be seen later.

The samples with CR = 50 K/s show a further decrease in the transformation temperatures compared to the samples with slower cooling rates. The T_s values for the samples with ε_2 = 0.0 and 0.3 are similar to the values found for the bainite start temperatures (Table 3.3). This is because the transformation mechanism of the phases present is both diffusional and displacive, the latter proceeding more rapidly. However, the sample with ε_2 = 0.5 is only diffusional due to the formation of ferrite. This happens because deformation accelerates the phase transformations controlled by diffusion [49]. Deforming the austenite grains implies a larger grain boundary length in 2D, and area in 3D, increasing the nucleation density of diffusional phases and leading to higher T_s temperatures and shorter t_{transf} [14].

The T_s values for the samples with CR_{max}, and with ε_2 = 0.0 and 0.3 are closer to the calculated martensite start temperatures (Table 3.2). As deformation increases, from ε_2 = 0.3 to 0.5, the T_s and T_f values increase. This can again be due to a change in the transformed phase, possibly due to a shift in the CCT diagram.

Combining all the results from Table 4.1, the trend observed is that for each cooling rate both the T_s and T_f increase with increasing strain, except for CR_{max}, where no clear trend is observed. This increase in the transformation temperatures can be attributed to the increase in the dislocation density due to deformation which leads to an increase in the number of nucleation sites [50]. This facilitates phase

nucleation and accelerates the transformation kinetics [50], seen by a reduction in t_{transf}. The T_s and T_f increase with deformation imply a shift in the CCT curves shift. This effect is evident for cooling rates of 50, and CR_{max} K/s, indicating that different microstructural constituents can form at the same cooling rate depending on the applied deformation. This will be seen in a later section.

For most samples, the *dL/dT* curves exhibited significant noise, making it difficult to clearly identify phase transformation temperatures. At elevated temperatures, material softening causes the holding force to influence the measured displacement, introducing apparent length variations. In other cases, noise originated from fluctuations in the high-frequency (HF) induction power (see Appendix B.2). As temperature changes, particularly during phase transformations, the electrical resistivity and magnetic properties of the specimen vary, altering electromagnetic coupling between the induction coil and the sample. This leads to continuous power adjustments, which manifest as fluctuations in the HF signal and appear as noise in the derivative curve [39].

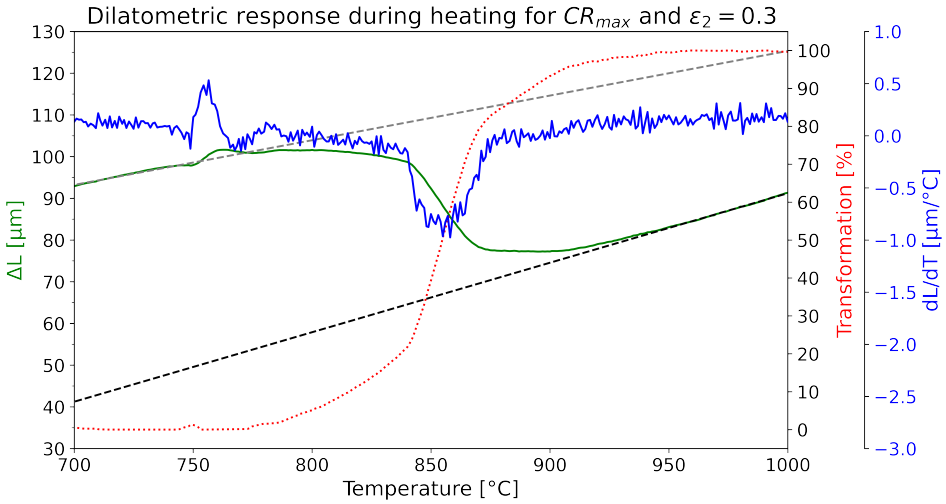

Figure 4.2: Example of a dilatometer plot on heating with a small contraction followed by an expansion peak. This sample has a posterior $\varepsilon_2 = 0.3$ and quench.

The dilatometer plots were also plotted on heating and the same behavior was observed for all the samples. This is a good indication that the thermocouples used were measuring accurately. However, most samples were found to have a small contraction followed by an expansion peak in the ΔL curve, which was also seen in the derivative curve (*dL/dT*). Figure 4.2 shows an example of this. The contraction peak is due to the change in magnetic properties of the material near the Curie temperature. The Curie temperature corresponds to the transition from ferromagnetic to paramagnetic behavior, which is normally accompanied by a volume contraction due to the loss of electronic exchange interactions [51]. The expansion peak is specific to induction-heated systems and is associated with the applied radio-frequency (RF) electromagnetic field, specifically in quench dilatometer. Under the RF field, additional spin splitting of the conduction electron bands modifies the electron-phonon interactions, leading to an abnormal thermal expansion [51].

The reproducibility and reliability of the dilatometer measurements and thermocouple response were verified using duplicate samples subjected to identical heat treatment and compression conditions (Appendix B.3). The resulting transformation behavior is highly consistent, with comparable start and finish temperatures.

4.3. Combining Dilatometry and Optical Microscopy

To characterize the microstructures, the transformation (in %) versus temperature graphs will be analyzed in combination with the OM images. The temperature at the inflection point of the transformation curve was identified as the start temperature of the second phase, and this value was subsequently used to determine the corresponding phase fraction (Appendix B.4).

4.3.1. CR = 1 K/s

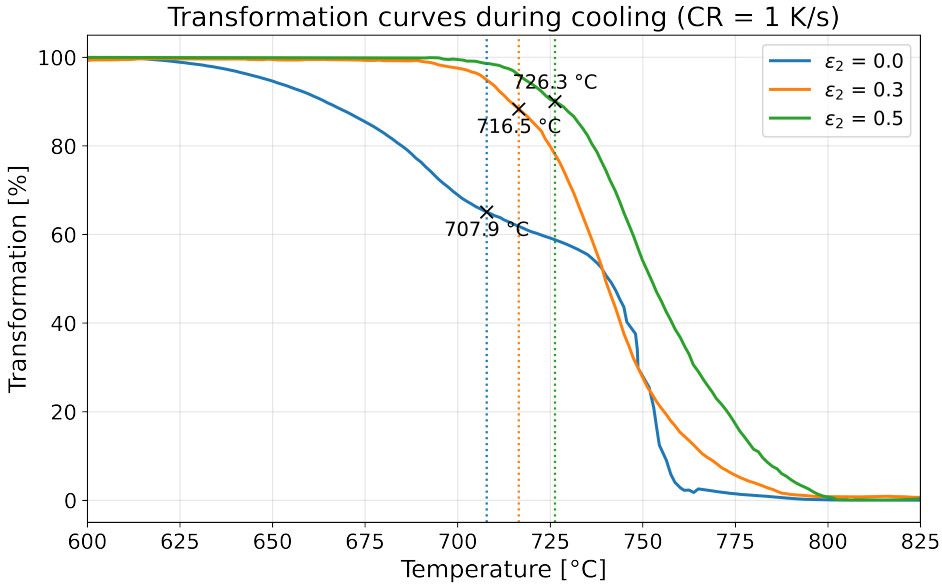

(a) Transformation curves (on cooling) for samples with a cooling rate 1 K/s.

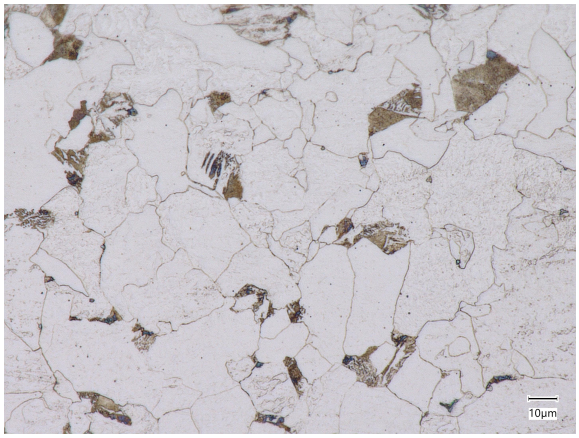

(b) $\varepsilon_2 = 0.0$

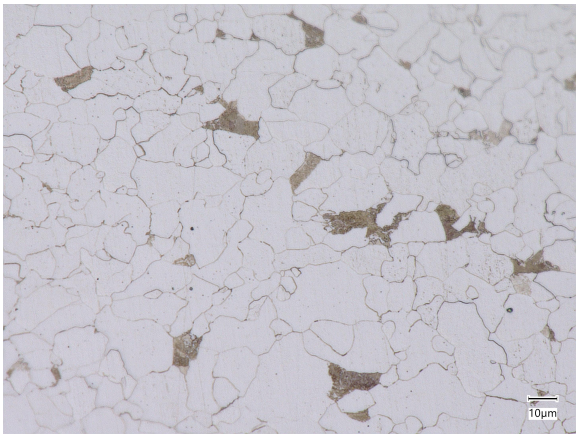

(c) $\varepsilon_2 = 0.3$

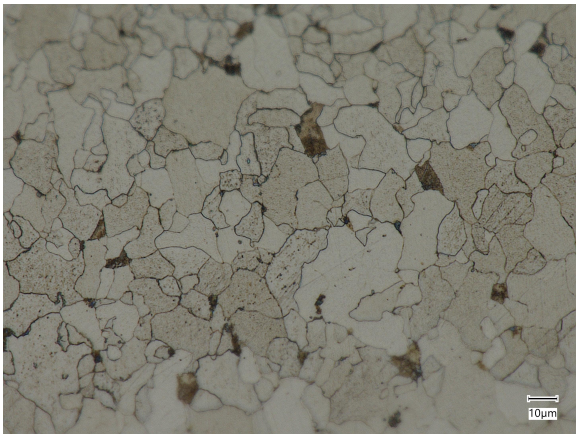

(d) $\varepsilon_2 = 0.5$

Figure 4.3: OM images for different values of ε_2 for samples cooled at 1 K/s. The labeled temperatures correspond to the pearlite start temperature. The measured pearlite fractions are (b) 34.9%, (c) 11.7%, and (d) 10.0%.

The transformation behavior during cooling at 1 K/s is shown in Figure 4.3(a). The corresponding OM images are presented in Figure 4.3(b)-(d). In all cases, the microstructure consists of ferrite (light regions) and pearlite (dark regions). The ferrite exhibits an equiaxed morphology, known as polygonal ferrite. Based on the pearlite start temperatures indicated in the transformation curves, the calculated pearlite fractions are 34.9%, 11.7%, and 10.0% for samples with ε_2 = 0.0, 0.3, and 0.5, respectively. However, these values do not correlate well with the OM images shown in Figure 4.3(b)-(d), where the visually estimated pearlite fraction seems to be significantly lower, particularly for ε_2 = 0.0. To compare these results, an image analysis approach was applied using Fiji software [43]. The OM images were converted to grayscale and subsequently thresholded to generate black-white images. In this procedure, the white regions were identified as ferrite, and the dark regions were attributed to pearlite. The resulting pearlite fractions were 8.3%, 5.6%, and 10.3% for samples with ε_2 = 0.0, 0.3, and 0.5, respectively. These values are in better agreement with the qualitative microstructural observations. The remaining discrepancy observed for the ε_2 = 0.5 sample can be attributed to stronger etching contrast, which led the software to partially classify most of the grain boundaries as pearlite, thereby overestimating the pearlite fraction. For reference, an equilibrium pearlite fraction of approximately 4% was calculated for the present steel composition using the phase diagram. This value is closer to the fractions estimated from the OM images; however, the reason for the significant deviation from the lever rule calculations remains unclear.

However, independent of this methodological limitation, a pronounced decrease in pearlite fraction is observed with increasing prior deformation. The increased stored energy and defect density in deformed austenite promote earlier ferrite nucleation [52], reducing the available austenite volume and enriching the remaining austenite in carbon. This can happen since enhanced carbon diffusion along deformation-induced defects further accelerates ferrite growth, thereby suppressing pearlite formation [53]. Consequently, the pearlite fraction decreases, while the interlamellar spacing is reduced, indicating a higher local carbon content within the remaining pearlite.

4.3.2. CR = 10 K/s

From Figure 4.4(a), no second phases were identified in the phase transformations of these samples. The OM images shown in Figure 4.4(b) and (c) show a microstructure with irregular grains, corresponding to acicular ferrite. This form of ferrite is a non-equiaxed phase that forms at a slightly higher temperature range than upper bainite, and it is known for its needle-like grains, nucleating inside austenite grains at nonmetallic inclusions [11]. Acicular ferrite grows through a diffusionless transformation [54], it rejects carbon into the remaining austenite, the carbon-enriched austenite transforms during cooling into pearlite or bainite [55]; therefore, the darker regions observed in the OM images likely correspond to pearlite.

Bharadwaj et al. [7] reported that increasing the cooling rate in a steel of comparable composition led to a transition in ferrite morphology from polygonal to acicular (Figure 2.2). The former similar to Figure 2.2(a) and (b), and the latter similar to Figure 2.2(c)-(e). This change was attributed to a shift in the growth mechanism from diffusion-controlled to interface-controlled [7]. Diffusion-controlled growth occurs when the advance of a transformation interface is limited by the diffusion of solute atoms ahead of it, whereas interface-controlled growth occurs when diffusion is sufficiently fast and the transformation rate is governed by the intrinsic mobility of the interface [7].

Bharadwaj et al. [7] observed acicular ferrite only at a cooling rate of 30 K/s, whereas Figure 4.4 shows acicular ferrite at a lower cooling rate (10 K/s). Zhao et al. [11] reported that Mn, Nb, Ti, and Mo promote acicular ferrite formation over polygonal ferrite. The present material contains Mn as well as Nb and Ti microalloying additions, whereas the steel studied by Bharadwaj et al. contained only Ti. This difference in alloying content likely explains the formation of acicular ferrite in Figure 4.4.

The difference in the sample with ε_2 = 0.0 versus the sample with ε_2 = 0.3 is that the latter also includes equiaxed (polygonal) grains. This can also be seen in the transformation curve of this sample, where the slope change around a temperature of $\sim$ 697°C corresponds to the start of the transformation of acicular ferrite. This change can be seen since the transformation for polygonal ferrite and acicular ferrite are kinetically separated.

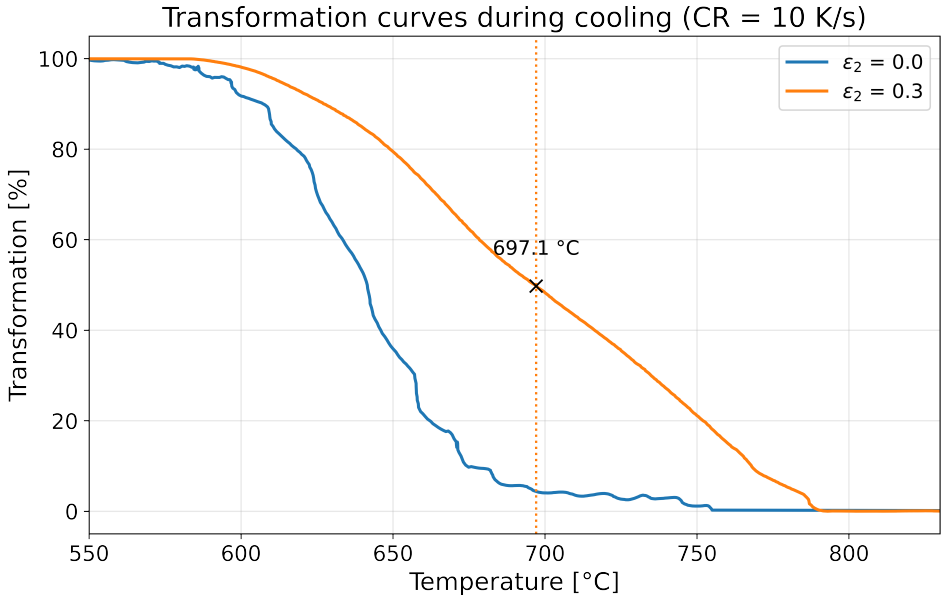

(a) Transformation curves (on cooling) for samples with a cooling rate 10 K/s.

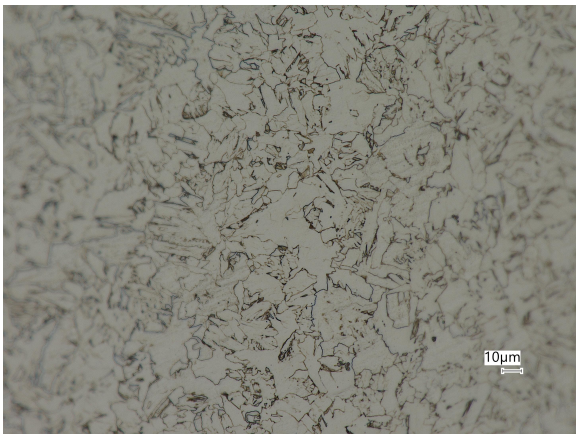

(b) ε_2 = 0.0

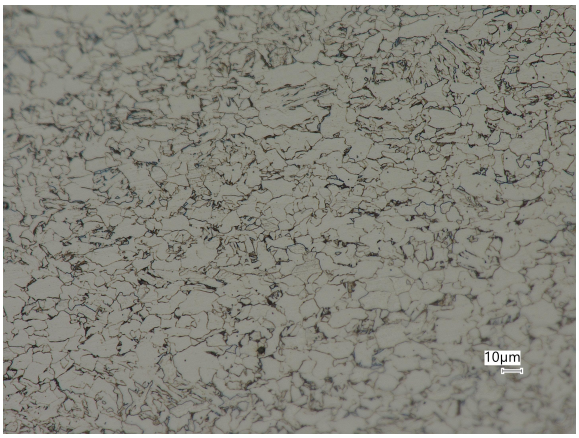

(c) ε_2 = 0.3

Figure 4.4: (a) Combination of the transformation curves (on cooling) for the samples cooled down at 10 K/s, and (b) and (c) the corresponding OM images for different values of ε_2. The fluctuations in the transformation curve of the sample with ε_2 = 0.0 corresponds to variations in the HF power.

4.3.3. CR = 50 K/s

Higher cooling rates lead to a displacive atomic growth mechanism, suppressing atomic diffusion and creating non-equilibrium phases such as martensite and bainite [56, 57]. From In Figure 4.5(a), a transformation start temperature of approximately 620°C is experimentally observed for the sample with ε_2 = 0.0. The calculated B_s temperature from Thermo-Calc is approximately 684°C, suggesting that bainite formation occurs in this material when cooled at 50 K/s. Bainite can be seen from the larger grains containing carbides (labeled with red arrows) [58]. Another phase transformation is observed at ~ 540°C. Earlier, an average M_s temperature of ~ 491°C was calculated (Table 3.2), which also suggests that the second transformation forms martensite. Analyzing Figure 4.5(b), the needle-like features (labeled with a blue arrow) are characteristic of martensite.

However, for ε_2 = 0.3, martensite is no longer formed, but instead acicular ferrite and bainite, as the second phase, can be seen (Figure 4.5(c)). For ε_2 = 0.5 (Figure 4.5(d)), the microstructure becomes ferritic, with a mixture of polygonal ferrite and elongated ferrite.

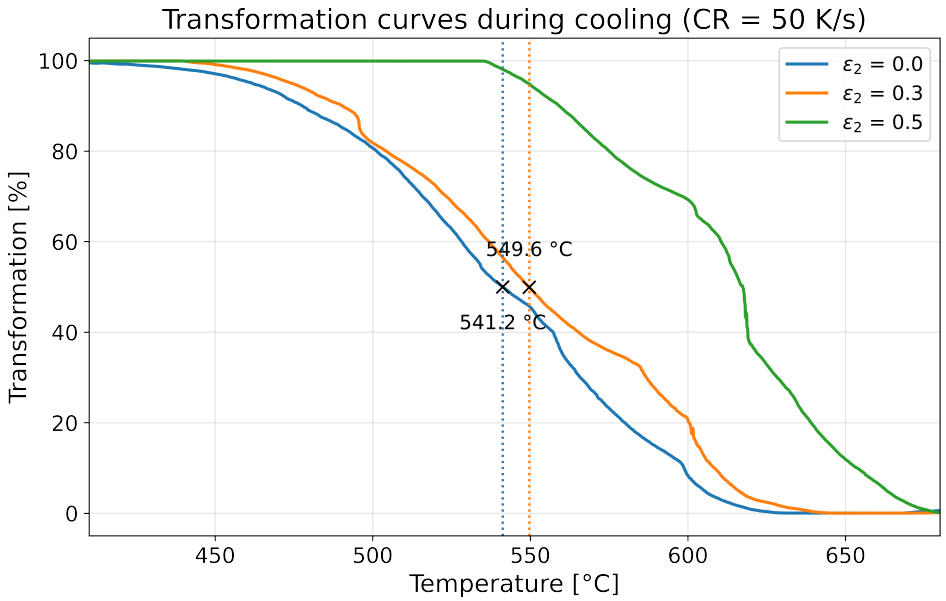

(a) Transformation curves (on cooling) for samples with a cooling rate 50 K/s.

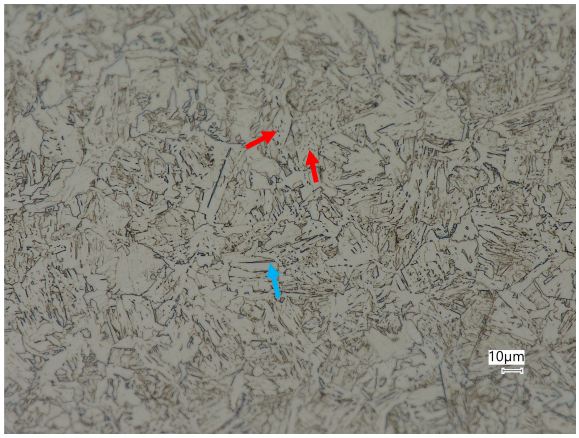

(b) $\varepsilon_2 = 0.0$

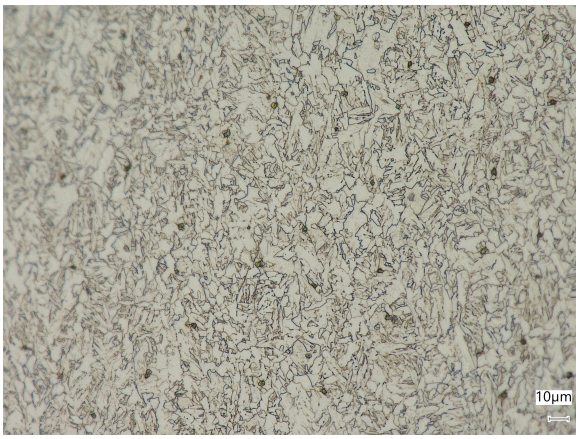

(c) $\varepsilon_2 = 0.3$

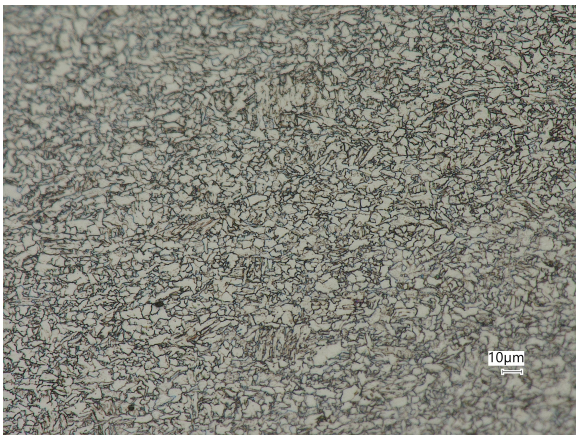

(d) $\varepsilon_2 = 0.5$

Figure 4.5: (a) Combination of the transformation curves (on cooling) for the samples cooled down at 50 K/s, and (b), (c) and (d) the corresponding OM images for different values of ε_2. The arrows in image (b) indicate features characteristic of a bainitic (red) and martensitic (blue) microstructure.

4.3.4. CR_{max}

Higher cooling rates, as explained previously, result in a displacive atomic growth mechanism. Due to the high strain energy in these non-equilibrium phases, as is the case for bainite and martensite, their morphology is characterized by needle- or plate-like structures [57].

From the dilatometer curve (Figure 4.6(a)), the transformation start temperature of the sample with no deformation is at ~ 500°C. When looking back at the calculated M_s temperature, ~ 491°C was obtained. From Figure 4.6(b), the microstructure has irregularly oriented, needle-like structure, characteristic of a martensite. For these two observations, it can be said that this sample is martensitic.

The sample with $\varepsilon_2 = 0.3$ can be attributed to a combined transformation of martensite and bainite, due to the morphology seen in the microstructure. The darker etched areas with needle-like grains correspond to martensite, whereas the lighter etched areas correspond to bainite. Probably both transformations occurred simultaneously, therefore, change in the slope of the transformation curve can be identified.

For the sample with the $\varepsilon_2 = 0.5$, it can be seen how the microstructure become a a mixture of polygonal and elongated ferrite, very similar to the one observed in Figure 4.5(c). Even though a second phase seems to start forming at a temperature of ~ 466.4°C, due to a change in slope in the transformation curve (Figure 4.6(a)), only a ferritic microstructure is observed. The results obtained for the samples cooled down at 50 K/s and CR_{max} show a similar trend, where as deformation increases, the growth mechanism changes from a displacive character to a diffusional character.

4.4. Mean Linear Intercept Method

The results obtained from the grain size measurements using the M.L.I. method can be found in Figure 4.7. The samples labeled with a "X" could not be measured due to a complex grain structure.

From the plot, an increase in ε_2 leads to a decrease in the average grain size, for the samples cooled down at the same rate. In diffusional transformations, such as ferrite formation, the final grain size of the new phase is governed by the number of nuclei formed and their subsequent growth. A high nucleation rate, due to prior deformation in the austenite, combined with limited growth leads to a large number of fine grains [59]. This is consistent for the samples cooled down at 1 K/s.

Accelerated cooling promotes grain refinement by reducing the time available for grain growth, thereby producing a finer microstructure [59]. This is seen when the samples with $\varepsilon_2 = 0.0$ are compared, since the average grain size decreases with an increasing cooling rate. However, due to the different microstructures for the samples with CR = 50 K/s and CR_{max} with an increasing deformation, no comparisons can be made.

To further analyze the results, the %SD was calculated and plotted in Figure 4.8. This variable was calculated by normalizing the standard deviation with the mean grain size, and multiplied by 100. It is also known as the coefficient of variation. In the present context, the %SD of the average grain sizes of the samples provides an indication of the microstructural homogeneity of the sample; a high %SD reflects a wide distribution of grain sizes relative to the mean, corresponding to a more heterogeneous or irregular microstructure, whereas a low %SD indicates a more uniform grain size distribution. A clear trend is observed whereby the %SD decreases with increasing deformation, indicating a progressively more homogeneous grain size distribution.

Even though the M.L.I. method yielded interesting results, some issues were encountered during the analysis. As mentioned, two samples were not measured due to the difficulty in distinguishing between grains. This was the case for the samples with a martensitic or bainitic microstructure. A possible solution could be to use the IPF maps from EBSD instead, however, in EBSD-based measurements the estimated grain size is sensitive to the chosen misorientation threshold and step size. These images were also complex to analyze, therefore, for consistency, the OM images were used for all the M.L.I. measurements. Also, the IPF maps primarily display orientation contrast rather than true grain boundaries, and sub-grains or low-angle boundaries may be erroneously identified as grains. Consequently, the M.L.I. method depends on the measurement conditions and image interpretation chosen by the researcher, and therefore retains a degree of subjectivity. Further grain size analysis will be conducted using the software EDAX OIM Analysis in Section 4.7.2.

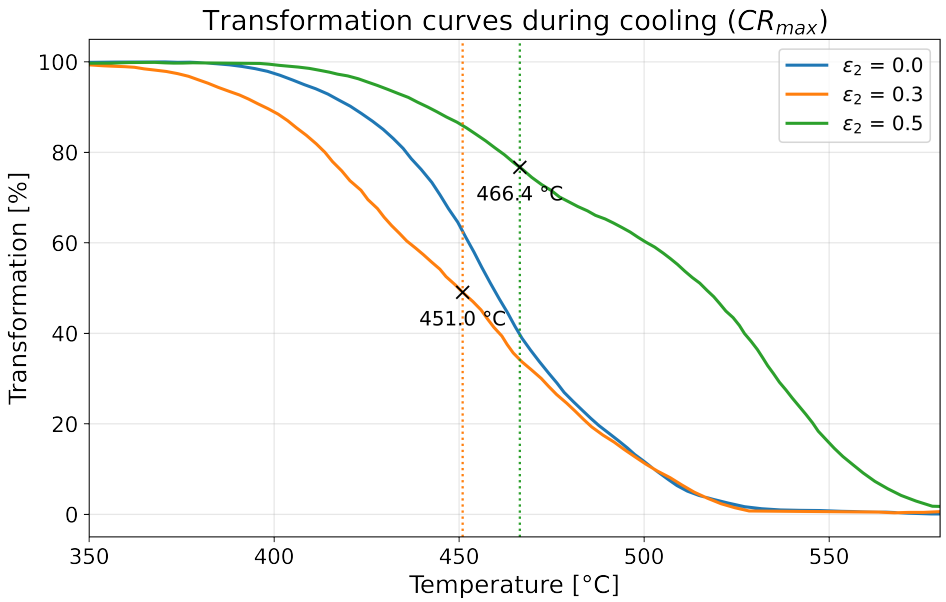

(a) Transformation curves (on cooling) for samples with a cooling rate CR_{max}.

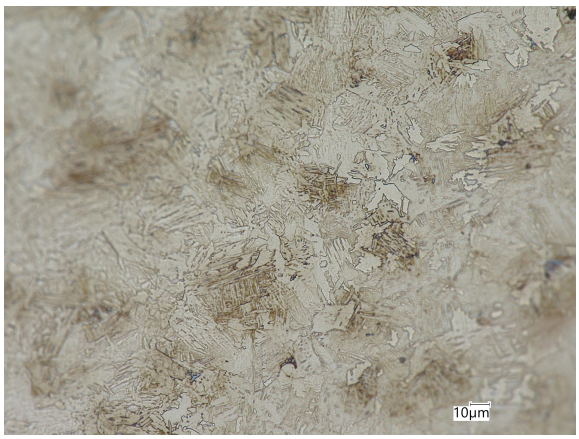

(b) $\varepsilon_2 = 0.0$

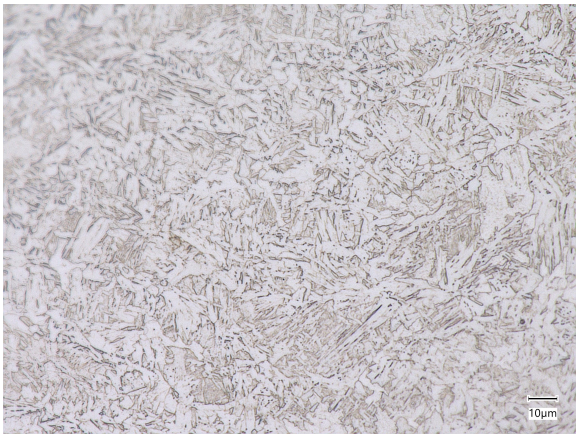

(c) $\varepsilon_2 = 0.3$

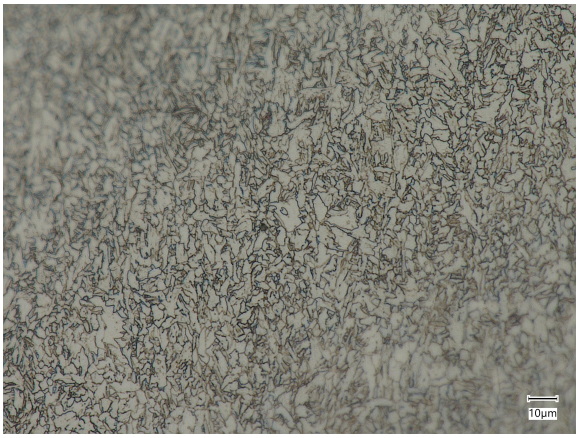

(d) $\varepsilon_2 = 0.5$

Figure 4.6: (a) Combination of the transformation curves (on cooling) for the samples cooled down at CR_{max} K/s, and (b), (c) and (d) the corresponding OM images for different values of ε_2.

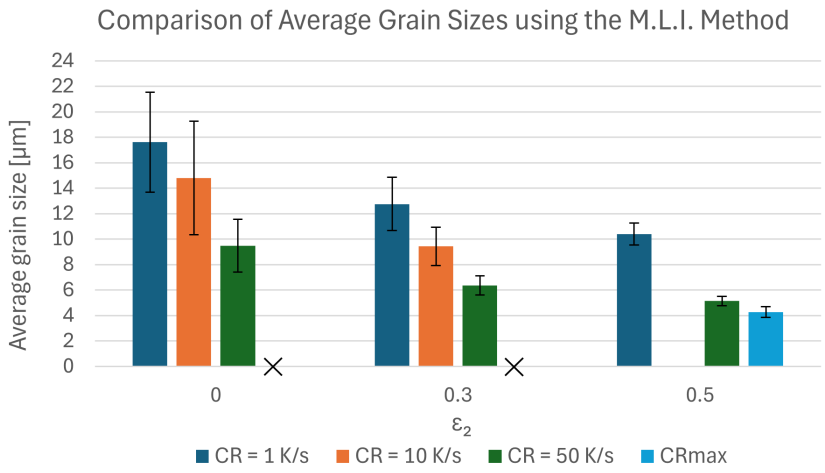

Figure 4.7: Average grain size as a function of ε_2 for different cooling rates. Error bars represent the standard deviation of five measurements. "X" denotes cases where measurements were not possible due to complex grain structures. No sample with $\varepsilon_2 = 0.5$ was tested at a cooling rate of 10 K/s.

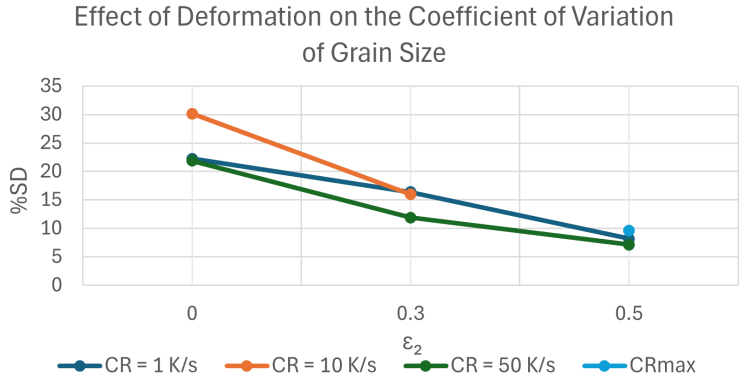

Figure 4.8: Coefficient of variation (%SD) of the average grain size as a function of ε_2 for different cooling rates.

4.5. Vickers Hardness

The hardness results have been plotted individually per cooling rate (CR), to understand the influence of deformation on the hardness of the material. At the end, a plot combining the results for all the CRs tested for all three deformation levels is also presented for comparison.

The samples cooled down at 1 K/s consist on ferrite (dominating) and pearlite, as was previously observed. As deformation increased, the average grain size was found to decrease, as well as the fraction of pearlite. This ferrite-pearlite distribution within a material has a large influence on its final mechanical properties [56]. From Figure 4.9, the hardness decreases with increasing prior deformation. The samples with a hardness of approximately 160 HV correspond to ferritic microstructures for this material composition, consistent with values reported in literature [18, 60]. However, once deformation is applied, the hardness appears to reach a plateau at approximately 145 HV10. This behavior can be associated with the pronounced reduction in pearlite fraction at $\varepsilon_2 = 0.3$, followed by only a minor additional decrease of 1.7 percentage points for $\varepsilon_2 = 0.5$. Pearlite consists of ferrite and cementite, with the latter contributing significantly to the hardness by restricting dislocation motion [6]. The small difference in pearlite fraction between the two deformed samples is therefore reflected in the apparent hardness plateau. Although the average grain size was observed to decrease with increasing deformation, which would typically be expected to increase hardness (according to the Hall-Petch relation), the overall hardness appears to be more strongly influenced by the phase constitution of the material.

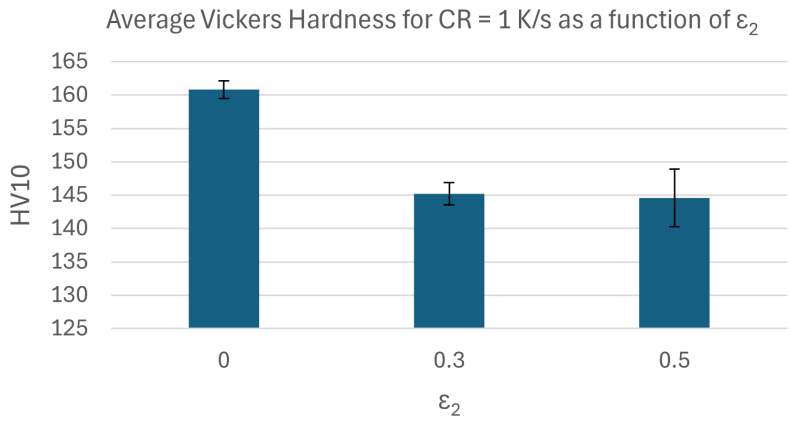

Figure 4.9: Average Vickers hardness (HV10) measured for samples processed at a cooling rate of 1 K/s as a function of the applied strain parameter ε_2. Error bars represent the standard deviation of five hardness measurements per condition.

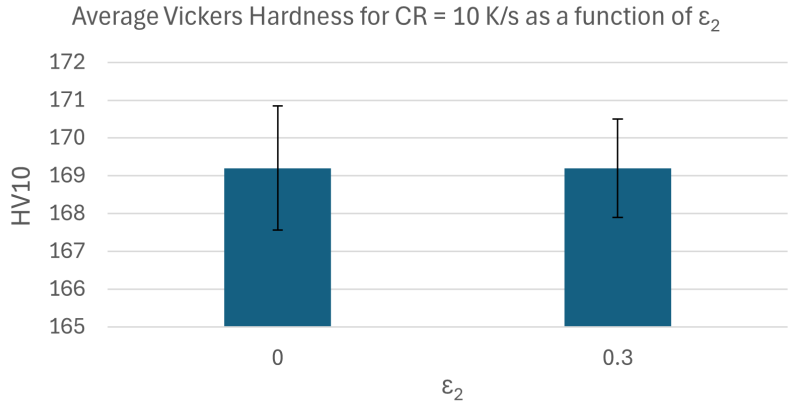

Figure 4.10: Average Vickers hardness (HV10) measured for samples processed at a cooling rate of 10 K/s as a function of the applied strain parameter ε_2. Error bars represent the standard deviation of five hardness measurements per condition.

The samples with CR = 10 K/s (Figure 4.10) show comparable average hardness values within experimental uncertainty. This means that deformation has no apparent influence on the hardness of the material. Even though polygonal ferrite was found in the sample with $\varepsilon_2 = 0.3$, acicular ferrite is still the dominating phase. The decrease in the average grain size for the sample with $\varepsilon_2 = 0.3$ is also insufficient to produce a corresponding increase in hardness, resulting in values comparable to those of the undeformed condition. Moreover, due to large error bars no distinctions can be made between both deformation levels.

The samples processed at CR = 50 K/s (Figure 4.11) with $\varepsilon_2 = 0.3$ exhibit a slight decrease in the hardness compared to the sample with $\varepsilon_2 = 0.0$. The phases present in the sample without deformation are bainite and martensite, whereas the sample with $\varepsilon_2 = 0.3$ does not contain martensite, therefore, yielding a lower hardness value. The sample with $\varepsilon_2 = 0.5$ shows a relatively large standard deviation, which may affect the reliability and interpretation of the results, so no conclusions can be drawn for the samples with this deformation level.

The samples processed at CR_{max} show a decreasing hardness with an increasing deformation (Figure 4.12). These samples experienced the largest variation in the phases formed influenced by deformation. Each one of the microstructural constituents formed have different structural compositions, morphology, and transformation mechanisms, therefore, different hardness values. With $\varepsilon_2 = 0.0$, martensite is observed, and the corresponding hardness matches reported values for a material with the same carbon content [61]. For the sample with $\varepsilon_2 = 0.3$ there is a slight decrease in hardness. This decrease in hardness is be attributed to the transition from a fully martensitic microstructure toward a mixture of

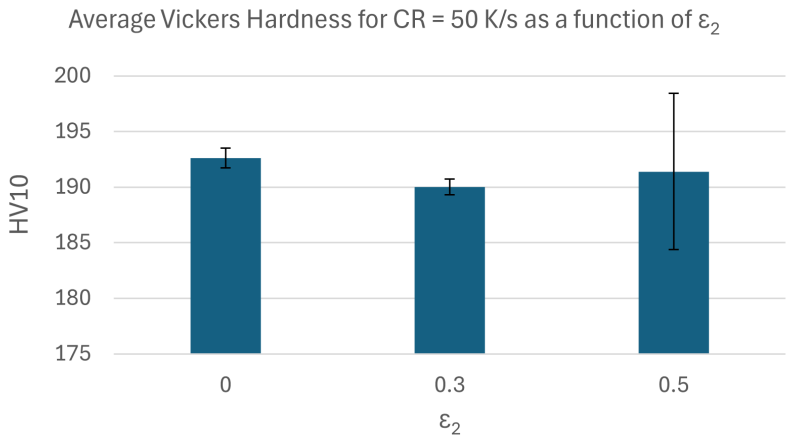

Figure 4.11: Average Vickers hardness (HV10) measured for samples processed at a cooling rate of 50 K/s as a function of the applied strain parameter ε_2. Error bars represent the standard deviation of five hardness measurements per condition.

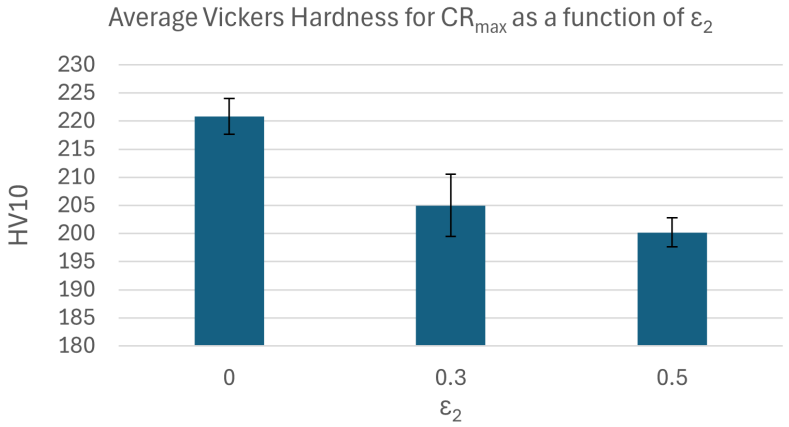

Figure 4.12: Average Vickers hardness (HV10) measured for samples processed at a cooling rate of CR_{max} as a function of the applied strain parameter ε_2. Error bars represent the standard deviation of five hardness measurements per condition.

bainite and martensite. Martensite is diffusionless, making carbon atoms trapped in interstitial sites, but bainite is a mix of displacive and diffusional, forming ferrite (a softer phase) and cementite. Hence, the presence of bainite decreases the overall hardness of the samples with $\varepsilon_2 = 0.3$. Applying a deformation of $\varepsilon_2 = 0.5$, shows a further decrease in the hardness, attributed to the resulting ferritic microstructure.

Combining the hardness results for all the cooling rates with all the deformation levels (Figure 4.13), an increase in the hardness of the material is seen for an increasing cooling rate. A faster the cooling rate, impedes dislocation motion and enhances the hardness of the material [56]. The samples with the lowest cooling rate, containing ferrite and pearlite, have the lowest measured hardness. This is due to its characteristic coarse structure and low carbon content (0.005wt.%) [6]. The original sample shows a hardness value comparable to that found for the sample with CR = 10 K/s and $\varepsilon_2 = 0.0$. This is also justified by their similar microstructures, both having irregular ferrite grains. In conclusion, the hardness of this material is governed by the nature of the microstructural constituents present in the material, while grain size refinement plays a secondary role.

4.6. Continuous Cooling Transformation Diagram

Before delving into the CCT results, another CCT plot was made to compare the Thermo-Calc CCT calculation with the experimental results obtained for the undeformed sample. To compute this plot, the first step was to manually convert the data estimated by Thermo-Calc from Figure 3.2 to Excel. The steps taken to do this are explained in Appendix C. Note that the composition used to plot the CCT

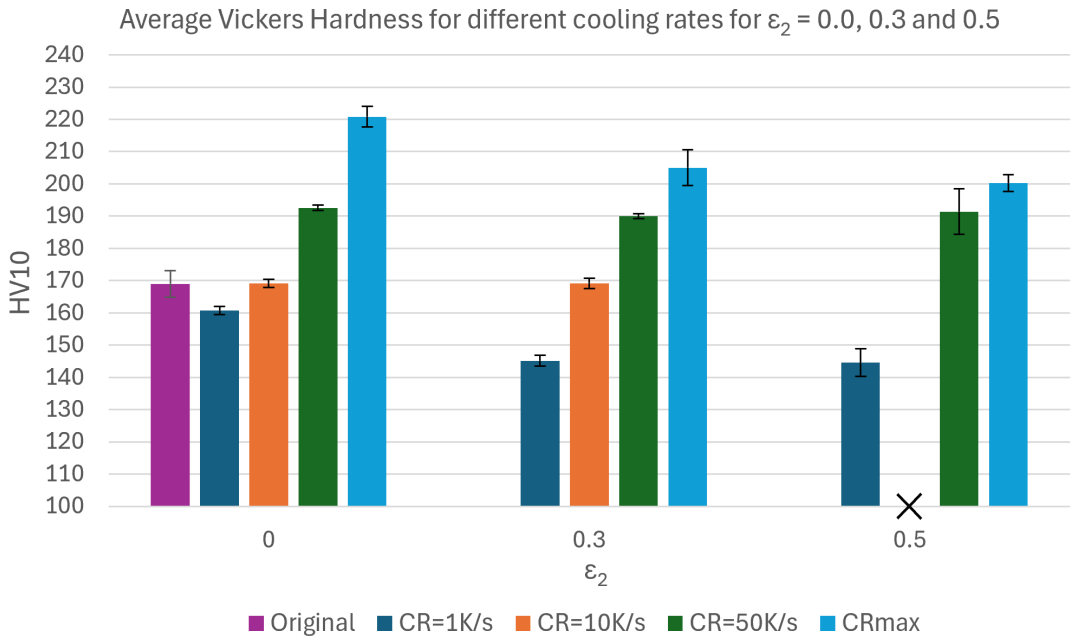

Figure 4.13: Average Vickers hardness (HV10) of samples processed at different cooling rates for ε_2 = 0.0, 0.3 and 0.5. The conditions include the original (as-received) material, and samples processed at cooling rates of 1, 10, and 50 K/s, and CR_{max}. Error bars represent the standard deviation calculated from five hardness measurements per condition.

using Thermo-Calc was a simplified composition of the material, namely 0.05 wt% C, 1.3 wt% Mn and 0.2 wt% Si, and an austenite grain size of 100 μm. This CCT plot can be found in Figure 4.14.

The first observation is that both approaches show good agreement for the ferrite curve for cooling rates of 1 and 10 K/s, exhibiting similar transformation behavior in the CCT diagram. However, at a cooling rate of 50 K/s, Thermo-Calc predicts ferrite to be formed at significantly shorter times and higher temperatures than observed experimentally, thereby overestimating the ferrite region. Conversely, bainite formation is overestimated by Thermo-Calc, as indicated by a higher predicted B_s temperature compared to the experimental results at CR = 50 K/s. The experimental pearlite curve (dashed blue curve) was drawn purely based on estimation, since only one data point at right-most cooling curve was measured (hence, labeled with a '?'). Comparing this data point to the calculation of Thermo-Calc at CR = 1 K/s, it can be seen that Thermo-Calc underestimates the pearlite curve. In summary, noticeable discrepancies are observed for bainite and pearlite.

When examining the M_s temperature line (yellow line), the experimental results show a higher M_s temperature than that predicted by Thermo-Calc. This discrepancy can be attributed to several factors. For instance, differences may arise from the method used to determine the M_s temperature from the dilatometer data; some approaches define M_s as the exact point where the curve deviates from linearity (as done in this work), while others define it at a 5 % deviation from the baseline. Furthermore, when comparing the experimental M_s temperature with the empirically determined value reported in Table 3.2 (average of 491 °C), the experimental result is closer to the empirical value than to the Thermo-Calc estimate. Another contributing factor may be the austenite grain size, which is experimentally unknown in this study. A value of 100 μm was assumed in the Thermo-Calc simulations; however, the actual grain size in the sample may differ.

Note that the experimentally derived data points do not lie exactly on the nominal CR lines. This is due to discrepancies between the nominal cooling rates specified in the dilatometer program and the actual cooling rates experienced by the samples.

To understand the influence of prior deformation (compression) on a Nb-microalloyed low-carbon steel (Figure 4.15), the microstructure characterization and transformation temperatures were combined and a CCT diagram was constructed. The data used for the plots can be found in Appendix C. Note that

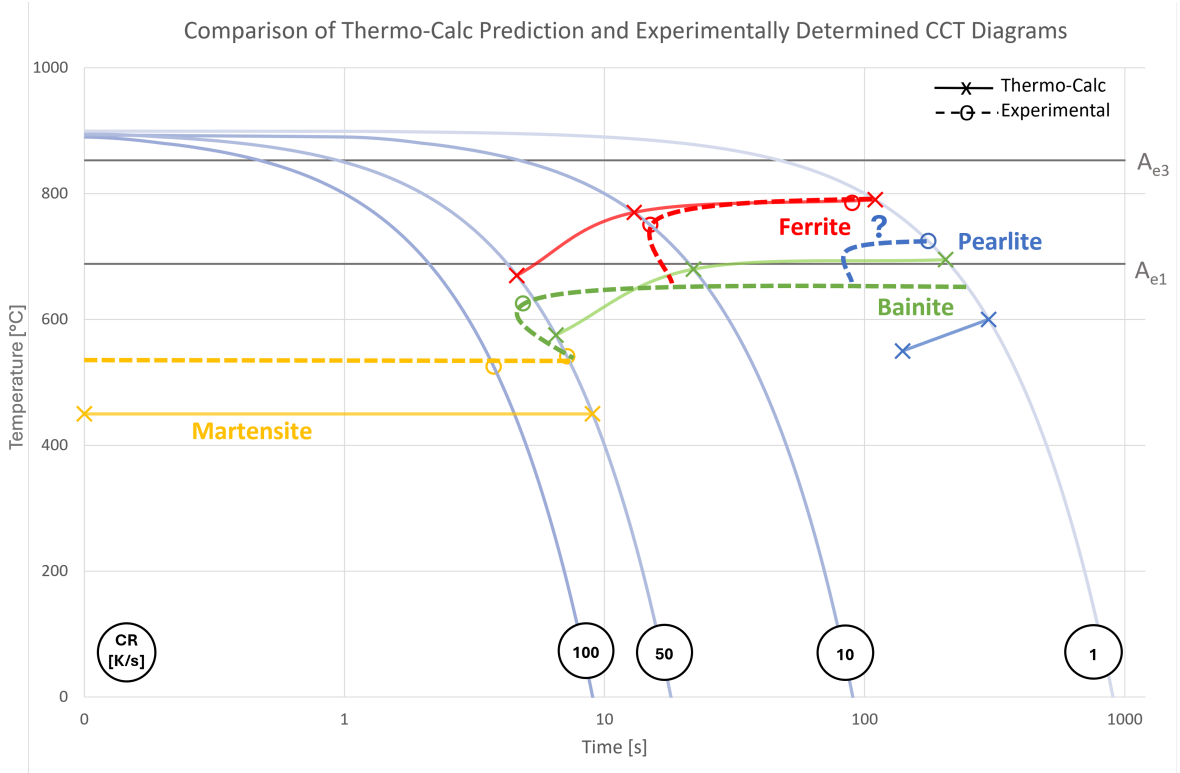

Figure 4.14: CCT plot comparing the Thermo-Calc prediction for a simplified composition (0.05C-1.3Mn-0.2Si in wt.%)), with the experimental results obtained for the sample without deformation ($\varepsilon_2 = 0.0$). Note: The experimental pearlite curve is labeled with '?' since it is based purely on estimation.

no martensite was found for any cooling rate for $\varepsilon_2 = 0.5$, this is why only two lines can be observed, instead of three. Also, for $\varepsilon_2 = 0.3$ only one data point was found for the M_s, so a horizontal line is drawn connected to the start the of the bainite curve for the corresponding deformation level. The pearlite curves drawn are estimated (hence, labeled with '?'), since only one data point was obtained per deformation level at the right-most cooling curve (CR = 1 K/s).

It is important to take into account that the curves shown in the plot have been drawn manually, as estimates. The general shape of the curves have been drawn based on what can be seen from literature (for example from Figure 2.6). Also note, no distinction was made between acicular and polygonal ferrite in the plot due to limited amount of data. The A_{e1} and A_{e3} values marked as gray horizontal lines are the values found for the austenite equilibrium temperatures using Thermo-Calc.

Analyzing the CCT diagram in Figure 4.15, the effect of prior deformation on ferrite transformation is evident. With deformation, the noses of the ferrite curves are shifted toward shorter transformation times and to higher transformation temperatures compared to the undeformed condition. This indicates a pronounced acceleration of ferrite formation due to deformation. Deformation in the austenite introduces a high density of dislocations which act as preferential nucleation sites and promote both nucleation and growth. This behavior arises from the increased stored energy associated with these defects, which lowers the nucleation energy barrier. This is consistent with previous studies [14] showing that ferrite (and pearlite) transformations occur earlier in plastically deformed austenite than in undeformed austenite, with the acceleration being most pronounced at the initial stage of transformation and increasing with strain level. The observed shift of the ferrite "nose" toward shorter times agrees with literature reports that deformation primarily affects the left-hand side of the CCT curve [49].

Interestingly, the ferrite curves show that the sample with $\varepsilon_2 = 0.3$ shows the highest transformation start temperature, whereas the curve corresponding to $\varepsilon_2 = 0.5$ lies between the undeformed condition and the $\varepsilon_2 = 0.3$ condition. A hypothesis for this behavior is possibly related to the non-linear evolution of stored energy with increasing strain. As discussed by Petkovicét al. [62], at intermediate deformation

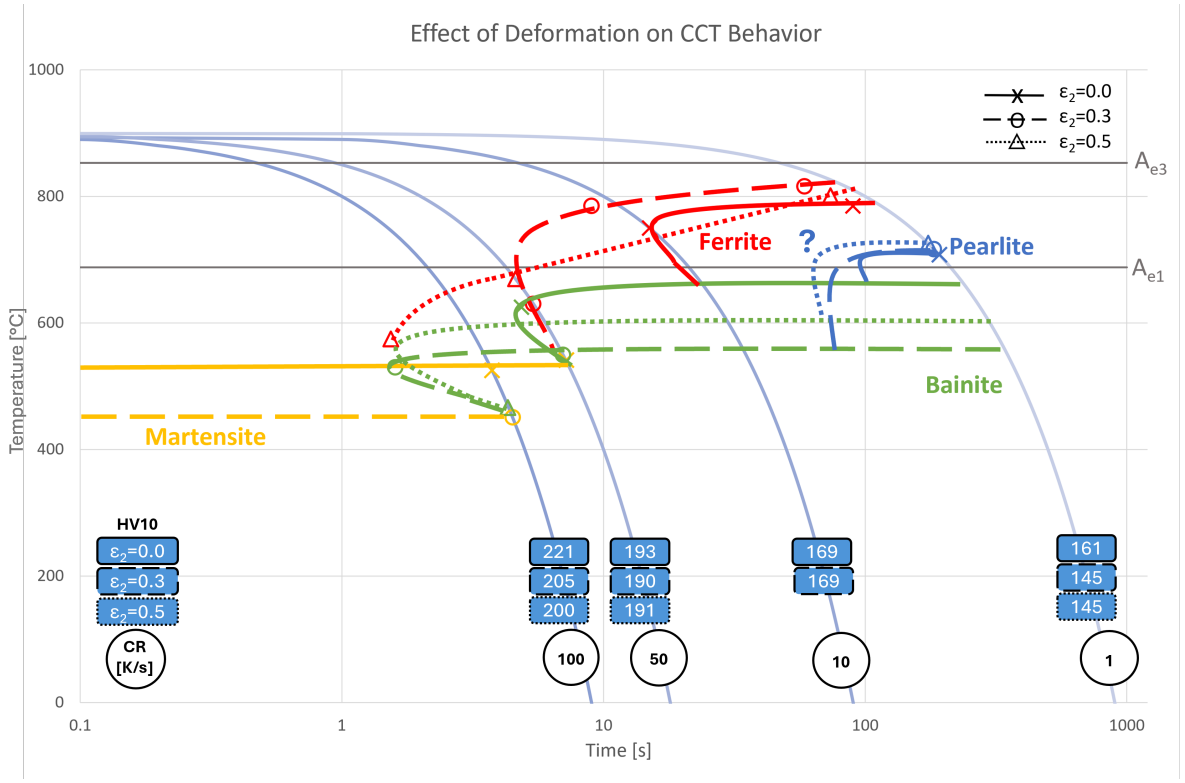

Figure 4.15: CCT plot investigating the effect of deformation (compression) on the material 0.05C-1.3Mn-0.042Nb-0.2Si-0.010Ti-0.03Al-0.0040N-Bal.Fe (wt.%) for tested cooling rates of 1, 10, 50 and 100 K/s. The hardness values (HV10) determined experimentally are also shown. Note: The pearlite curves are labeled with '?' since they are purely based on estimation.

levels the increased dislocation density enhances the driving force for transformation, while at higher strains recovery and the onset of dynamic recrystallization partially consume the stored energy through defect annihilation, thereby reducing the effective driving force for transformation [62]. This can therefore suggest that the stored energy for $\varepsilon_2 = 0.5$ is lower than that of $\varepsilon_2 = 0.3$.

For pearlite, no clear trend can be identified, as there is only one data point for each deformation level and their transformation start temperatures are similar, all on the cooling rate curve of 1 K/s. Due to the limited number of data points for this phase, the pearlite curves were constructed to intersect the corresponding bainite curves for the same ε_2. Due to these limitations, no definitive conclusions can be drawn regarding the effect of deformation on the pearlite transformation kinetics.

The influence of deformation on bainite transformation is more complex due to its mixed diffusion-displacive nature. Nevertheless, the noses of the bainite curves for $\varepsilon_2 = 0.3$ and 0.5 are shifted toward shorter times compared to the undeformed condition. This acceleration of bainite observed in the present work aligns with literature findings [14] that deformation generally promotes transformations involving a diffusion component, even when the transformation mechanism is not purely diffusive.

Another observation is that the bainite curves shift towards lower transformation temperatures when prior deformation is applied, whereas the opposite trend is observed for the ferrite curves. A similar behavior was reported by Kawulok et al. [14] when the material was cooled down at > 1.5 K/s (see Figure 2.6). This behavior may be attributed to its partially displacive nature, which may lead to a reduction in transformation temperatures, analogous to the downward shift of the martensite start temperature (explained below), which is associated with increased austenite stability resulting from deformation-induced grain refinement. Additionally, the bainite curves exhibit a similar non-linear trend to that observed for the ferrite curves; however, in this case the shift occurs toward lower temperatures. The less pronounced downward shift for $\varepsilon_2 = 0.5$ can be explained by the defect annihilation at a high deformation level. This leads to a reduction in the effective driving force (undercooling) compared to $\varepsilon_2 = 0.3$, leading to a less suppressed bainite curve for the $\varepsilon_2 = 0.5$ condition [62].

The CCT diagram shows a slight suppression of the martensitic transformation, manifested by a downward shift of the M_s temperature for the sample with $\varepsilon_2 = 0.3$. This reduction in M_s can be attributed primarily to refinement of the parent austenite grain (PAG) induced by plastic deformation. Grain refinement enhances austenite stability by strengthening the austenitic matrix and increasing the resistance to martensite-austenite interface motion, thereby requiring greater undercooling to initiate the martensitic transformation [13]. In addition, deformation-induced dislocation networks can impede interface propagation, further contributing to the observed suppression of martensitic transformation kinetics [14]. Overall, the results indicate that prior deformation stabilizes the austenite and slows the kinetics of martensitic transformation.

The constructed CCT diagram clearly demonstrates that prior deformation alters transformation kinetics of phase transformations. The transformation of ferrite is strongly accelerated, while the bainite transformation shows a moderate acceleration. With deformation in the austenite, the transformation start temperatures are increased for ferrite, but decreased for bainite and martensite. Therefore the effects of deformation in the austenite are therefore clearly reflected in the position of the experimentally derived CCT transformation curves. It was also found that for fast cooling rates, as was the case of 50 K/s and CR_{max}, increasing deformation in the austenite can change the dominating transformation product from martensite to bainite and further to ferrite.

4.7. EBSD & EDAX OIM Analysis

The EBSD results were analyzed using the software EDAX OIM Analysis 8. The grain boundaries, separated into HAGBs and LAGBs, were delineated in the IPF maps, to see the influence of deformation on the length and fraction of HAGBs and LAGBs, as well as on the total grain boundary (GB) length. In this work, LAGBs are grain boundaries with misorientations in the range $2 - 15°$, whereas HAGBs have misorientations between 15° and 62.8°. The misorientation of grains is used to describe the relative rotation between two crystal lattices [45]. The grain size distributions for all the samples were also generated to compare the results with the M.L.I. method.

4.7.1. Grain Boundary Length and Fraction

The grain boundary (GB) length is a valuable indication on the effective grain size of the samples [8]. Grain refinement causes an increase in the GB area, which impedes dislocation motion. To discuss the results, the GB length are plotted as a function of deformation for all the cooling rates, and the LAGBs and HAGBs fraction and lengths are also presented as a function of deformation. While the GB data obtained from 100 and 10 μm scale IPF maps show consistent trends with cooling rate and strain, the higher spatial resolution of the 10 μm scale images enables the detection of sub-grain boundaries. Therefore, the data used for the GB analysis comes from the images with the highest magnification.

As shown in Figure 4.16, the undeformed sample with CR = 1 K/s exhibits a fine-grained ferritic microstructure with a dense HAGB network. This network is due to the Nb-microalloy, as was also seen by Dere et al. [63]. With increasing deformation, the microstructure evolves toward a more organized substructure, with reduced internal misorientation, observed as an increase in the LAGBs. This agrees with the findings of Landheer et al. [64], who reported that prior deformation increases LAGB density, which provides energetically favorable, semi-coherent nucleation sites for ferrite.

The IPF maps for the samples with CR = 10 K/s (Figure 4.17), the sample with $\varepsilon_2 = 0.3$ reveals a more fragmented microstructure than the sample without deformation. This suggests that deformation promotes intragranular ferrite nucleation [22].

For the samples cooled at 50 K/s (Figure 4.18), the undeformed condition exhibits a microstructure rich in LAGBs and substructure, corresponding to a mixed bainitic-martensitic microstructure. This is because both phases form lath-like microstructures that retain significant transformation-induced dislocation substructure and low-angle misorientations [65]. For $\varepsilon_2 = 0.3$, the microstructure is bainite-ferrite with larger grains and more homogeneous internal orientations. Further deformation shifts the microstructure to ferrite.

A similar trend is observed for samples cooled at CR_{max} (Figure 4.19), where deformation strongly alters the microstructure from predominantly martensitic in the undeformed condition to ferrite for $\varepsilon_2 = 0.5$.

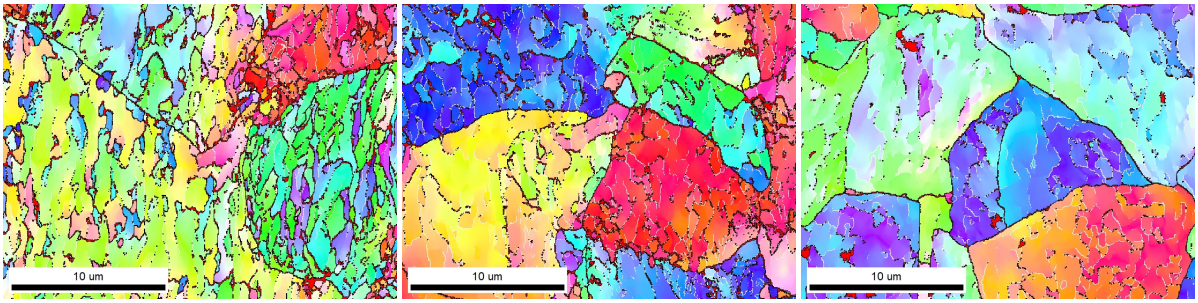

(a) $\varepsilon_2 = 0.0$ **(b)** $\varepsilon_2 = 0.3$ **(c)** $\varepsilon_2 = 0.5$

Figure 4.16: IPF maps for samples cooled at 1 K/s, showing the distribution of LAGBs (white) and HAGBs (black) for different values of ε_2.

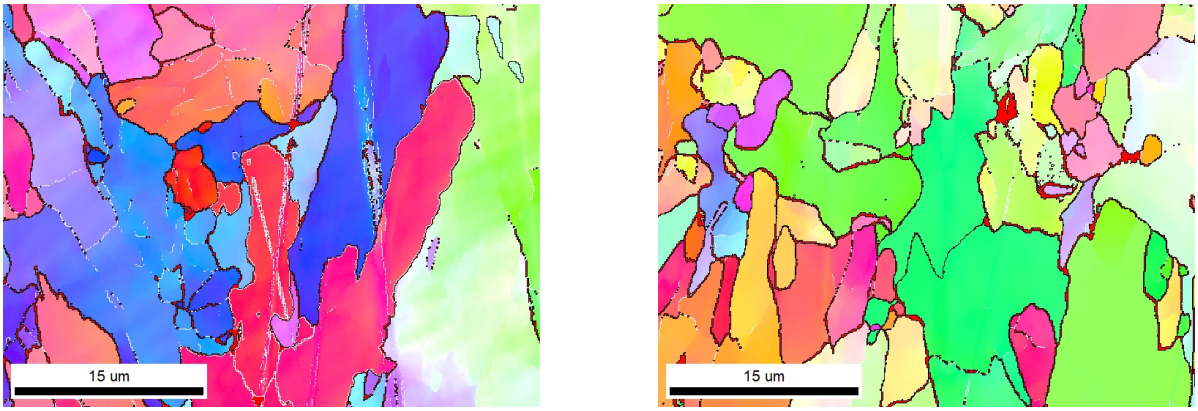

(a) $\varepsilon_2 = 0.0$ **(b)** $\varepsilon_2 = 0.3$

Figure 4.17: IPF boundary maps for samples cooled at 10 K/s, showing the distribution of LAGBs (white) and HAGBs (black) for different values of ε_2.

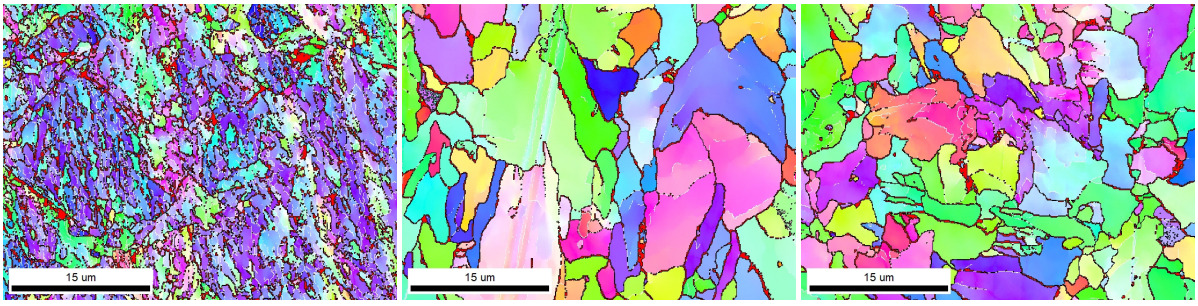

(a) $\varepsilon_2 = 0.0$ **(b)** $\varepsilon_2 = 0.3$ **(c)** $\varepsilon_2 = 0.5$

Figure 4.18: IPF boundary maps for samples cooled at 50 K/s, showing the distribution of LAGBs (white) and HAGBs (black) for different values of ε_2.

To quantitatively evaluate the effect of prior deformation on the GB length of the transformed phases, the results are presented in Figure 4.20. The plot shows that increasing deformation lead to a decrease in the total GB length, except the samples with CR = 10 K/s. This was unexpected, since due to a decrease in the grain size with an increasing deformation, the total GB length was predicted to increase. However, the grain size was measured using optical microscopy. With this technique, LAGBs cannot be resolved, nor the substructure caused by the Nb microalloying. This explains the mismatch between the grain size and grain boundary length. It should be noted that the IPF maps are shown at different length scales; this was accounted for during the normalization, although visual comparison alone may be misleading.

Only two samples were tested for CR = 10 K/s, with $\varepsilon_2 = 0.0$ and 0.3, and no noticeable dependence is

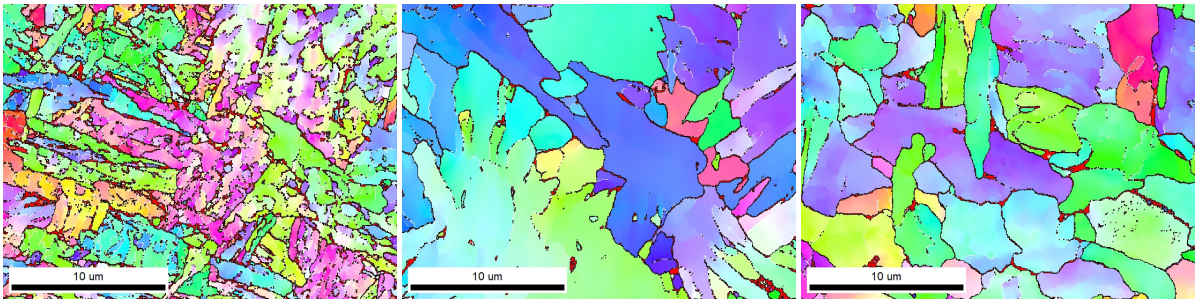

(a) $\varepsilon_2 = 0.0$ **(b)** $\varepsilon_2 = 0.3$ **(c)** $\varepsilon_2 = 0.5$

Figure 4.19: IPF boundary maps for samples cooled at CR_{max}, showing the distribution of LAGBs (white) and HAGBs (black) for different values of ε_2.

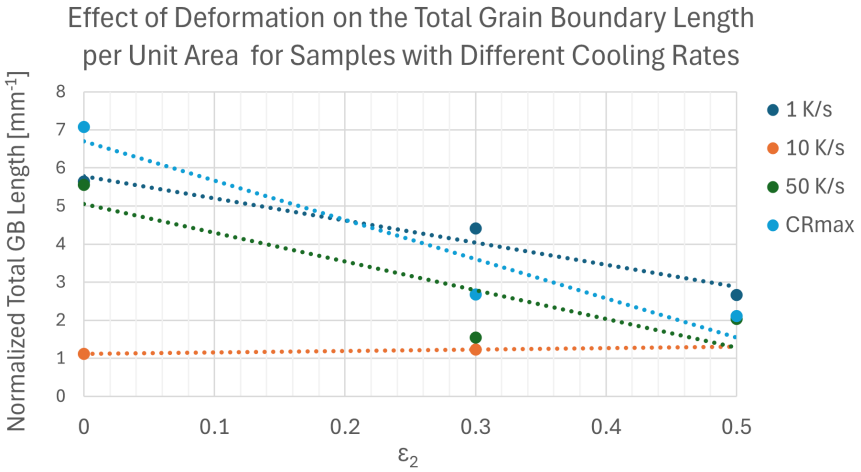

Figure 4.20: Plot showing the normalized total GB length (GB length per unit analyzed area) as a function of the applied strain ε_2, with separate curves corresponding to different cooling rates. The data used is taken from the images with the highest magnification. The GB lengths were obtained from software-based image analysis; only one value per sample is available, so no standard deviation is shown.

observed for the GB length with increasing deformation. This can again be explained by the similarity of their microstructures, both in morphology and grain size. They measure the lowest normalized GB length as their microstructures appear to be large grains with no substructure (as was seen in Figure 4.17).

The undeformed sample with CR_{max} has the highest normalized GB length, which can be attributed to the high boundary density characteristic of a lath martensitic microstructure. Also, for high cooling rates (50 K/s and CR_{max} K/s), the normalized GB lengths of the samples with $\varepsilon_2 = 0.5$ are very similar. This is because the microstructures obtained were very similar, as was seen in the OM images, elongated and polygonal ferrite grains. This similarity can also be reasoned as despite the difference in their nominal cooling rates, the effective cooling rates were alike, where for the range 500–100 °C, the sample with CR_{max} had an effective CR = 54 K/s (refer to Table 3.5).

To further analyze the GB data, the results have been separated into normalized LAGB and HAGB length (Figure 4.21), as well as LAGB and HAGB fraction (Figure 4.22) plots. The findings are summarized below:

- For the samples cooled at 1 K/s, the normalized LAGB length does not vary with deformation. However, the normalized HAGB length decreases with increasing deformation. This is therefore expressed as an increase in the LAGB fraction and decrease in the HAGB fraction. This is associated with the dense HAGB network resulting from Nb microalloying [63], whereas deformation primarily leads to an increase in LAGB density rather than HAGB density, as seen in Figure 4.16.

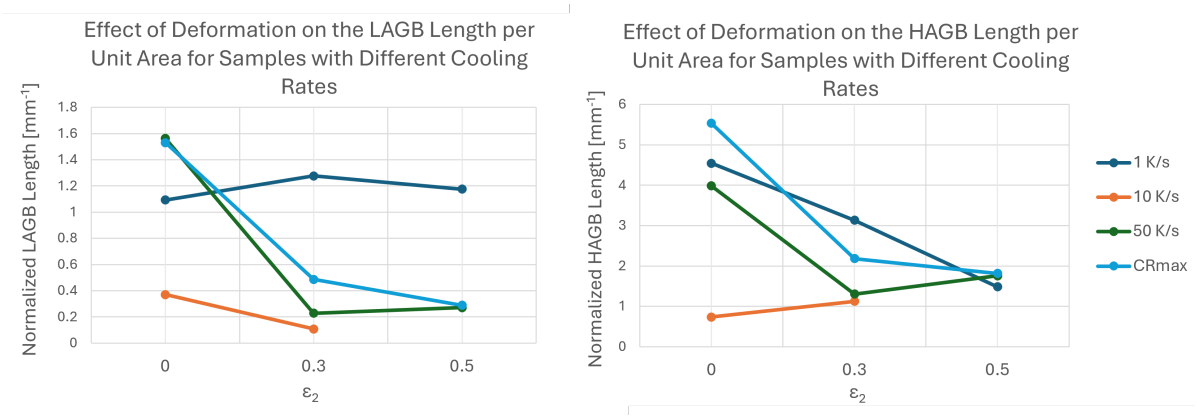

Figure 4.21: The LAGB (left) and HAGB (right) length per unit analyzed area are plotted as a function of the applied strain ε_2, with separate curves corresponding to different cooling rates. HAGB and LAGB length are reported as a single value per sample; standard deviation is not available.

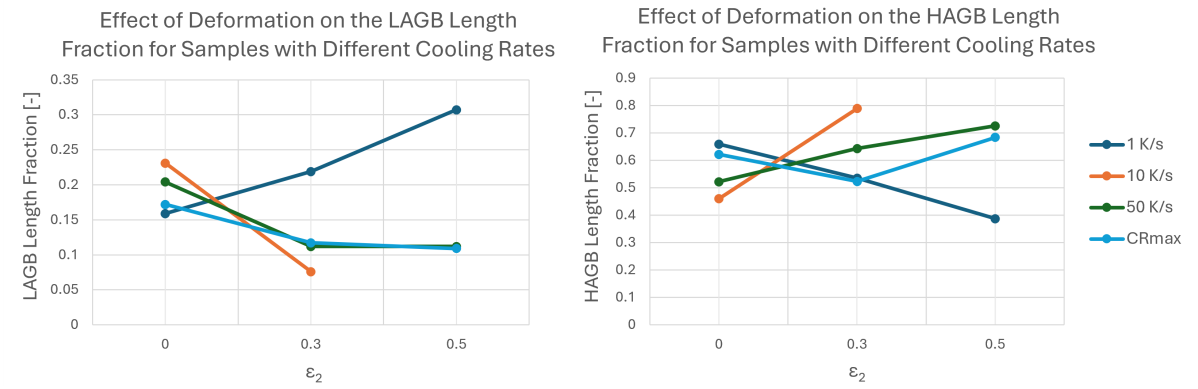

Figure 4.22: The LAGB (left) and HAGB (right) length fractions are plotted as a function of the applied strain ε_2, with separate curves corresponding to different cooling rates. HAGB and LAGB fractions are reported as a single value per sample; standard deviation is not available.

- For CR = 10 K/s, the normalized LAGB length decreases slightly and the normalized HAGB length increases slightly when deformation is applied. However, due to the limited number of samples and the similarity of the resulting microstructures, no definitive conclusions can be drawn.
- For high cooling rates (50 and CRmax K/s), the samples with $\varepsilon_2 = 0.0$ and 0.3 show a considerable decrease in both normalized LAGB and HAGB lengths. In the case of CRmax, this reduction is attributed to the transition from a fully martensitic microstructure to a mixed bainite–martensite microstructure. At CR = 50 K/s, it corresponds to the transition from a bainite–martensite to a bainite–ferrite microstructure. This trend is consistent with martensite having the highest overall grain boundary length, owing to its fine lath-like morphology and associated high boundary density.
- For the samples with $\varepsilon_2 = 0.5$ at CR = 50 K/s, both the normalized LAGB and HAGB lengths show a slight increase, reflected in the measured boundary fractions. This is further supported by the IPF maps, which reveal a finer ferritic microstructure compared to the bainite–ferrite microstructure.
- However, at CR_{max} K/s, both the normalized LAGB and HAGB lengths for $\varepsilon_2 = 0.5$ decrease slightly, which is consistent with the IPF maps showing minimal variation in grain boundary density.

Overall, deformation modifies the GB character distribution in a cooling-rate-dependent manner. At low cooling rates (1 K/s), deformation primarily increases the LAGB formation, whereas at intermediate cooling rates (10 K/s) no clear dependence was found. For high cooling rates (50 and CR_{max} K/s),

deformation shifted the CCT curves, so the GB behavior changed based on the new phase, or phases, present.

4.7.2. Grain Size Distribution

To compare the grain size results obtained from the M.L.I. method, the grain size distributions of the samples were computed using the EDAX OIM Analysis software. The program presented the diameters of the grains and the number fraction in a plot and a table, as well as a summary with the calculated average grain size based on the number and area method, and their respective standard deviations.

Interestingly, analyzing the results, all the samples showed that most of the grains were smaller than 1 μm, and the average grain size was in the range of 0.1-1.2 μm for all the samples (using the number method). This did not correlate with what was observed from the IPF maps or OM images, nor with the results from the M.L.I. method (Figure 4.7). This was due to an inaccurate clean-up of the samples which incorrectly indexed these points as small grains. To fix this issue, the grain sizes were computed again, but this time with the constraint that the minimum grain size was 1 μm. Using this specification, many samples appeared with more than 90% of the pixels being highlighted from the grain image. An example is shown in Figure 4.23. In this figure, selecting the grains larger than 1 μm showed that 93.5% of the image was selected. This seems reasonable, and the remaining ~6 % likely corresponding to unindexed pixels.

After collecting the grain size averages with the size constraint, no conclusive results were found for any cooling rate. Both images were analyzed, with x500 and x3000 magnification, and their results were also not consistent. From a statistical standpoint, the ×500 magnification images were selected for the grain size analysis, as they provide a larger sampled area and therefore yield more representative and reliable grain size statistics. However, no trend was observed for an increasing deformation for any of the cooling rates. For the number method grain size calculation, the average grain size lies between 1 to 4 μm for all the samples. For the area method, since larger grains weigh more, the average grain size calculated was larger for all the samples, ranging from ~ 4 to 20 μm. Only the samples with CR = 10 K/s showed a decreasing grain size for an increasing deformation for both methods (number and area), however, with this cooling rate only two deformation levels were tested (ε_2 = 0.0 and 0.3), compared to the rest of the cooling rates, which have three. Due to these reasons, the reliability fo the software for determining the grain size remains questionable.

To explain this issue further, the three methods used to calculate the average grain size of the samples with a cooling rate of 10 K/s have been collected in Table 4.2. The three methods yield markedly different average grain sizes. Both the number and area method show large standard deviations relative to their mean values, indicating poor reliability. The number method strongly underestimates the grain size due to incorrectly identifying GBs as small grains, while the area method overestimates the grain size due to its calculation method. This shows that neither of the automated methods provides a representative grain size for the samples in the present study.

CR [K/s]	ε_2	M.L.I. Method [μm]	Number Method [μm]	Area Method [μm]
10	0.0	14.81 ± 4.47	4.74 ± 5.76	19.58 ± 10.76
10	0.3	9.44 ± 1.57	4.43 ± 3.76	10.52 ± 4.79

Table 4.2: Table comparing the results obtained using different methods for the average grain size of the samples with CR = 10 K/s and varying deformation. The SDs are also included. The M.L.I. method has been done manually, whereas the number and area method have been computed by the EDAX OIM Software, using the image with a x500 magnification.

Other issues observed with the grain size calculation is that the software was counting the GBs as grains when the GBs were thick lines. Also, when the sample had a lot of sub-grain structure it was partly eliminated during the clean-up. Examples of these two issues can be found in Figure 4.24.

Based on the grain size results obtained from the software, and in comparison with both the manually measured M.L.I. method and the visual assessment of the OM and IPF maps, it can be concluded that the automated grain size results are not consistent with either the M.L.I. data or the observed microstructural features. This is mainly due to difficulties in identifying sub-grain structure or incomplete clean-up of the samples. Therefore, no further analysis of the grain sizes using the software will be conducted.

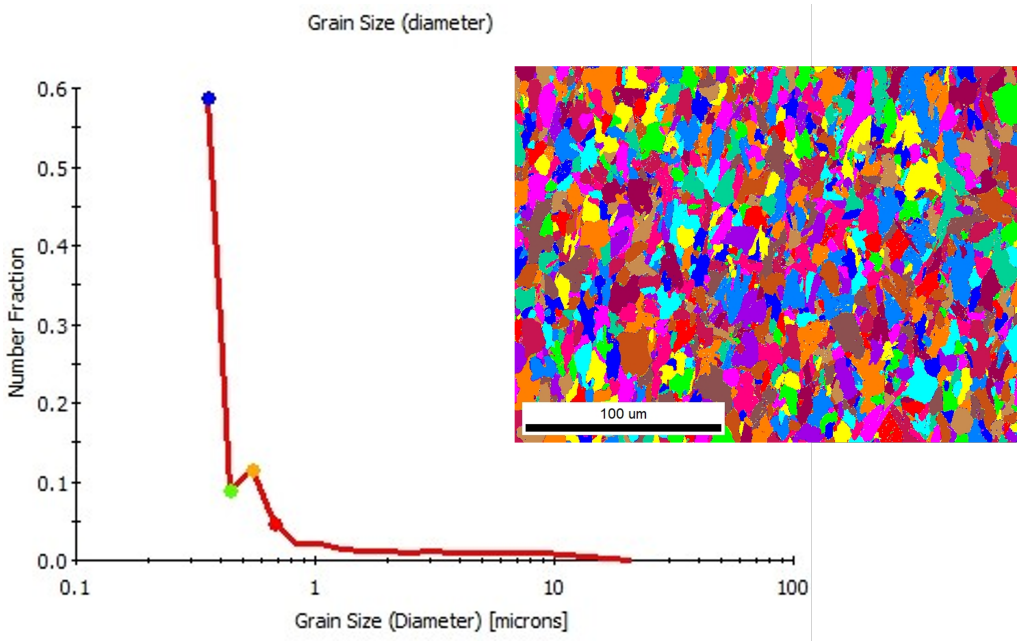

(a)

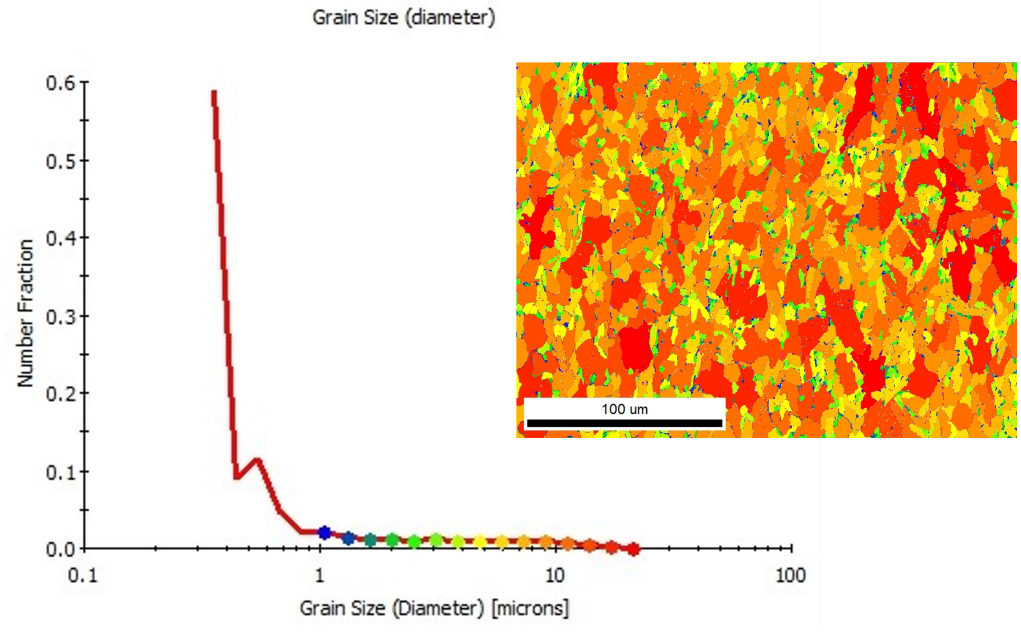

(b)

Figure 4.23: Grain maps and corresponding grain size distributions obtained using EDAX OIM Analysis, highlighting grains (indicated by colored markers in the distributions) (a) smaller than 1 μm and (b) larger than 1 μm. This sample was deformed with $\varepsilon_2 = 0.3$ and cooled at 10 K/s.

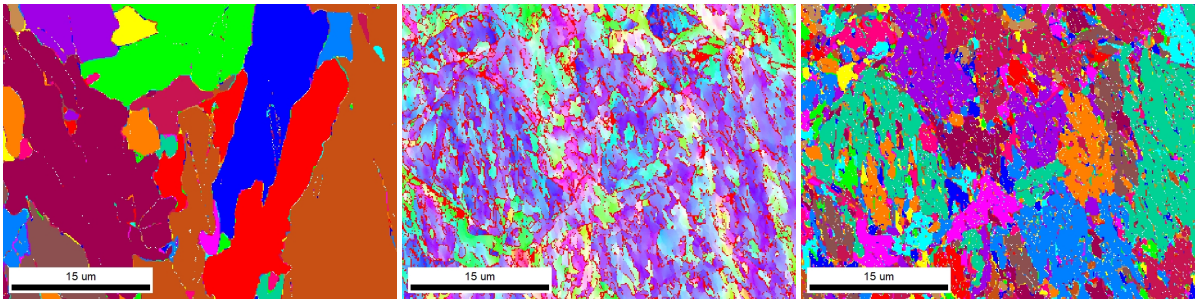

(a) Grain image. **(b)** IPF X image. **(c)** Grain image.

Figure 4.24: (a) Sample with $\varepsilon_2 = 0.0$ and CR = 10 K/s, showing how the software identified GBs as grains. Images (b) and (c) show an example of the loss of sub-grain structure when the sample is processed with the EDAX OIM Analysis software (sample with $\varepsilon_2 = 0.0$ and CR = 50 K/s).

5

Conclusion

The present study investigates the influence of deformation on the CCT behavior of a Nb-microalloyed low-carbon steel with composition 0.05C-1.3Mn-0.042Nb-0.2Si-0.010Ti-0.03Al-0.0040N-Bal. Fe, in wt.%, provided by TATA Steel. The experimental methods used include dilatometry, OM, and Vickers hardness testing for the CCT diagram construction. Further analysis was done using the M.L.I. method, EBSD and EDAX OIM software analysis for GB characterization and grain size analysis. The main conclusions are summarized below.

For samples cooled at CR = 1 K/s, the microstructure consists predominantly of ferrite with coarse, equiaxed grains. With increasing deformation, the average grain size decreases and the pearlite fraction appears to be reduced. Increasing the cooling rate to 10 K/s leads to a more irregular ferritic morphology, identified as acicular ferrite. With increasing deformation, grain refinement is again observed; however, the microstructure is still acicular ferrite with some equiaxed ferrite grains. For CR = 50 K/s, the microstructure with $\varepsilon_2 = 0.0$ consists on a combination of bainite and martensite, with $\varepsilon_2 = 0.3$ the microstructure shifts toward bainite-ferrite and to ferrite with $\varepsilon_2 = 0.5$. For CR_{max}, the undeformed microstructure is fully martensitic, with $\varepsilon_2 = 0.3$ the microstructure shifts toward a mixture of martensite and bainite, and to ferrite with $\varepsilon_2 = 0.5$. For CR = 50 K/s and CR_{max} at $\varepsilon_2 = 0.5$, very similar microstructures are observed, consisting of a mixture of polygonal and elongated ferrite. Overall, there is an increase in both T_s and T_f temperatures with increasing deformation, except for the samples processed at CR_{max}.

The grain size analysis using the M.L.I. method shows that increasing deformation in the austenite leads to a decrease in the grain size after the transformation. Additionally, increasing the cooling rate leads to a decrease in the average grain size. The coefficient of variation (%SD) was also evaluated and was found to decrease with increasing deformation, which means that the microstructure transformed was more uniform.

For the hardness measurements, for CR = 1 K/s, applying deformation lead to a decrease in hardness, attributed to the decrease in the pearlite fraction with increasing deformation. For samples cooled at 10 K/s, deformation has no apparent effect on hardness due to very similar microstructures. For higher cooling rates, increasing deformation leads to a reduction in hardness, which can be attributed to changes in the transformed microstructure, with a shift from martensitic to bainitic and ultimately ferritic constituents. Therefore, the hardness values for high cooling rates (> 50 K/s) are strongly influenced by the nature and properties of the microstructural constituents present.

The CCT diagram comparing the experimental results for the undeformed samples against the Thermo-Calc predictions showed discrepancies. Especially for the pearlite curve and the martensite line. To understand the influence of deformation on the material, a CCT diagram showing the experimental results for all three deformation levels of all cooling rates was plotted. Deformation in the austenite was found to significantly influence the microstructural evolution of the transformed products. Compared to the undeformed condition, deformation shifted ferrite start and finish curves to shorter times and higher temperatures. For pearlite, the trend is less clear due to very similar transformation start temperatures

for ε_2 = 0.0, 0.3 and 0.5. The bainite transformation curves were also shifted toward shorter times but lower transformation temperatures with increasing deformation. In contrast, the martensitic line was suppressed for ε_2 = 0.3. Overall, deformation in the austenite shifts ferrite and bainite to shorter times and shifts martensite to lower transformation temperatures.

Grain boundary analysis using EDAX OIM Analysis software shows that increasing deformation in the austenite leads to a decrease in total grain boundary length after transformation, except for samples cooled at CR = 10 K/s, where no clear dependence on deformation is observed. Deformation was shown to influence the grain boundary character distribution in a cooling-rate-dependent manner. At low cooling rates (1 K/s), deformation in the austenite phase promotes LAGB formation in the ferrite, leading to an increased fraction of LAGBs. At high cooling rates (50 and CR_{max} K/s), deformation altered the phases formed due to shifts in the CCT curves, resulting in changes in grain boundary character. From a martensite-bainitic microstructure without deformation to a ferritic microstructure for high levels of deformation.

6

Recommendations

After completing this thesis and reflecting on the project, several additional steps are identified that could have deepened the understanding of the investigated phenomena or could be pursued as future work by follow-up studies.

To improve the reliability of the transformation temperatures determination, a larger number of samples should be tested, with other cooling rates as well. Repeated measurements would reduce uncertainty and improve reproducibility. In addition, care should be taken to minimize HF-related signal disturbances by ensuring proper thermocouple installation.

Additional insight could be obtained by performing the same thermo-mechanical cycle tests on a GLEEBLE 3800 system to determine the stress-strain response of samples subjected to a total deformation of $\varepsilon_2 = 0.5$. This would enable identification of the onset of static softening and recovery processes, which may help explain the softening behavior observed at high deformation levels for the bainite and ferrite curves in the CCT diagram [62].

Based on the constructed CCT diagrams, it would also be beneficial to further distinguish the different transformation morphologies within the diagram. Separating regions corresponding to polygonal ferrite, acicular ferrite, bainite and martensite would make the results more specific and informative. Achieving this would require additional experimental data to clearly define the transformation domains associated with each morphology. Further characterization of the slow-cooled samples could be performed using Scanning Electron Microscopy (SEM) analysis to better understand its transformation mechanism with deformation.

Alternative TMP routes could also be explored. For instance, the use of a dilatometer equipped with nitrogen gas quenching could enable higher and more controlled cooling rates, providing additional data points for the martensitic transformation region of the CCT diagram. In the present study, such experiments could not be performed due to equipment limitations. The GLEEBLE 3800 was also tested for quenching, but the average cooling rate found was comparable to those measured for CR_{max} in the dilatometer, due to the heat dissipation from the large sample holders to the small cylindrical specimens resulted in cooling rates. Therefore, alternative set-ups could also be investigated.

In industrial TMP routes, other deformation modes are commonly encountered, for instance tension, shear, and bending. Investigating how these deformation modes influence phase transformation kinetics would be of interest. For example, during three-point bending, tensile stresses develop near the outer radius of the specimen, while compressive stresses occur near the inner radius [66]. Sectioning such a specimen could allow direct comparison between regions subjected to tension and compression, as well as the transition zone between them. Applying different cooling rates after bending may lead to the formation of distinct microstructures within a single sample.

References

[1] W. S. Association. *Circular Economy*. n.d. URL: https://worldsteel.org/wider-sustainability/circular-economy/ (visited on 04/28/2025).

[2] R. Singh. "Classification of Steels". In: *Applied Welding Engineering*. 3rd. Butterworth-Heinemann, 2020. Chap. 6, pp. 53–60. DOI: 10.1016/B978-0-12-821348-3.00014-8.

[3] W. Huang, J. Tian, J. Xiao, Q. Yuan, H. Hu, Q. Zhang, X. Gan, and G. Xu. "A quantitative analysis of transformation, microstructure and properties of a low-carbon Nb-microalloyed steel for building after deformation". In: *Journal of Materials Research and Technology* 41 (2026), pp. 4216–4230. DOI: 10.1016/j.jmrt.2026.02.019.

[4] R. Jamaati, S. Ataya, N. H. Alrasheedi, and A. Fathy. "Effect of carbon content on the martensite morphology, texture, and mechanical properties of dual-phase steels". In: *Journal of Materials Research and Technology* 39 (Nov. 2025), pp. 9477–9488. DOI: 10.1016/J.JMRT.2025.11.256.

[5] H. Bhadeshia and R. Honeycombe. "Iron-Carbon Equilibrium and Plain Carbon Steels". In: *Steels*. 5th. Butterworth-Heinemann, Jan. 2024. Chap. 3, pp. 59–100. DOI: 10.1016/B978-0-08-100270-4.00003-2.

[6] S. Papavinasam. "Materials". In: *Corrosion Control in the Oil and Gas Industry*. Boston: Gulf Professional Publishing, 2014. Chap. 3, pp. 133–177. DOI: 10.1016/B978-0-12-397022-0.00003-0.

[7] R. Bharadwaj, A. Sarkar, and B. Rakshe. "Effect of Cooling Rate on Phase Transformation Kinetics and Microstructure of Nb–Ti Microalloyed Low Carbon HSLA Steel". In: *Metallography, Microstructure, and Analysis* 11.4 (Aug. 2022), pp. 661–672. DOI: 10.1007/S13632-022-00864-9.

[8] S. Zajac, V. Schwinn, and K.-h. Tacke. *Characterisation and Quantification of Complex Bainitic Microstructures in High and Ultra-High Strength Linepipe Steels*. Tech. rep. MSF, Nov. 2005, pp. 387–394. DOI: 10.4028/www.scientific.net/msf.500-501.387.

[9] H. Bhadeshia and R. Honeycombe. "Formation of Martensite". In: *Steels*. 5th. Oxford: Butterworth-Heinemann, 2024. Chap. 5, pp. 137–176. DOI: 10.1016/B978-0-44-318491-8.00011-3.

[10] D. David, R. Schneider, G. Klösch, and C. Sommitsch. "Influence of Alloying Elements on the Transformation Behavior of Medium Manganese Steels". In: *NETSU SHORI* 64 (2024), pp. 187–192. ISSN: 0288-0490. DOI: 10.14940/netsushori.64.ex187.

[11] M. C. Zhao, K. Yang, F. R. Xiao, and Y. Y. Shan. "Continuous cooling transformation of undeformed and deformed low carbon pipeline steels". In: *Materials Science and Engineering: A* 355.1-2 (Aug. 2003), pp. 126–136. DOI: 10.1016/S0921-5093(03)00074-1.

[12] I. Dey, S. Chandra, R. Saha, and S. K. Ghosh. "Effect of Nb micro-alloying on microstructure and properties of thermo-mechanically processed high carbon pearlitic steel". In: *Materials Characterization* 140 (June 2018), pp. 45–54. DOI: 10.1016/J.MATCHAR.2018.03.038.

[13] C. Celada-Casero, J. Sietsma, and M. J. Santofimia. "The role of the austenite grain size in the martensitic transformation in low carbon steels". In: *Materials & Design* 167 (Apr. 2019), p. 107625. DOI: 10.1016/J.MATDES.2019.107625.

[14] R. Kawulok, P. Kawulok, I. Schindler, P. Opěla, S. Rusz, V. Ševčák, and Z. Solowski. "Study of the effect of deformation on transformation diagrams of two low-alloy manganese-chromium steels". In: *Archives of Metallurgy and Materials* 63.4 (2018), pp. 1735–1741. DOI: 10.24425/AMM.2018.125099.

[15] W. B. Hutchinson, L. Ryde, and P. S. Bate. "Transformation Textures in Steels". In: *Materials Science Forum* 495-497 (Sept. 2005), pp. 1141–1150. DOI: 10.4028/www.scientific.net/msf.495-497.1141.

[16] H. K. D. H. Bhadeshia. "Diffusional and displacive transformations". In: *Scripta Metallurgica* 21.8 (1987), pp. 1017–1022. DOI: 10.1016/0036-9748(87)90242-0.

[17] A. Jain and A. Varshney. "A critical review on deformation-induced transformation kinetics of austenitic stainless steels". In: *Materials Science and Technology* 40.2 (Feb. 2024), pp. 75–106. DOI: 10.1177/02670836231212618.

[18] T. Garcin, S. Rivoirard, C. Elgoyhen, and E. Beaugnon. "Experimental evidence and thermodynamics analysis of high magnetic field effects on the austenite to ferrite transformation temperature in Fe-C-Mn alloys". In: *Acta Materialia* 58.6 (Apr. 2010), pp. 2026–2032. DOI: 10.1016/J.ACTAMAT.2009.11.045.

[19] S. E. Offerman. "Evolving microstructures in carbon steel: a neutron and synchrotron radiation study". PhD thesis. 2003, p. 141. ISBN: 9040724261.

[20] C. Zener. "Theory of Growth of Spherical Precipitates from Solid Solution". In: *Journal of Applied Physics* 20.10 (Oct. 1949), pp. 950–953. ISSN: 0021-8979. DOI: 10.1063/1.1698258.

[21] H. Bhadeshia and R. Honeycombe. "Solutes that Substitute for Iron". In: *Steels: Microstructure and Properties*. Elsevier, 2017, pp. 101–134. DOI: 10.1016/b978-0-08-100270-4.00004-4.

[22] Z. Tong, C. Xia, W. Li, W. Ding, B. Guo, N. Min, W. Gong, S. Harjo, and N. Tsuji. "Unveiling post-deformation transformation mechanism and ferrite microstructure evolution for tailoring mechanical properties of low-carbon martensitic steels". In: *Journal of Materials Science & Technology* 266 (Sept. 2026), pp. 127–140. DOI: 10.1016/J.JMST.2025.12.004.

[23] X. Liu, F. Yuan, and Y. Wei. "Grain size effect on the hardness of nanocrystal measured by the nanosize indenter". In: *Applied Surface Science* 279 (2013), pp. 159–166. ISSN: 0169-4332. DOI: 10.1016/j.apsusc.2013.04.062.

[24] Y. N. Tsvetkov and Y. K. Loparev. "Influence of grain size on the hardness of metal". In: *AIP Conference Proceedings* 3021.1 (Mar. 2024), p. 30033. DOI: 10.1063/5.0193769/3280041.

[25] P. Wan, T. Kang, F. Li, P. Gao, L. Zhang, and Z. Zhao. "Dynamic recrystallization behavior and microstructure evolution of low-density high-strength Fe–Mn–Al–C steel". In: *Journal of Materials Research and Technology* 15 (Nov. 2021), pp. 1059–1068. ISSN: 2238-7854. DOI: 10.1016/J.JMRT.2021.08.079.

[26] J. Dang, C. Wang, H. Wang, Q. An, J. Wei, B. Gao, Z. Liu, and M. Chen. "Deformation behavior and microstructure evolution of 300M ultrahigh strength steel subjected to high strain rate: an analytical approach". In: *Journal of Materials Research and Technology* 25 (July 2023), pp. 812–831. ISSN: 2238-7854. DOI: 10.1016/J.JMRT.2023.05.203.

[27] N. H. Van Dijk, W. G. Bouwman, S. E. Offerman, et al. "High temperature SANS experiments on Nb(C,N) and MnS precipitates in HSLA steel". In: *Metallurgical and Materials Transactions A* 33 (2002), pp. 1883–1891. DOI: 10.1007/s11661-002-0021-9.

[28] B. B. Wang, D. X. Zhu, C. L. Zhang, X. Y. Zhou, H. H. Wu, S. Z. Wang, G. L. Wu, J. H. Gao, H. T. Zhao, and X. P. Mao. "Influence of typical elements and heat treatment parameters on hardenability in steel: a review". In: *Journal of Iron and Steel Research International* 32.6 (Aug. 2024), pp. 1455–1467. DOI: 10.1007/S42243-024-01307-1.

[29] Thermo-Calc Software AB. *Thermo-Calc Software*. Version 2025b. URL: https://thermocalc.com/products/thermo-calc/ (visited on 10/16/2025).

[30] M. Al-Moussawi, A. J. Smith, A. Young, et al. "Modelling of friction stir welding of DH36 steel". In: *International Journal of Advanced Manufacturing Technology* 92 (2017), pp. 341–360. DOI: 10.1007/s00170-017-0147-y.

[31] S. M. C. van Bohemen. "Bainite and martensite start temperature calculated with exponential carbon dependence". In: *Materials Science and Technology* 28.4 (Apr. 2012), pp. 487–495. ISSN: 0267-0836. DOI: 10.1179/1743284711Y.0000000097.

[32] C. Y. Kung and J. J. Rayment. "An examination of the validity of existing empirical formulae for the calculation of ms temperature". In: *Metallurgical Transactions A* 13.2 (Feb. 1982), pp. 328–331. ISSN: 0360-2133. DOI: 10.1007/BF02643327.

[33] W. Steven and A. G. Haynes. "The Temperature of Formation of Martensite and Bainite in Low-Alloy Steels". In: *Journal of the Iron and Steel Institute* 183.8 (1956), pp. 349–359.

[34] K. Ishida. “Calculation of the effect of alloying elements on the Ms temperature in steels”. In: *Journal of Alloys and Compounds* 220.1-2 (Apr. 1995), pp. 126–131. ISSN: 09258388. DOI: 10.1016/0925-8388(94)06002-9.

[35] K. Andrews. “Empirical formulae for the calculation of some transformation temperatures.” In: *J Iron Steel Inst* 203.7 (1965), pp. 721–727.

[36] S. M. Van Bohemen. “Modeling Start Curves of Bainite Formation”. In: *Metallurgical and Materials Transactions A* 41.2 (Dec. 2009), pp. 285–296. ISSN: 1543-1940. DOI: 10.1007/S11661-009-0106-9.

[37] J. Trzaska. “Calculation of critical temperatures by empirical formulae”. In: *Archives of Metallurgy and Materials* 61.2B (2016), pp. 981–986. ISSN: 17333490. DOI: 10.1515/amm-2016-0167.

[38] M. A. Mohd Fauzi, S. N. Saud, E. Hamzah, M. F. Mamat, and L. J. Ming. “In Vitro Microstructure, Mechanical Properties and Corrosion Behaviour of Low, Medium and High Carbon Steel Under Different Heat Treatments”. In: *Journal of Bio- and Tribo-Corrosion* 5.2 (June 2019), p. 37. ISSN: 2198-4220. DOI: 10.1007/s40735-019-0230-z.

[39] D. Kaiser, D. Torres-Velasquez, S. Dietrich, and V. Schulze. “Design, fabrication and validation of an improved coil for induction dilatometry”. In: *Thermochimica Acta* 689 (July 2020), p. 178612. ISSN: 0040-6031. DOI: 10.1016/J.TCA.2020.178612.

[40] G. Grimvall. “Estimations and Correlations”. In: *Thermophysical Properties of Materials* (1999), pp. 331–352. DOI: 10.1016/B978-044482794-4/50020-6.

[41] H. Torres, M. Varga, and M. R. Ripoll. “High temperature hardness of steels and iron-based alloys”. In: *Materials Science and Engineering: A* 671 (Aug. 2016), pp. 170–181. ISSN: 0921-5093. DOI: 10.1016/J.MSEA.2016.06.058.

[42] ASTM International. *ASTM E112-13: Standard Test Methods for Determining Average Grain Size*. Tech. rep. West Conshohocken, PA: ASTM International, 2013.

[43] J. Schindelin, I. Arganda-Carreras, E. Frise, V. Kaynig, M. Longair, T. Pietzsch, S. Preibisch, C. Rueden, S. Saalfeld, B. Schmid, J.-Y. Tinevez, D. J. White, V. Hartenstein, K. Eliceiri, P. Tomancak, and A. Cardona. “Fiji: an open-source platform for biological-image analysis”. In: *Nature Methods* 9.7 (2012), pp. 676–682. DOI: 10.1038/nmeth.2019.

[44] S. Zaefferer, N.-N. Elhami, and P. Konijnenberg. “Electron backscatter diffraction (EBSD) techniques for studying phase transformations in steels”. In: *Phase Transformations in Steels* (Jan. 2012), pp. 557–587. DOI: 10.1533/9780857096111.4.557.

[45] N. Haghdadi, P. Cizek, P. D. Hodgson, V. Tari, G. S. Rohrer, and H. Beladi. “Effect of ferrite-to-austenite phase transformation path on the interface crystallographic character distributions in a duplex stainless steel”. In: *Acta Materialia* 145 (Feb. 2018), pp. 196–209. ISSN: 13596454. DOI: 10.1016/j.actamat.2017.11.057.

[46] EDAX, Inc. *OIM Analysis Software*. Version 8. 2025. URL: https://www.edax.com/products/ebsd/oim-analysis (visited on 11/09/2025).

[47] S. M. Tan. *Convert EBSD CTF Files to ANG Format: Pure Python Implementation*. 2025. URL: https://github.com/stevenmitchelltan/ctf2ang (visited on 10/29/2025).

[48] EDAX, Inc. *Grain analysis in OIM Analysis*. n.d. URL: https://www.edax.com/news-events/edax-blog/edax-blog-posts/grain-analysis-in-oim-analysis (visited on 02/16/2026).

[49] R. Kawulok, I. Schindler, and P. Kawulok. “Transformation kinetics of selected steel grades after plastic deformation”. In: *Metalurgija* 55.3 (2016), pp. 357–360. DOI: 10.13140/RG.2.1.1401.0001.

[50] I. E. Benrabah, A. Deboer, G. Geandier, H. Van Landeghem, C. Hutchinson, Y. Brechet, and H. Zurob. “Effect of deformation on the bainitic transformation”. In: *Acta Materialia* 277 (Sept. 2024), p. 120195. ISSN: 1359-6454. DOI: 10.1016/J.ACTAMAT.2024.120195.

[51] J. Park, M. Jung, and Y. K. Lee. “Abnormal expansion during the ferro- to para-magnetic transition in pure iron”. In: *Journal of Magnetism and Magnetic Materials* 377 (Mar. 2015), pp. 193–196. ISSN: 0304-8853. DOI: 10.1016/J.JMMM.2014.10.092.

[52] M. M. Aranda, B. Kim, R. Rementeria, C. Capdevila, and C. G. De Andrés. “Effect of prior austenite grain size on pearlite transformation in A hypoeuctectoid Fe-C-Mn steel”. In: *Metallurgical and Materials Transactions A: Physical Metallurgy and Materials Science* 45.4 (2014), pp. 1778–1786. ISSN: 10735623. DOI: 10.1007/s11661-013-1996-0.

[53] L. Zhao, N. Park, Y. Tian, A. Shibata, and N. Tsuji. "Deformation-assisted diffusion for the enhanced kinetics of dynamic phase transformation". In: *Materials Research Letters* 6.11 (Nov. 2018), pp. 641–647. ISSN: 21663831. DOI: 10.1080/21663831.2018.1527787.

[54] H. Bhadeshia and R. Honeycombe. "Acicular Ferrite". In: *Steels: Microstructure and Properties*. 4th. Butterworth-Heinemann, 2017. Chap. 7, pp. 203–216. DOI: 10.1016/b978-0-08-100270-4.00007-x.

[55] D. Loder, S. K. Michelic, and C. Bernhard. "Acicular Ferrite Formation and Its Influencing Factors-A Review". In: *Journal of Materials Science Research* 6.1 (Dec. 2016), p. 24. ISSN: 1927-0585. DOI: 10.5539/jmsr.v6n1p24.

[56] M. I. Equbal, P. Alam, R. Ohdar, K. A. Anand, and M. S. Alam. "Effect of Cooling Rate on the Microstructure and Mechanical Properties of Medium Carbon Steel". In: *International Journal of Metallurgical Engineering* 5.2 (2016), pp. 21–24. ISSN: 2167-7018. DOI: 10.5923/J.IJMEE.20160502.01.

[57] H. Bhadeshia and R. Honeycombe. "Bainite". In: *Steels: Microstructure and Properties*. Butterworth-Heinemann, 2017. Chap. 6, pp. 179–202. DOI: 10.1016/B978-0-08-100270-4.00006-8.

[58] F. García Caballero, C. Capdevila, J. Chao, J. Cornide, C. García Mateo, H. Roelofs, S. Hasler, and G. Mastrogiacomo. "The microstructure of continuously cooled tough bainitic steel". In: *Associazione italiana di metallurgia* (2010).

[59] M. Umemoto, Z. Hai Guo, and I. Tamura. "Effect of cooling rate on grain size of ferrite in a carbon steel". In: *Materials Science and Technology* 3.4 (Feb. 2012), pp. 249–255. ISSN: 02670836. DOI: 10.1179/026708387790122701.

[60] Y. Jiang, J. Xie, Y. Xu, P. Qiao, Y. Lu, and J. Gong. "Evolution of mechanical properties of ferrite and pearlite phases during spheroidization process and their relationship to the overall properties of low alloy steel". In: *Journal of Materials Research and Technology* 29 (Mar. 2024), pp. 5437–5446. ISSN: 2238-7854. DOI: 10.1016/J.JMRT.2024.02.210.

[61] M. Zamani, H. M. Ghasemi, and H. Mirzadeh. "Effect of Variation of Martensite with a Constant Carbon Content on Mechanical Behavior and Sliding Wear of Dual Phase Steels". In: *Tribology Letters* 70.3 (Sept. 2022). ISSN: 15732711. DOI: 10.1007/s11249-022-01616-0.

[62] R. A. Petković, M. J. Luton, and J. J. Jonas. "Recovery and recrystallization of carbon steel between intervals of hot working". In: *Canadian Metallurgical Quarterly* 14.2 (Jan. 1975), pp. 137–145. ISSN: 18791395. DOI: 10.1179/000844375795050201;WGROUP:STRING:PUBLICATION.

[63] E. G. Dere, H. Sharma, R. H. Petrov, J. Sietsma, and S. E. Offerman. "Effect of niobium and grain boundary density on the fire resistance of Fe-C-Mn steel". In: *Scripta Materialia* 68.8 (Apr. 2013), pp. 651–654. ISSN: 13596462. DOI: 10.1016/j.scriptamat.2012.12.030.

[64] H. Landheer, S. E. Offerman, R. H. Petrov, and L. A. Kestens. "The role of crystal misorientations during solid-state nucleation of ferrite in austenite". In: *Acta Materialia* 57.5 (Mar. 2009), pp. 1486–1496. ISSN: 13596454. DOI: 10.1016/j.actamat.2008.11.034.

[65] A. Shibata, G. Miyamoto, S. Morito, A. Nakamura, T. Moronaga, H. Kitano, I. Gutierrez-Urrutia, T. Hara, and K. Tsuzaki. "Substructure and crystallography of lath martensite in as-quenched interstitial-free steel and low-carbon steel". In: *Acta Materialia* 246 (Mar. 2023), p. 118675. ISSN: 1359-6454. DOI: 10.1016/J.ACTAMAT.2023.118675.

[66] H. Kamali, H. Xie, H. Bi, E. Chang, H. Xu, H. Yu, and Z. Jiang. "Deformation mechanism and texture evolution of a low-Ni Cr–Mn–N austenitic stainless steel under bending deformation". In: *Materials Science and Engineering: A* 804 (Feb. 2021). ISSN: 09215093. DOI: 10.1016/j.msea.2020.140724.

A

Equations

A.1. Phase Transformation

$$\text{Transformation on heating} = \frac{(\Delta L - y_1)}{(y_2 - y_1)} \times 100 \tag{A.1}$$

$$\text{Transformation on cooling} = \frac{(y_2 - \Delta L)}{(y_2 - y_1)} \times 100 \tag{A.2}$$

$$\Delta L = L - L_0, \tag{A.3}$$

where ΔL is the change in length of the sample, L is the length of the specimen at temperature T, L_0 is the measured initial length (at room temperature). y_1 and y_2 are reference values of ΔL at the beginning and end of the transformation, respectively.

A.2. M_S Temperature

Note, x_i is in wt%.

Ishida [34]

$$M_S = 545 - 330x_C - 23x_{Mn} - 7x_{Si} - 14x_{Cr} - 13x_{Ni} - 13x_{Cu} - 5x_{Mo} + 2x_{Al} + 7x_{Co} - 4x_{Nb} + 3x_{Ti} + 4x_V \tag{A.4}$$

van Bohemen [31]

$$M_s = 565 - 600 \cdot (1 - e^{-0.96x_C}) - 31x_{Mn} - 13x_{Si} - 18x_{Ni} - 10x_{Cr} - 12x_{Mo} \tag{A.5}$$

Steven & Haynes [33]

$$M_s = 561 - 474x_C - 33x_{Mn} - 17x_{Cr} - 21x_{Mo} - 17x_{Ni} \tag{A.6}$$

Andrews [35]

$$Ms = 561 - 423x_C - 30.4x_{Mn} - 12.1x_{Cr} - 7.5x_{Mo} - 17.7x_{Ni} + (10x_{Co} - 7.5x_{Si}) \tag{A.7}$$

Kung & Rayment (mod. St&H)* [32]

$$Ms = 561 - 474x_C - 33x_{Mn} - 17x_{Cr} - 21x_{Mo} - 17x_{Ni} + 10x_{Co} - 7.5x_{Si} \tag{A.8}$$

*This is an adaptation of the equation of Andrews [35], and Steven & Haynes [33] by also considering also the effects of Co and Si [32].

A.3. B_S Temperature

Note, x_i is in wt%. These equations calculate the B_S temperatures for TTT curves.

van Bohemen [31]

$$B_S = 839 - (86x_{Mn} + 23x_{Si} + 67x_{Cr} + 33x_{Ni} + 75x_{Mo}) - 270 \cdot [1 - exp(-1.33 \cdot x_C)] \tag{A.9}$$

Steven & Haynes [33]

$$B_S = 835 - 198x_C - 91x_{Mn} - 15x_{Si} - 73x_{Cr} - 36x_{Ni} - 87x_{Mo} \tag{A.10}$$

A.4. Austenite temperatures

Note, x_i is in wt%.

A_{c1} [37]
On heating, the temperature at which austenite begins to form.

$$A_{c1}\,[^\circ C] = 742 - 29\,x_{\mathrm{C}} - 14\,x_{\mathrm{Mn}} + 13\,x_{\mathrm{Si}} + 16\,x_{\mathrm{Cr}} - 17\,x_{\mathrm{Ni}} - 16\,x_{\mathrm{Mo}} \tag{A.11}$$

A_{c3} [37]
On heating, the temperature at which austenite finished forming.

$$A_{c3}\,[^\circ C] = 925 - 219\sqrt{x_{\mathrm{C}}} - 7\,x_{\mathrm{Mn}} + 39\,x_{\mathrm{Si}} - 16\,x_{\mathrm{Ni}} + 13\,x_{\mathrm{Mo}} + 97\,x_{\mathrm{V}} \tag{A.12}$$

B

Dilatometer Results

B.1. Graphs

The first derivative of the ΔL curve (dL/dT) highlights the rate of dimensional change with temperature, allowing clearer identification of transformations. The transformation start and end temperatures were determined from the points where the slope of the dilatation curve deviated from and returned to the linear baseline, respectively, marking the onset and completion of the phase transformation. For consistency in analysis and visualization, the ΔL axis was fixed to a range of 100 μm for all plots, while the dL/dT axis was fixed to a range of -3 to 1 $\mu m/^{\circ}C$ for all plots.

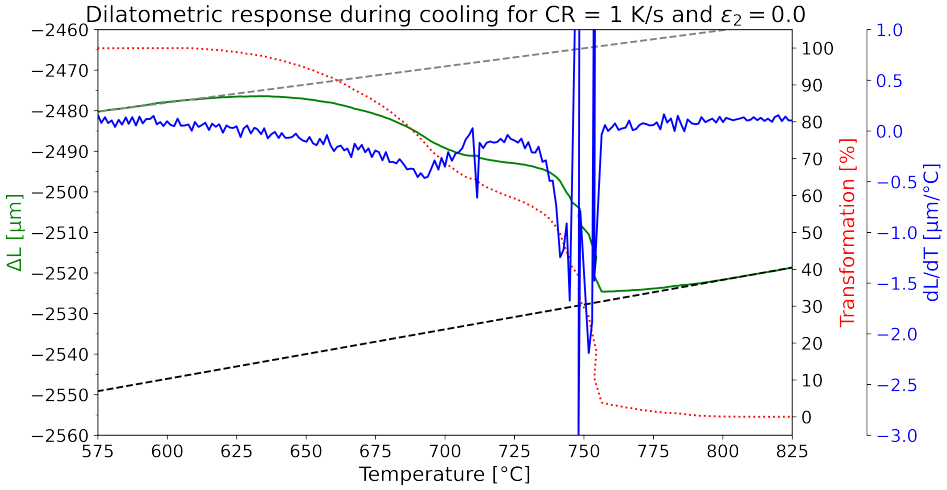

(a) $\varepsilon_2 = 0.0$

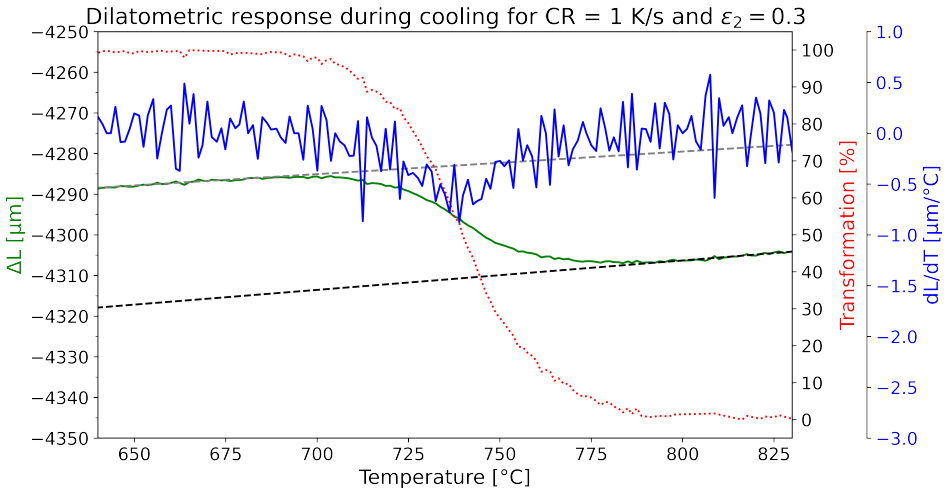

(b) $\varepsilon_2 = 0.3$

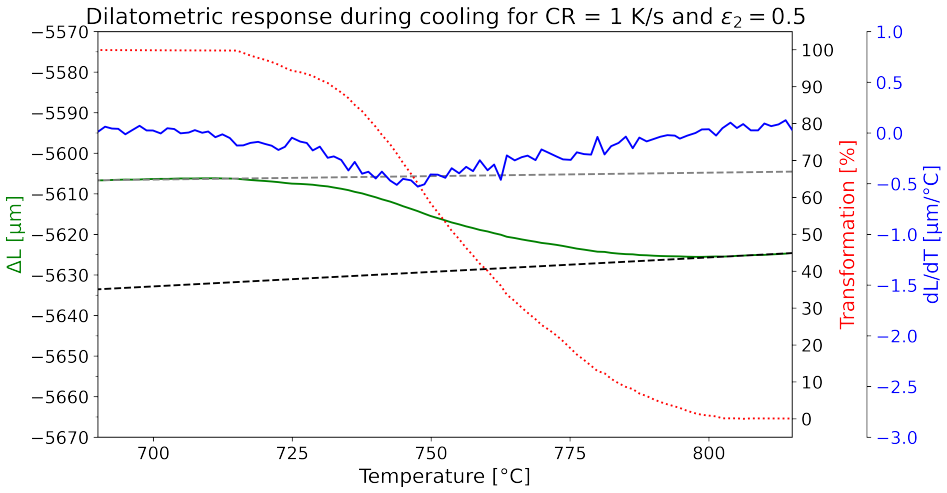

(c) $\varepsilon_2 = 0.5$

Figure B.1: Dilatometer cooling curves at 1 K/s for different values of ε_2.

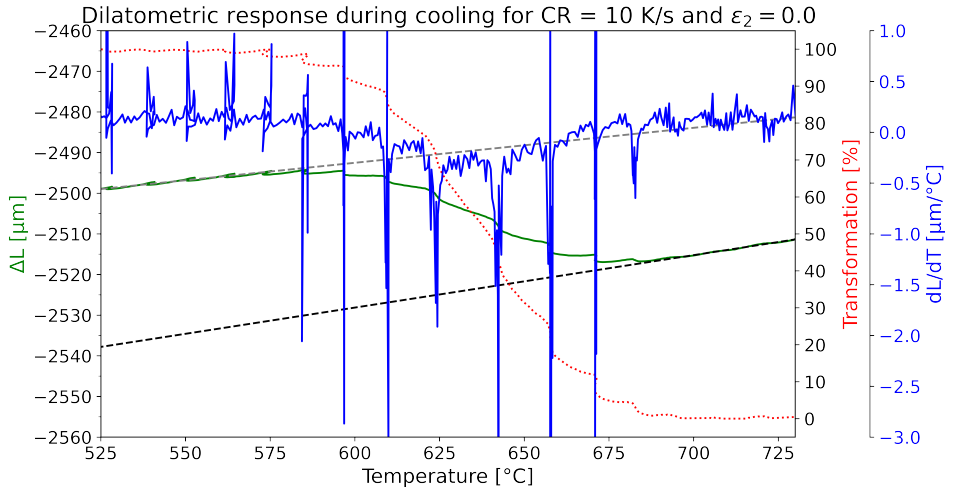

(a) $\varepsilon_2 = 0.0$

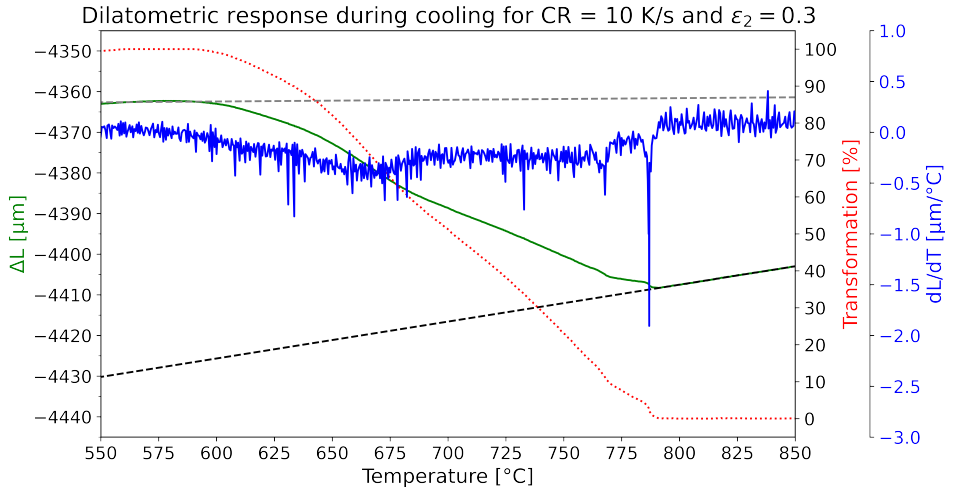

(b) $\varepsilon_2 = 0.3$

Figure B.2: Dilatometer cooling curves at 10 K/s for different values of ε_2. The noisy dL/dT signal in (b) originates from HF power fluctuations not phase transformations (the HF graphs are shown later).

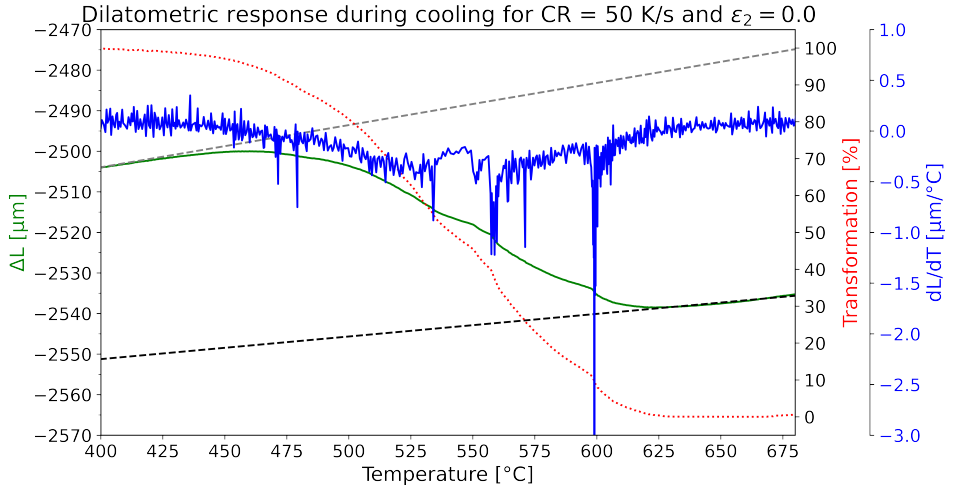

(a) $\varepsilon_2 = 0.0$

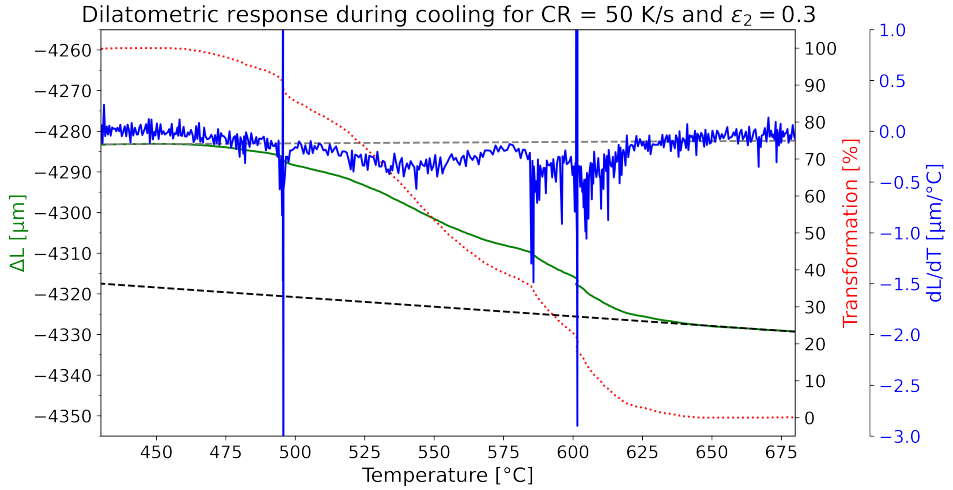

(b) $\varepsilon_2 = 0.3$

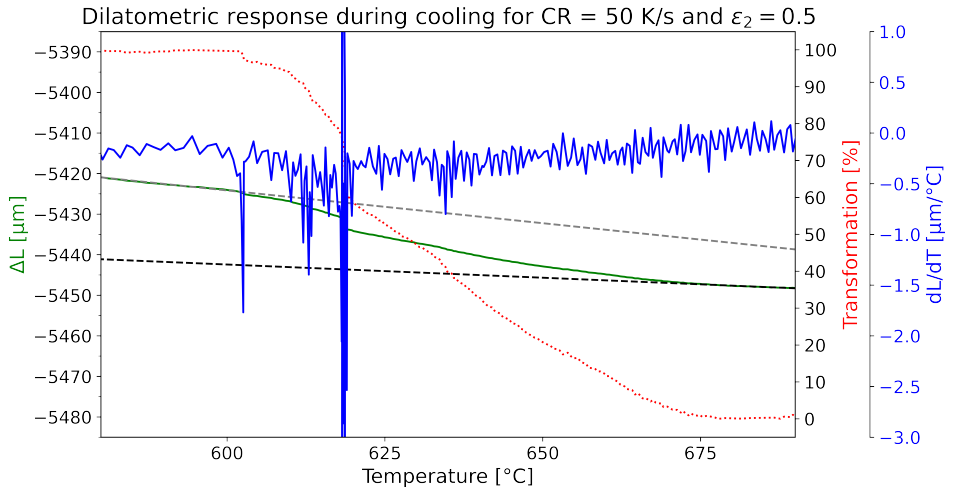

(c) $\varepsilon_2 = 0.5$

Figure B.3: Dilatometer cooling curves at 50 K/s for different values of ε_2.

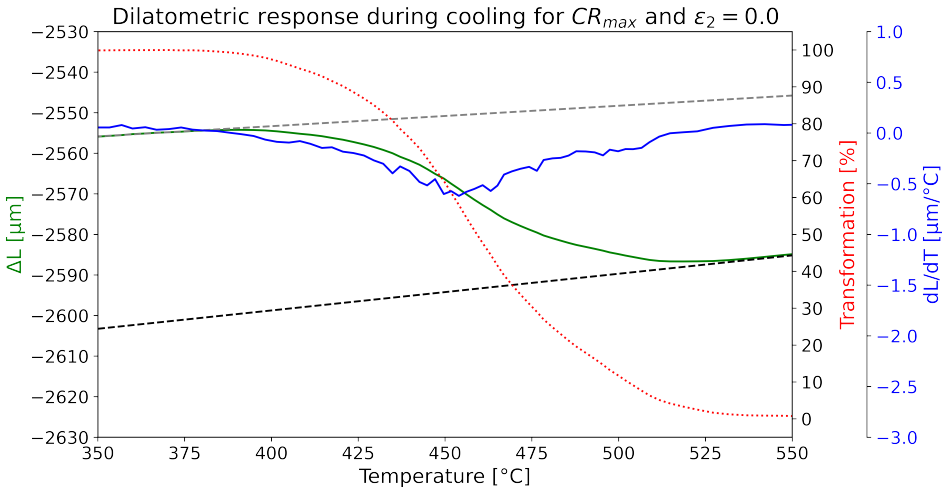

(a) $\varepsilon_2 = 0.0$

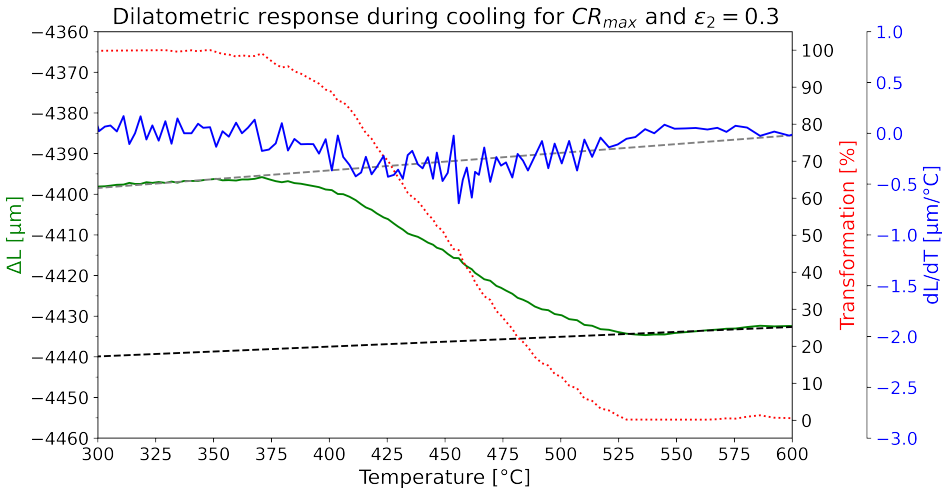

(b) $\varepsilon_2 = 0.3$

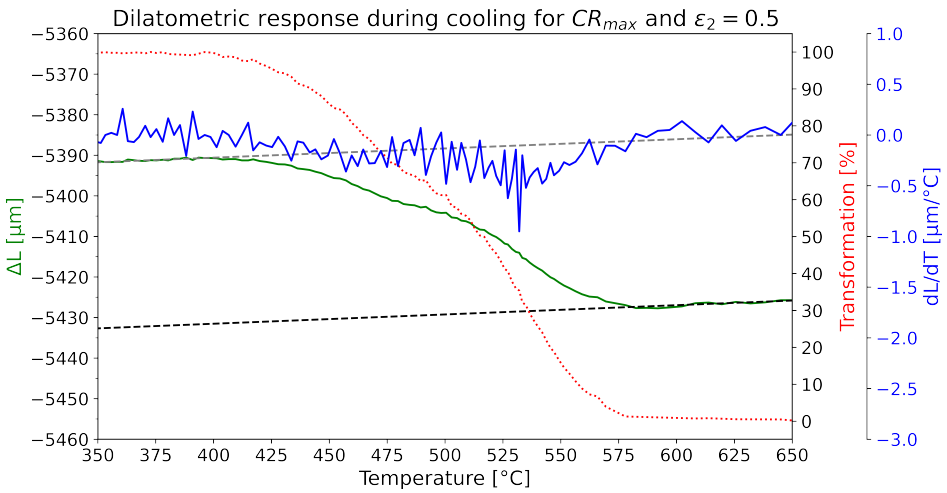

(c) $\varepsilon_2 = 0.5$

Figure B.4: Dilatometer cooling curves under quenching conditions for different values of ε_2.

B.2. HF Power

There were some samples that had great variation in the HF power curve, and this was reflected in the *dL/dT*, making them appear very noisy. This was misleading when determining phase transformation temperatures. This section includes the dilatometer plots including the HF power curve of those samples where this was case.

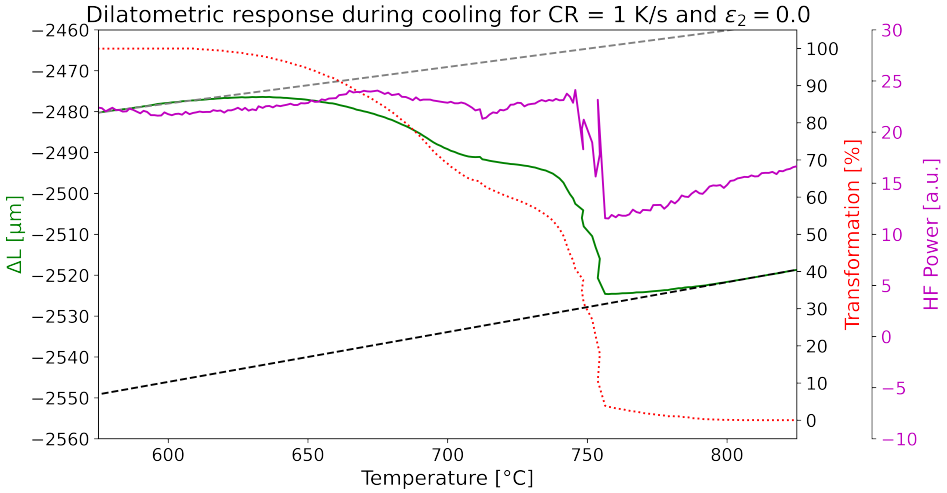

Figure B.5: Dilatometer cooling curve showing the HF Power curve for CR = 1 K/s, $\varepsilon_2 = 0.0$.

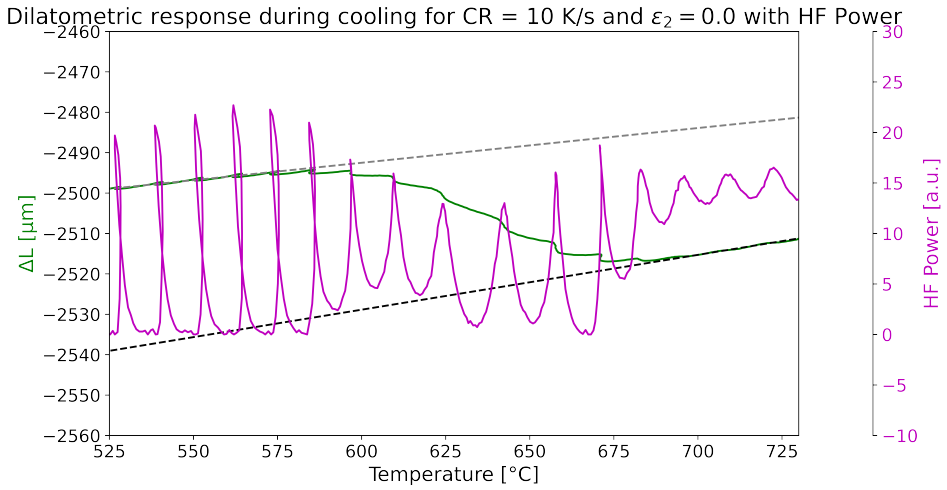

Figure B.6: Dilatometer cooling curve showing the HF Power curve for CR = 10 K/s, $\varepsilon_2 = 0.0$.

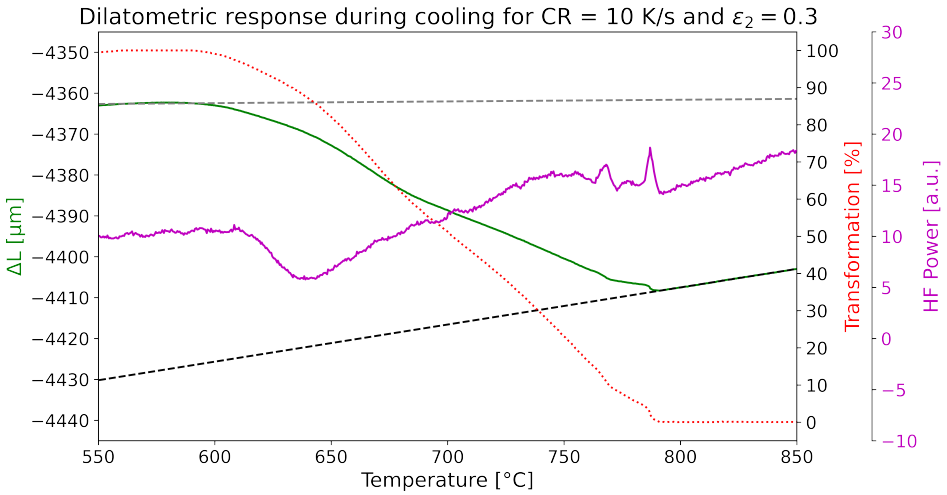

Figure B.7: Dilatometer cooling curve showing the HF Power curve for CR = 10 K/s, $\varepsilon_2 = 0.3$.

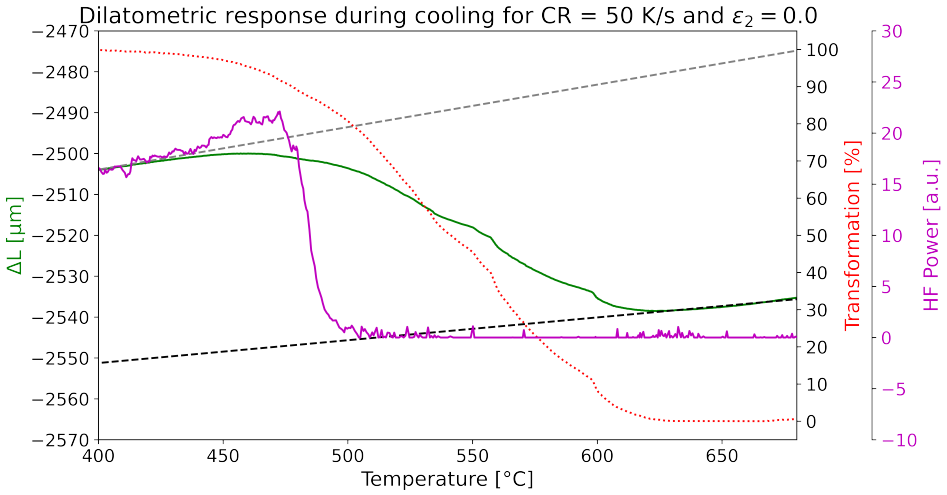

Figure B.8: Dilatometer cooling curve showing the HF Power curve for CR = 50 K/s, $\varepsilon_2 = 0.0$.

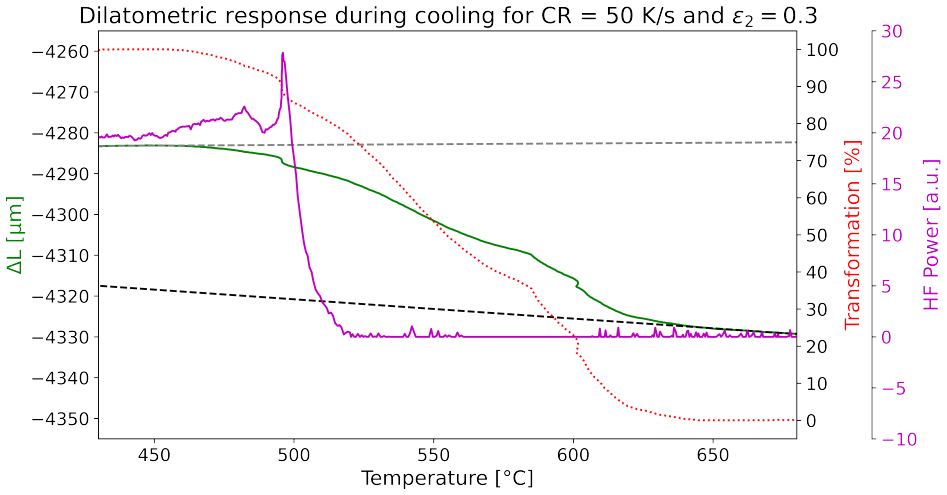

Figure B.9: Dilatometer cooling curve showing the HF Power curve for CR = 50 K/s, $\varepsilon_2 = 0.3$.

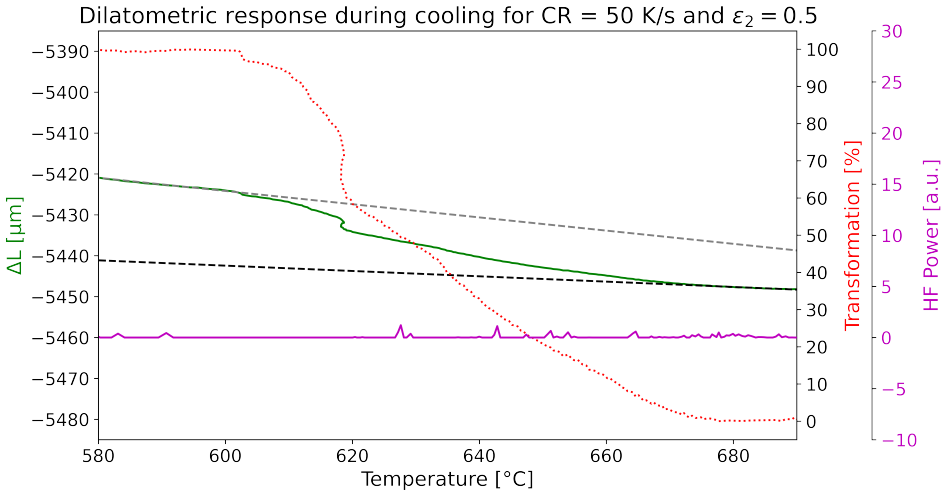

Figure B.10: Dilatometer cooling curve showing the HF Power curve for CR = 50 K/s, ε_2 = 0.5.

B.3. Duplicates Example

This example shows two samples tested with the same TMP in the dilatometer, yielding similar results and indicating good reproducibility of the method.

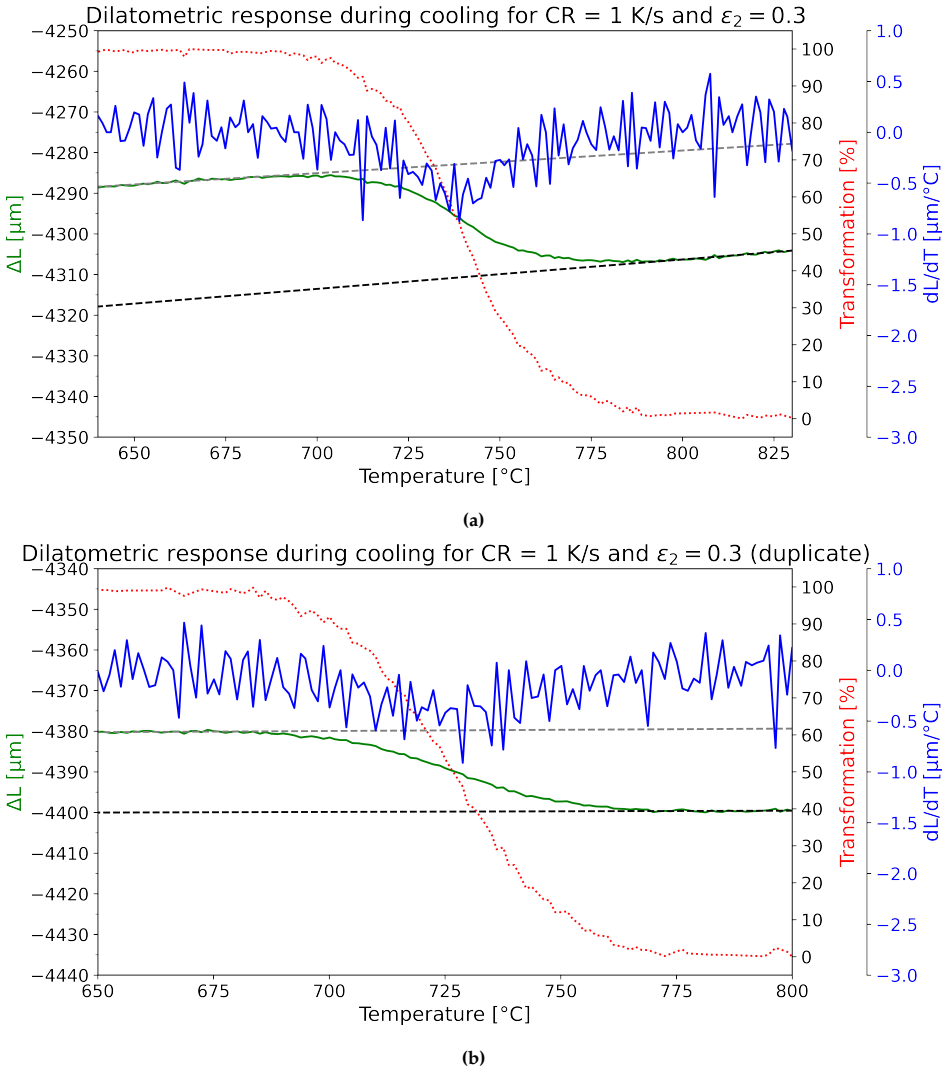

Figure B.11: Dilatometer plots of two duplicates that were cooled down at 1 K/s and compressed with $\varepsilon_2 = 0.3$.

B.4. Phase Fractions

For those samples with two phases, their phase fractions were determined and the results are presented in the table below.

CR [K/s]	ε_2	T_{inf} [°C]	Transformed fraction (f_A) [%]	Fraction of 2nd phase (f_B) [%]
1	0.0	707.9	65.1	34.9
	0.3	716.5	88.3	11.7
	0.5	726.3	90.0	10.0
10	0.0	–	–	–
	0.3	697.1	49.8	50.2
50	0.0	541.2	50.0	50.0
	0.3	549.6	49.9	50.1
	0.5	–	–	–
CR_{max}	0.0	–	–	–
	0.3	451.0	49.1	10.9
	0.5	466.4	76.7	23.3

Table B.1: Inflection temperature (T_{inf}) and the corresponding phase fraction of the 1st phase transformed, with the phase fraction of the 2nd phase (f_B) during cooling as a function of cooling rate and deformation ε_2.

C

Construction of CCT Diagram

To plot the Thermo-Calc CCT on Excel the following the steps were taken:

1. Draw the cooling rate curves for 10, 50 and 100 K/s (the 1 K/s curve is the right-most curve) on the CCT plot.
2. Draw horizontal starting at the intersection between a ferrite or bainite curve with the 1, 10, 50 and 100 K/s CR curves, and ending at the y-axis (T).
3. Now refer back to the data used to plot the cooling rate curves, and find the corresponding time (t) for each T value found for every cooling rate.
4. The M_s temperature is known (453 °C). Add the M_s series at t = 0.1 s and at t = 9.0 s, so that the M_s line ends where it intersects the 50 K/s curve (found from the data used to make the 50 K/s curve).
5. After adding all the transformation series separately, the chart type for each series was changed to 'Scatter with smooth lines'.

The data used for the plots is shown below.

Table C.1: Experimental data used for CCT construction without deformation (ε_2 = 0.0).

Cooling rate	Transformation start							
	Martensite		Bainite		Ferrite		Pearlite	
(K/s)	Time (s)	T (°C)	Time (s)	T (°C)	Time (s)	T (°C)	Time (s)	T (°C)
1	–	–	–	–	89.8	785	192	707.9
10	–	–	–	–	–	–	15	750
50	7.2	541.2	4.9	625	–	–	–	–
CR_{max}	3.8	525.0	–	–	–	–	–	–

For the CCT diagram showing the effect of deformation, the following data was also included in the plot.

Note that no distinction has been made between acicular ferrite or polygonal ferrite, they have instead been combined in the "Ferrite" curve.

Table C.2: Experimental data used for CCT construction at ε_2 = 0.3.

Cooling rate	Transformation start							
	Martensite		Bainite		Ferrite		Pearlite	
(K/s)	Time (s)	T (°C)	Time (s)	T (°C)	Time (s)	T (°C)	Time (s)	T (°C)
1	–	–	–	–	58.8	816	183	716.5
10	–	–	–	–	9.01	785	–	–
50	7.0	549.6	5.4	630	–	–	–	–
CR_{max}	4.5	451.0	1.6	530	–	–	–	–

Table C.3: Experimental data used for CCT construction at ε_2 = 0.5.

Cooling rate	Transformation start							
	Martensite		Bainite		Ferrite		Pearlite	
(K/s)	Time (s)	T (°C)	Time (s)	T (°C)	Time (s)	T (°C)	Time (s)	T (°C)
1	–	–	–	–	73.8	801	174	726.3
10	–	–	–	–	–	–	–	–
50	–	–	5.0	635	4.5	660	–	–
CR_{max}	–	–	2.7	490	1.5	575	–	–